# Photodynamic inactivation of bacteria with ZrTCPP thin films

Martin Tran


Master Thesis
Materials Science for Energy and Nanotechnology
60 credits

Department of Chemistry
Faculty of Mathematics and Natural Sciences

UNIVERSITY OF OSLO

May 2021

2021

Photodynamic inactivation of bacteria with ZrTCPP thin films

Martin Tran

http://www.duo.uio.no/

# Acknowledgements

The work presented in this MSc was performed in the NAFUMA group at the Department of Chemistry, Faculty of Mathematics and Natural Sciences at the University of Oslo, from August 2018 to May 2021 under the supervision of Prof. Ola Nilsen, Melania Rogowska, Per-Anders Hansen, and Håkon Valen.

I would like to express my very great appreciation to my supervisor Ola Nilsen for letting me work on this project. Thank you for always having your doors open, and providing me with much knowledge, encouragement, and good advice.

I would like to thank my co-supervisor Melania Rogowska for guidance and assistance in this project. Thank you for teaching me how to operate instruments in the labs, guidance in data analysis and writing, and so much more. I am particularly grateful that you could perform the antibacterial assay, as I could not do it myself due to the COVID-19 restrictions.

I would also like to thank Per-Anders Hansen, Ole Bjørn Karlsen, David Wragg, and Veljko Petrovic, for your brilliant assistance in the labs and guidance with data analysis. Thank you, Malin Solheim Olsen, your advice has been a great help in this project.

Thank you, my fellow MENA-students, Hanne, Christine, Silje, Ida, Marie, Veronica, and Salah, for making this adventure such a blast. I couldn't have asked for better people to finish this run with. I am especially going to miss our intellectual lunch conversations.

Lastly, I would like to thank my friends and family, especially Maren and Marie for making Oslo feel like a second home.

University of Oslo, May 2021

Martin Tran

# Abstract

In this work, we explored an alternative method for the treatment of bacterial infections to reduce the use of antibiotics. The use of antibiotics has led to the rapid emergence of resistant bacteria spreading worldwide, which has become a major threat as it poses severe consequences for human life. Our approach is to enhance the photodynamic inactivation (PDI) of bacteria by incorporating Zr into the porphyrin 4,4',4'',4'''-(porphine-5,10,15,20-tetrayl)tetrakis(benzoic acid) (TCPP). PDI process is based on the combination of a photosensitizer, light and molecular oxygen, which leads to the formation of reactive oxygen species (ROS) that cause damage to pathogenic bacteria. We explored the fabrication of ZrTCPP films by spin coating technique with the goal to optimize the procedure for formation of uniform films. Our approach is based on alternating the deposition of Zr and TCPP to build layers of film. Furthermore, we studied the optical and chemical properties of the deposited thin films and discussed the reproducibility and saturation of the films based on collected UV-Vis data. Moreover, the ZrTCPP films deposited by spin coating were evaluated for stability in an aqueous solution. We have also investigated a wet chemical layer-by-layer approach of fabricating ZrTCPP films. The method was performed in a flow-cell while collecting the UV-Vis spectra in situ. In this way, we were able to collect data for the chemical reactions of ZrTCPP formation as function of time.

The characterization data manifest that we have reached our goal by fabricating uniform thin films by spin coating. In addition, our results show that the absorption spectrum of the TCPP porphyrin was shifted into the visible range by forming a hybrid material with zirconium. This increased the effective absorption of the material. The films proved to be very photoactive and after only 10 min irradiation (11.4 $Jcm^{-2}$) of blue light, a 100% bacterial reduction was found for planktonic *Enterococcus faecalis* model bacteria. Without irradiation, our films also show a significant bacterial reduction. On overall, we have demonstrated an alternative method of synthesis of porphyrin-based materials, which is reproducible and efficient. The significant bacterial reduction of the planktonic and biofilm of *E. faecalis* bacteria demonstrate that ZrTCPP thin films has the potential to be a powerful agent in PDI.

# List of Abbreviations

| | |
|---|---|
| **ABMM** | Anthracene derivative tetrasodium-2,2'-(anthracene-9,10-diyl)bis(methylmalonate) |
| **AFM** | Atomic force microcopy |
| **ALD** | Atomic layer deposition |
| **BHI** | Brain heart infusion |
| **CFU** | Colony forming units |
| **CLSM** | Confocal laser scanning microscope |
| **Cu-Cy** | Copper-cysteamine |
| **CUR** | Curcumin |
| **DBD** | Dielectric barrier discharge |
| **DCFH-DA** | 2'-7'dichlorofluorescin diacetate |
| **DI** | Distilled |
| **DMF** | Dimethylformanide |
| **DMSO** | Dimethylsulfoxide |
| **DV** | Droplet volume |
| **EDS** | Energy-dispersive spectroscopy |
| **EPS** | Extracellular polymeric substances |
| **FEG** | Field emission gun |
| **FTIR** | Fourier-transform infrared spectroscopy |
| **GFP** | Green fluorescent protein |
| **GFU** | Green fluorescent protein |
| **GS** | Ground state |
| **HOMO** | Highest occupied molecular orbital |
| **ICG** | Indocyanine green |
| **IR** | Infrared |
| **ISC** | Intersystem crossing |
| **IUPAC** | International Union of Pure and Applied Chemistry |
| **LALD** | Liquid atomic layer deposition |
| **LUMO** | Lowest unoccupied molecular orbital |

| | |
|---|---|
| **MB** | Methylene blue |
| **MNP** | Magnetic nanoparticles |
| **MOF** | Metal-organic framework |
| **NAFUMA** | Nanostructures and Functional Material |
| **NaOCl** | Sodium hypochlorite |
| **NIOM** | Nordic Institute of Dental Materials |
| **NP** | Nanoparticle |
| **OD** | Optical density |
| **ON** | Overnight |
| **PBS** | Phosphate-Buffered Saline |
| **PDI** | Photodynamic inactivation |
| **PDT** | Photodynamic therapy |
| **PI** | Propidium iodide |
| **PLA** | 3-phenyllactic acid |
| **PMT** | Photomultiplier tube |
| **PS** | Photosensitizers |
| **PTTP-Glu-Ac** | Poly-5,15-diphenyl(2,5′-dithienylene)-10,20-di(3,5-di-O-TEG-tetra-O-acetyl-D-galactopyranoside-phenyl)porphyrin |
| **RBG** | Rose bengal group |
| **RMS** | Root-mean-square |
| **ROS** | Reactive oxygen species |
| **rpm** | Revolutions per minute |
| **RSS** | Rotational spin speed |
| **RT** | Room temperature |
| **SE** | Spectroscopic ellipsometry |
| **SEM** | Scanning electron microscopy |
| **TCPP** | 4,4’,4’’,4’’’-(porphine-5,10,15,20-tetryl)tetrakis(benzoic acid) |
| **TG** | Triaminoguanidinium chloride |
| **THPP** | 5,10,15,20-tetrakis(4-hydroxy-phenyl)-21H,23H-porphine |
| **TSB** | Tryptone soya broth |

| | |
|---|---|
| **UV-Vis** | Ultraviolet-visible |
| **WFC** | Woven cotton fabrics |
| **XPS** | X-ray Photoelectron Spectroscopy |
| **XRD** | X-ray diffraction powder diffraction |

# Contents

**ACKNOWLEDGEMENTS** ..... **IV**

**ABSTRACT** ..... **VI**

**LIST OF ABBREVIATIONS** ..... **VIII**

**1 INTRODUCTION** ..... **1**

1.1 MOTIVATION ..... 1

1.2 DEFINITION OF THE THESIS ..... 2

1.3 HISTORY AND BACKGROUND ..... 3

*1.3.1 Antibiotic Resistance: The eternal race between human and bacteria* ..... *3*

*1.3.2 Antimicrobial surfaces* ..... *5*

*1.3.3 History of light therapy* ..... *8*

1.4 PORPHYRINS AS PHOTOSENSITIZERS ..... 9

*1.4.1 Photosensitizers* ..... *9*

*1.4.2 Introduction to porphyrins* ..... *10*

*1.4.3 Naming porphyrins* ..... *14*

*1.4.4 Porphyrins as photosensitizers* ..... *14*

*1.4.5 Porphyrin used in this thesis* ..... *15*

1.5 PREVIOUS WORK ..... 15

*1.5.1 Fabrication of porphyrin-based material* ..... *16*

*1.5.2 Antibacterial porphyrin-based materials in the literature* ..... *21*

*1.5.3 Antibacterial activity against bacteria E. faecalis in literature* ..... *27*

**2 THEORY** ..... **31**

2.1 PORPHYRIN-BASED MATERIAL FOR INACTIVATION OF BACTERIA ..... 31

*2.1.1 Basic photochemistry* ..... *31*

*2.1.2 Energy diagram* ..... *32*

*2.1.3 Photosensitizing mechanisms* ..... *34*

2.2 INTRODUCTION TO BACTERIA ..... 35

*2.2.1 Bacteria cell wall* ..... *36*

*2.2.2 Biofilm* ..... *37*

*2.2.3 Bacterial growth* ..... *38*

*2.2.4 Bacteria in this thesis* ..... *40*

**3 METHODS ..... 41**
3.1 THIN FILMS ..... 41
*3.1.1 Uniformity ..... 41*
*3.1.2 Plasma cleaner ..... 41*
*3.1.3 Spin coating ..... 42*
*3.1.4 Atomic layer deposition (ALD) ..... 43*
*3.1.5 Liquid atomic layer deposition (LALD) ..... 44*
3.2 CHARACTERIZATION TECHNIQUES ..... 45
3.3 ANTIBACTERIAL ASSAY METHODS ..... 45
*3.3.1 Performing an antibacterial assessment ..... 45*
*3.3.2 Confocal laser scanning microscope (CLSM) ..... 47*
**4 EXPERIMENTAL ..... 48**
4.1 REAGENTS AND SOLVENTS ..... 48
*4.1.1 Preparation of precursors ..... 49*
4.2 SUBSTRATES ..... 49
*4.2.1 Substrate pre-treatment ..... 50*
*4.2.2 Plasma cleaner: ..... 50*
*4.2.3 Sample handling ..... 50*
4.3 SPIN COATING ..... 50
4.4 ALD ..... 51
4.5 LAYER-BY-LAYER LIQUID DEPOSITION ..... 51
*4.5.1 Fabrication of flow-cell ..... 52*
4.6 CHARACTERIZATION TECHNIQUES ..... 53
*4.6.1 UV-Vis spectroscopy ..... 53*
*4.6.2 UV-Vis used in LbL deposition ..... 54*
*4.6.3 Ellipsometry ..... 54*
*4.6.4 Contact angle ..... 54*
*4.6.5 FTIR ..... 54*
*4.6.6 AFM ..... 54*
*4.6.7 XRD ..... 55*
*4.6.8 SEM and EDS ..... 55*
4.7 MATERIALS AND METHODS ..... 55
*4.7.1 Bacteria ..... 55*
*4.7.2 Materials ..... 56*

*4.7.3 Light source* ..... *57*
*4.7.4 Antibacterial phototoxicity on planktonic bacteria* ..... *58*
*4.7.5 Adhesion of bacteria* ..... *58*
*4.7.6 Phototoxicity of ZrTCPP films* ..... *59*
*4.7.7 Antibacterial phototoxicity on biofilm* ..... *60*
*4.7.8 Control of biofilm formation* ..... *60*
*4.7.9 LIVE/DEAD BacLight protocol* ..... *60*
*4.7.10 Phototoxicity of ZrTCPP films* ..... *61*

**5 RESULTS** ..... **62**

5.1 ZRTCPP THIN FILMS ..... 62

*5.1.1 Deposition by spin-coating* ..... *62*
*5.1.2 Optical properties* ..... *66*
*5.1.3 FTIR* ..... *67*
*5.1.4 Reproducibility* ..... *69*
*5.1.5 Saturation* ..... *70*
*5.1.6 Absorbance of solutions with different concentration* ..... *73*
*5.1.7 Washing step* ..... *75*
*5.1.8 Layer-by-layer liquid deposition* ..... *76*
*5.1.9 Stability in aqueous solution* ..... *82*
*5.1.10 Recovery of lost Zr in the water* ..... *85*
*5.1.11 Stability at various pH-levels* ..... *86*
*5.1.12 Elemental mapping by EDS* ..... *89*
*5.1.13 Saline solution* ..... *89*
*5.1.14 Contact angle* ..... *90*
*5.1.15 XRD* ..... *91*
*5.1.16 AFM* ..... *92*
*5.1.17 Ellipsometry* ..... *93*
*5.1.18 Summary of result* ..... *93*

5.2 ANTIBACTERIAL PROPERTIES ..... 94

*5.2.1 Phototoxicity of ZrTCPP films against planktonic bacteria* ..... *95*
*5.2.2 Phototoxicity in supernatant* ..... *97*
*5.2.3 Antibacterial effect against established biofilm* ..... *99*
*5.2.4 Summary of results* ..... *100*

**6 DISCUSSION ..... 101**
6.1 ZrTCPP THIN FILM ..... 101
*6.1.1 Water stability ..... 105*
*6.1.2 Layer-by-layer liquid deposition ..... 108*
6.2 ANTIBACTERIAL PROPERTIES ..... 109
*6.2.1 Planktonic E. faecalis ..... 109*
*6.2.2 Dark toxicity ..... 113*
*6.2.3 Biofilm ..... 113*
**7 CONCLUSION ..... 115**
**8 FURTHER PERSPECTIVES ..... 116**
**9 REFERENCES ..... 118**
**APPENDIX A ..... 128**
A.1 UV-VIS SPECTROSCOPY ..... 128
A.2 X-RAY DIFFRACTION (XRD) ..... 129
A.3 FOURIER-TRANSFORM INFRARED SPECTROSCOPY (FTIR) ..... 131
A.4 SCANNING ELECTRON MICROSCOPY (SEM) ..... 132
A.5 ENERGY DISPERSIVE X-RAY SPECTROSCOPY (EDS) ..... 134
A.6 ATOMIC FORCE MICROSCOPY (AFM) ..... 134
A.7 SPECTROSCOPIC ELLIPSOMETRY ..... 136
A.8 CONTACT ANGLE ..... 137
**APPENDIX B ..... 139**
B.1 CALCULATIONS ..... 139
B.2 EDS ..... 140

# 1 Introduction

## 1.1 Motivation

Even though humans have climbed to the top of the food chain, the fight for survival is not over yet. Pathogenic bacteria are one of the microbes that are very harmful to us. In fact, our fight against these pathogens has now grown challenging because our primary mitigation, antibiotics, has been weakened due to an increase in antibiotic resistance. Already now, we see an increase in medical costs, prolonged hospital stays, and mortality. This is a major threat to human health, and the world urgently needs alternative ways to fight these pathogens [1]. Many alternative methods to reduce the use of antibiotics are in development and have shown significant results. One such method is the fabrication of new surfaces that eliminate or substantially reduce the extent of bacterial attachment and biofilm formation on the surfaces. Antibacterial surfaces may repel or resist the initial attachment of microbes by exhibiting an anti-fouling effect or bactericidal effect. Anti-fouling surfaces may resist or prevent cellular attachment because of an unfavorable surface topography or surface chemistry for the microorganisms [2, 3]. While the bactericidal effects induce cell death by inactivation of microbes in contact with the surface. One encouraging class of material showing bactericidal effect is porphyrins. The development of porphyrin-based materials is a growing field, especially, towards antibacterial properties. Life as we know it, would be impossible without porphyrins and their relatives. For example, the well-known iron-containing porphyrin, also known as heme, is used to bind oxygen in the bloodstream. Porphyrin-based materials are known to absorb energy from visible light and transfer it to nearby oxygen. This chemical process generates reactive oxygen species (ROS) that can reduce microbes [4] (p. 177-180).

This thesis builds on the master thesis by Malin Solheim Olsen on porphyrin-based surfaces for photodynamic inactivation of bacteria, performed at the NAFUMA group. In the beginning, their goal was to fabricate the films by atomic layer deposition (ALD), to create films with good coverage and adhesion by control of layer-by-layer construction. However, her work proved that to bring the porphyrin into the gas-phase was too challenging as the porphyrin decomposed at around sublimation. Therefore, they further explored an alternative method of fabrication of films, which is by liquid phase depositions. A spin coating technique was used to produce the thin films of ZrTCPP. The antibacterial properties of these films were evaluated against

*Enterococcus faecalis* bacteria at the Nordic Institute of Dental Materials (NIOM). The thin films were irradiated with blue light for 20 minutes and inhibit a 99.95% reduction of viable bacteria in the established biofilm. These great results inspired further exploration in this direction of the project. However, creating a homogenous thin films that are stable in water by spin-coating was a challenge and needed to be further explored for optimization. The experience gained through the master thesis by Olsen has become the motivation and foundation for this project. This project is also related to the Ph.D. project of Melania Rogowska.

## 1.2 Definition of the thesis

Our goal with this MSc project is to fabricate antibacterial thin films and evaluate their antibacterial properties. The chosen material is a photo catalytically active hybrid material based on a material formed between $Zr^{4+}$ as the inorganic part and the porphyrin TCPP (Figure 1.1) as the organic compound. Furthermore, we will investigate the antibacterial effect by ROS production of the thin film. To reach this goal, this thesis is divided into two parts.

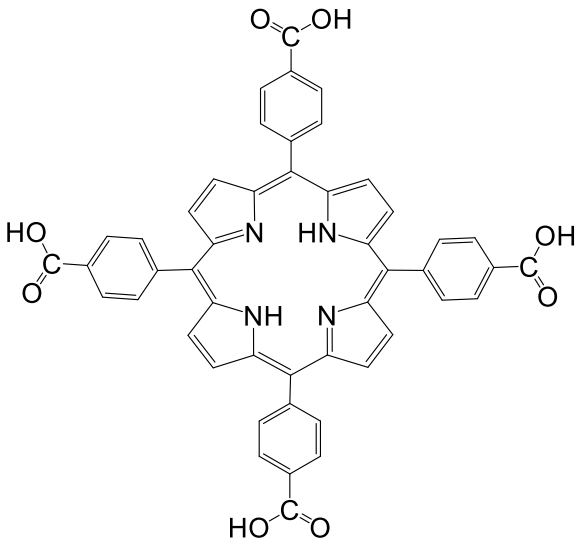


Figure 1.1: Chemical structure of TCPP.

The first part aims to fabricate and characterize the hybrid material as deposited. We will continue to fabricate the ZrTCPP films by spin coating and optimize this process with respect to uniform and reproducible films. Furthermore, we will explore fabrication by a layer-by-layer approach in a specially designed chamber that allows for in-situ optical measurements during growth. The goals are to create a reproducible homogenous thin film that is stable in an aqueous

solution and change the UV-Vis absorption to increase the visible light absorption. These are important factors for the second part of the project. The stability of the thin film will be evaluated in different solutions. To gain more insight into the thin film properties, different techniques were conducted, such as UV-Vis spectroscopy, spectroscopic ellipsometry (SE), X-ray powder diffraction (XRD), scanning electron microscopy (SEM) in combination with energy-dispersive spectroscopy (EDS), atomic force microscopy (AFM), Fourier-transform infrared spectroscopy (FTIR), and contact angle measurements.

The second part of this project is to evaluate the antimicrobial properties of the thin film. The bacteria used in this project are *E. faecalis*, which are the same bacteria used in Olsen's master thesis. The application and characterization of ZrTCPP thin film for its antimicrobial properties were done at the Nordic Institute of Dental Material (NIOM). NIOM's vision for this project is to provide an antibacterial coating for use in dental health. The viability of bacteria *E. faecalis* planktonic and biofilm culture were evaluated after exposure to ZrTCPP in combination with visible light and without light.

## 1.3 History and background

### 1.3.1 Antibiotic Resistance: The eternal race between human and bacteria

In the pre-antibiotic era, just a simple infection disease could lead to a high morbidity and mortality. Antibiotics were regarded as the most important therapeutic agents that have been globally used to aid human health against mild and treatable illnesses to deadly bacterial infections. Moreover, antibiotics did not only have high efficacy in treatments, but were also widely available and relatively low in cost [5]. However, the highly popular and demanded use of antibiotics had a downside. In 2014, The World Health Organization announced that antibiotic resistance is one of the three greatest threats to human health. Antibiotic resistance is increasing, which poses a severe challenge in public health [6]. The predicted outcome of the increasing resistance will result in approximately 10 million deaths by 2050 [7]. The causes and spread of antibiotic resistance are complex and include many aspects of human behavior. The consequences affect every individual on this planet.

The coronavirus disease in 2019 (COVID-19) rapidly spread globally and became the start of a pandemic in March 2020. The outbreak of this deadly virus has caused enormous pressure on medical workers, high death rates and struggling economy [8]. However, in early 2021 the vaccines are in development and are widely distributed. The pandemic will end one day, but the aftermath may be significant. The increased hospital admission and disruption to health service could increase the risk of health-care-associated infections and the transmission of the multidrug-resistant organism [9, 10]. Researchers believe that the COVID-19 is accelerating the threat of antibiotic resistance. Reports have shown that 72% of COVID-19 patients that are admitted to hospitals have received antimicrobial agents. However, only 8% of the patients were diagnosed with co-infected bacteria or fungi and needed antibiotic treatment. The high abuse of antibiotics was due to high pressure on health services, lack of competence, and weak antibiotic control [11]. A combination of the increased exposure to healthcare settings and antibiotic use has been one of the reasons for the amplified opportunity for pathogens to become resistant and spread [12]. In addition, the exposure to biocidal agents due to environmental and personal disinfections can pose another threat, as it also enhances antibiotic resistance [13].

Over the past decade, the development of new medical agents has lagged behind the increasing antibiotic resistance. Bacteria develop the ability to withstand drugs faster than we can compete. In a community of bacteria, there may be bacteria cells that are resistant to certain antibiotics. Bacteria that are sensitive to the antibiotic will die, which leaves more nutrients for the resistant bacteria to grow and multiply in a population (Figure 1.2). Bacteria have high metabolic and physiological adaptability, which means we keep needing new sources to control them [14]. The ideal solution is to keep them under control while not aid the growth condition for the mutated and resistant bacteria. As the cells multiply, small errors will occur in the genome sequence, known as mutations. Mutations are one of the main reasons that bacteria have such high physiological adaptability. Therefore, bacteria can become resistant to any antibiotic over time. In addition, when a bacteria has the mutated genome sequence against an antibiotic, it can sustain the rest of the bacteria community by gene transfer. The easiest way for bacteria to become resistant to a drug is to inhibit the adhesion of drugs to their cell wall. Bacteria can achieve this by mutations that alter the proteins of the cell walls accordingly [15]. Modern medicine is struggling to keep up with the rate at which bacteria are becoming resistant. New strategies for fighting infections are needed to prevent returning to the pre-antibiotic era.

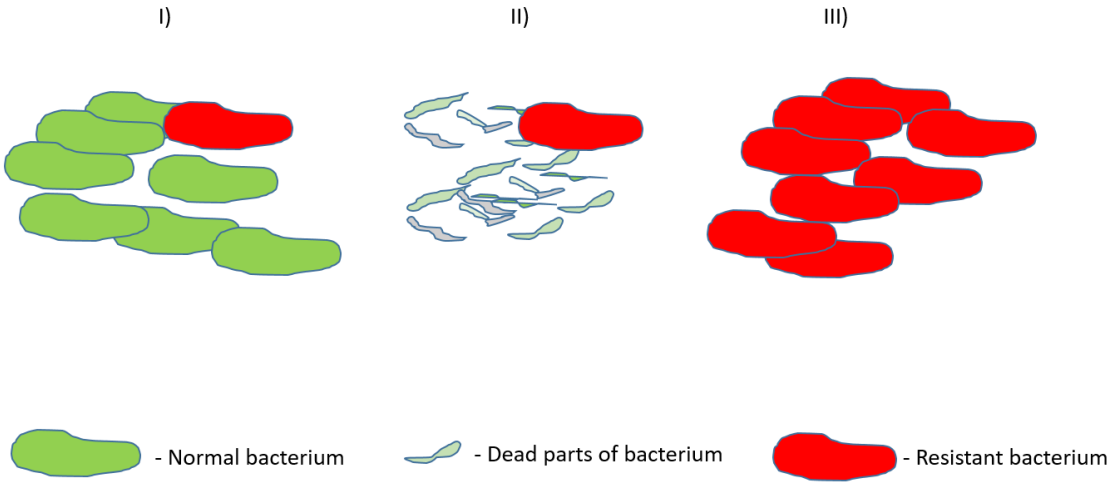


Figure 1.2: Illustration of the reason for antibiotic resistance. I) A culture of normal bacteria where a few are resistant to antibiotic. II) Antibiotics kills the normal bacteria while the resistant bacteria survives. III) The drug resistant bacteria have now better conditions for growth.

### 1.3.2 Antimicrobial surfaces

Not all bacteria are harmful. A large number of our bacteria help with breaking down food and protect us from other harmful bacteria. These bacteria are called symbiotic. We refer to the bacteria that do us harm as pathogens. These pathogens are the common enemy for all human life. Bacteria can be found in most places on the planet Earth. Therefore, it is common that surfaces are colonized by bacteria. Consider the large number of surfaces you are in contact with on a daily basis such as phone, computer, door handles, etc. The adhesion of bacteria on surfaces can be unfavorable for the environment, industry, and even human health. Bacteria can be responsible for the infection of medical implants, or tissues causing infection to humans. Furthermore, adhesion of bacteria can lead to biological layer built-up, which leads to blockage and reduction of aero- or hydrodynamic properties. Bacteria can also lead to bio-corrosion by the formation of “pits” on metallic surfaces through corrosion (e.g. copper water pipes) [16]. With the ideal environment and resources, bacteria can form a biofilm that is extremely difficult to eradicate. Therefore, it is desirable to prevent the growth of bacteria on surfaces. This can be achieved by utilizing antibacterial coatings on surfaces. The term “antibacterial surface” refers to surfaces that prohibit or reduce the growth and proliferation of microorganisms [17]. This can be achieved through anti-fouling or bactericidal effects. There is a range of approaches for

the design of such surfaces. Figure 1.3 is an illustration of several designs of antibacterial surfaces that inhibits bacterial growth.

Antifouling surfaces can repel proteins, bacteria, or biological species from attacking the surface [18] (p. 31). The development of these surfaces to inhibit adhesion can be via steric repulsion, low surface energy, or electrostatic repulsion as seen in Figure 1.3. Strategies for fabrication of such surfaces can be by modifying the surface to be hydrophilic, exhibit low surface free energy, and/or become negatively charged [19]. Extensive development has been made in the fabrication of these surfaces [20-22]. Inspiration to create these surfaces can be found in nature. For example, the lotus leaf, which exhibits antifouling properties. The self-cleaning ability of this plant is due to the superhydrophobic surface. This inspires the exploration of modifying the micro-and nanostructure on surfaces to mimic creations that are found in nature [23, 24]. As mentioned earlier, the other method of inhibiting bacterial growth on surfaces is to kill them in contact with the surface, known as bactericidal effect.

Antimicrobial agents have been exploited by humans for a long time. This discipline has been practiced by ancient Egyptians, Greeks, and Aztecs, where they used copper-containing compounds and alloys for sterilizing wounds and drinking water [25]. The common approach for developing antimicrobial surfaces is to functionalize the surface so it can quickly kill bacteria that come into contact with the surface. Strategies for the development of these surfaces can be via drug-releasing or contact-killing surfaces. For example, surfaces coated with silver nanoparticles have proven to be highly effective at damaging bacteria and leads to cell death [26, 27]. However, leaching and releasing of antibacterial agents from materials could result in a biosafety challenge. Also, it reduces the longevity of the material. This challenge can be avoided by contact-killing surfaces where the architectural design of the surface porosity, roughness, and geometry, exhibit resistance to microbial colonization by breaking down the bacteria at contact [28]. For example, the surface of *Psaltoda claripennis* cicada wings is found to be bactericidal. The robust hexagonal arrays of "nanopillars" on the surface kill bacteria with extreme efficacy by piercing the bacteria in contact. This discovery was the first example of a surface that exhibits bactericidal properties from purely physical actions [29].

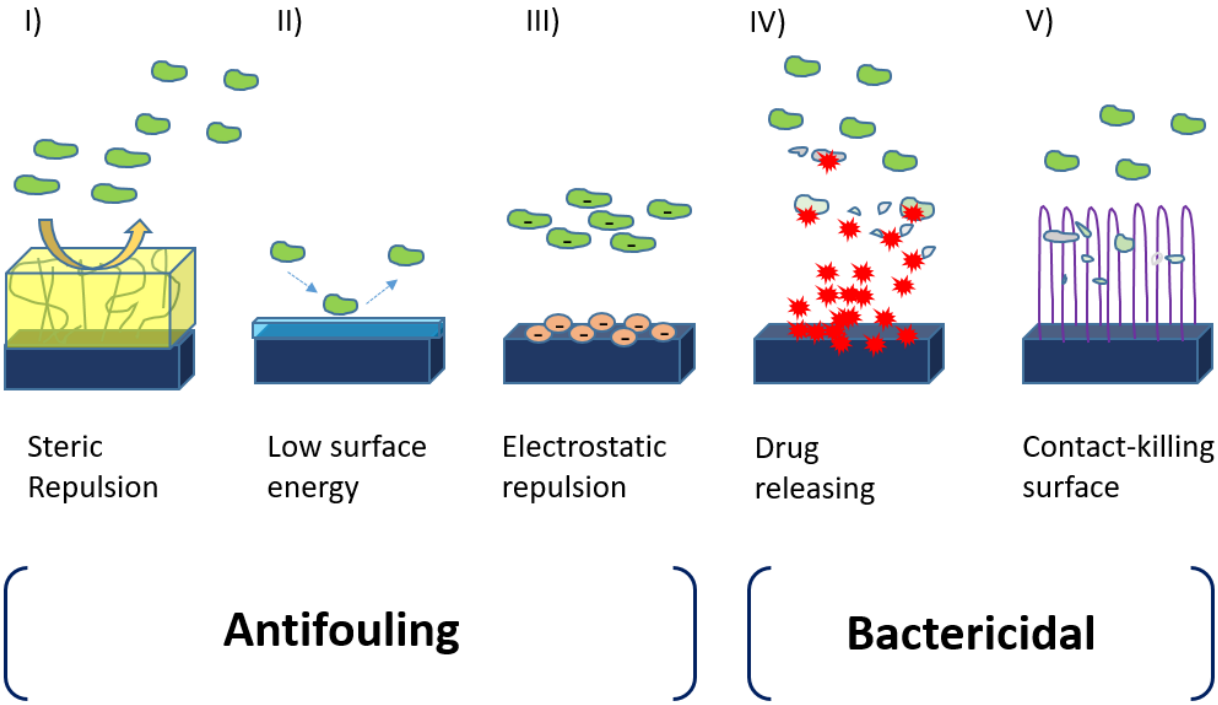


Figure 1.3: Illustration of several antifouling and antimicrobial surfaces. I) Polymers attached to the surface provide physical barriers that inhibit adhesion of microbes. II) Microbes are not able to attach to the surface due to the low surface energy. III) The charged surface repels microbes with the same electric charge. IV) The release of antimicrobial agents inhibit adhesion of microbes by killing them. V) The structure of the coating kill microbes upon contact.

As we have seen, there are many ways of functionalizing a surface to exhibit antibacterial effects. However, finding the ideal method is challenging and many factors must be considered, such as biosafety and biocompatibility. Usually, we want the material to be highly stable and show high efficacy at killing bacteria. Furthermore, the method for killing bacteria is chosen according to the type of bacteria we are facing. We first distinguish between gram-positive and gram-negative bacteria, and then determine the form the bacteria have taken, whether it is a suspension or a biofilm. Classifying the type of bacteria is a crucial step in fighting it. Usually, antibiotics only work for either gram-positive or gram-negative but not both. The gram-positive and gram-negative bacteria can be distinguished by their cell wall [14]. More information about the cell wall will be provided in a later section (section 2.2.1). The golden area of antibiotics resulted in reduced interest in photodynamic antimicrobial chemotherapy. However, the wind is shifting, as mentioned earlier antibiotics are becoming less secure against pathogens. Initially, photodynamic therapy (PDT) was developed to be used in cancer treatment. A combination of suitable light and photosensitizers (PS) can generate reactive oxygen species (ROS), which have the property to induce cell damage and eventually lead to cell death. Nevertheless, recent

studies have shown that PDT has a promising potential in reducing bacteria culture, henceforward referred to as photodynamic inactivation (PDI) (Figure 1.4) [30]. The generation of ROS by light energy provides advantages such as activation/deactivation of bactericidal effect and localized treatment [31, 32]. This approach is believed to be a promising method to kill pathogens with a low risk of bacterial resistance. The advantage of the photo destructive effect of ROS is the possibility to attack multiple cellular targets fast and efficiently, which lowers the probability of bacteria reacting [33]. Another advantage of PDI is that it can be used for killing biofilm-grown cells both in vitro and in vivo where antibiotics fail [34].

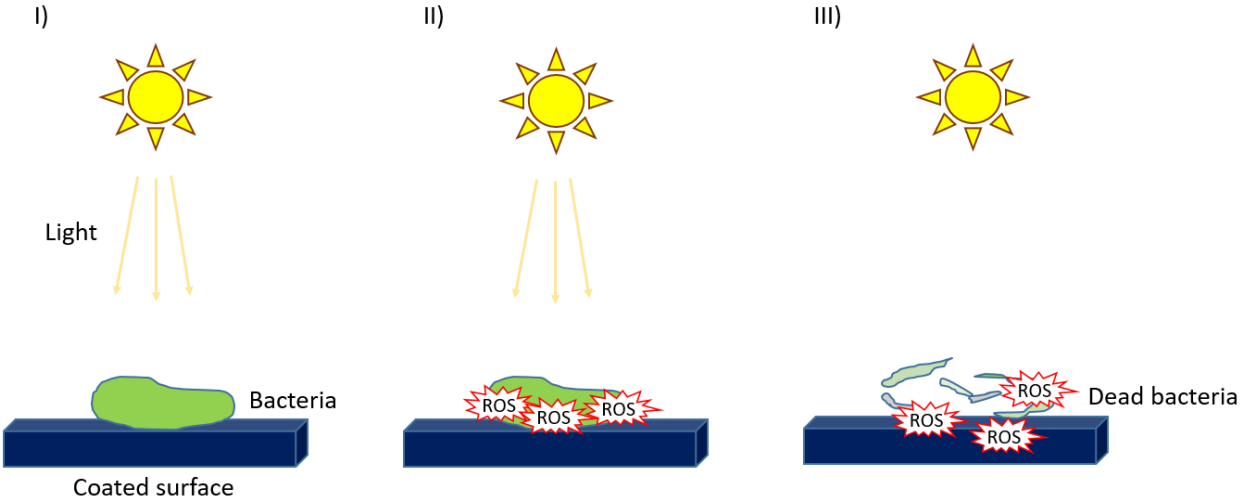


Figure 1.4: Illustration of photodynamic inactivation of bacteria. (I) The coated surface is infected by bacteria. (II) The surface is illuminated with light and creates ROS. (III) ROS damages the bacteria, which leads to cell death.

### 1.3.3 History of light therapy

Using light in medical therapy has lately received increased attention. The origin of this method can be traced back to ancient Greece, Egypt and India. Phototherapy was later introduced to Western medicine at the beginning of the 20th century by Oscar Raab and his supervisor Hermann von Tappeiner. Their experiments show that acridine (Figure 1.5) with the addition of light yields toxicity. Herman von Tappeiner's work brought this light therapy into science. He described the oxygen-dependent photosensitization, which became the foundation for "photodynamic therapy". This method was further popularized by the physician Niels Finsen who won the Nobel prize in 1903 for his work of carbon arc phototherapy against skin tumors.

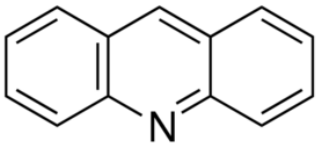


Figure 1.5: Chemical structure of acridine.

In 1841, hematoporphyrin was made for the first time by H. Scherer and was investigated by W. Hausmann and H. Pfeiffer. In 1911, they reported that this porphyrin shows a toxicity effect against mice and guinea pigs during exposure to intense light. Three years later, the toxicity of porphyrin as photosensitizing agents in humans was put on the map by Friedrich Meyer-Betz. He injected himself with hematoporphyrin to prove the toxicity against the human body [35]. Their work inspired that porphyrins could be further exploited as photosensitizers in medical therapy with light irradiation.

## 1.4 Porphyrins as photosensitizers

Porphyrin is a substance with a wide diversity of biochemical functions. As porphyrins were brought into the medical world, their usage as photosensitizers has awoken a great interest among researchers. Particularly, the interaction of porphyrin-based material with electromagnetic waves in the region from 200 to 1000 nm [36]. In this section, photosensitizers and porphyrin will be introduced. Moreover, porphyrin as photosensitizers will be discussed. Finally, a brief introduction of the porphyrin used in this thesis will be presented.

### 1.4.1 Photosensitizers

ROS, such as oxygen radicals, hydrogen peroxide, or singlet oxygen, are utilized as weapons to initiate damage to bacteria. This method of killing bacteria is also known as photodynamic therapy. ROS can be chemically produced with the aid of a photosensitizer. A photosensitizer is a molecule that harvests the energy from light and converts this energy by bringing oxygen molecules into a highly unstable state [36].

Organic molecules have proven to be good photosensitizers as they are able to absorb energy in the visible light range. Usually, radiation with a high-energy photons are needed for the electronic excitation of organic molecules. The fundamental energy absorption in organic

compounds lies within the C=C double bonding. The absorption of energy excites the bonding/non-bonding π-electron into an anti-bonding π* orbital [37].

Transition: $\pi \rightarrow \pi^*$

π bonds are formed by the sideways overlap of the half-filled p orbitals when two carbon atoms form a double bond. The atomic structure of photosensitizers usually gives rise to a large delocalized π-system. This system is a part of the whole π-framework rather than localized between two specific nuclei (Figure 1.6). Thus, the electrons are shared between several nuclei. As a result, the energy level of HOMOs (highest occupied molecular orbitals) is lowered. In other words, the delocalized π-systems decrease the band gap between HOMO and LUMO (lowest unoccupied molecular orbitals), resulting in the absorption of energy with a longer wavelength, ultimately in the visible light region.

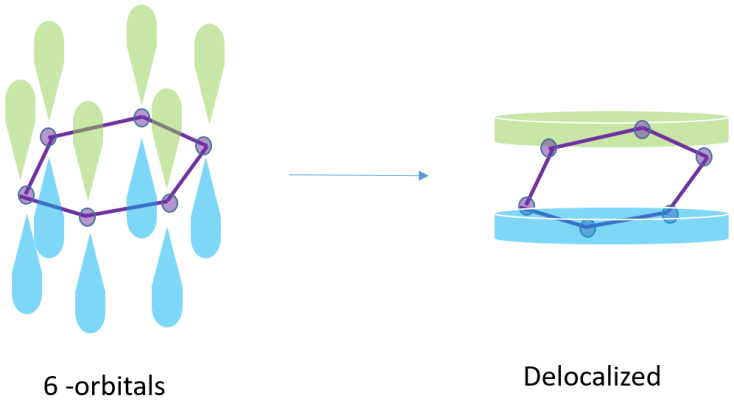


Figure 1.6: Illustration of a conjugated π-system. Electron density delocalized over all six carbon atoms.

### 1.4.2 Introduction to porphyrins

The porphyrins have been called “pigments of life” due to their importance in the biological world. A full range of biological processes that are either performed or catalyzed by porphyrin-containing proteins is the origin of life as we know it. The name “porphyrin“ is traced back to the Greek word “porphyra” which means purple. It was early recognized that the intensity and color of porphyrins are derived from the highly conjugated π-electron systems. Porphyrins are also well known for hemes, giving blood cells the red color and chlorophyll that gives plants its green color [4, 38] (p. 3). Attempt to replicate the same properties of naturally occurring

porphyrins, gives an origin for syntheses of contracted, isomeric, and expanded porphyrins [39]. The basic building block for all porphyrins starts with the simplest chemical structure as seen in Figure 1.7.

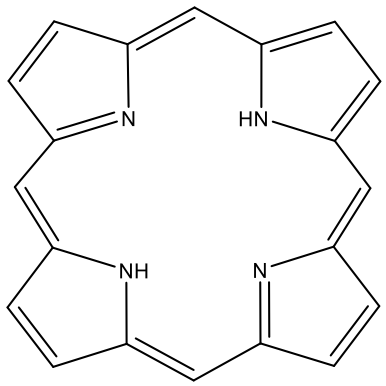


Figure 1.7: Chemical structure of the simplest porphyrin.

Porphyrins are planar aromatic macrocycles. The basic unit of porphyrins is pyrrole, which consists of an aromatic five-membered nitrogen heterocycle and belongs to the group of azoles. Pyrroles have π-excessive due to their six π-electrons that are distributed over five atoms. The excessive π-electrons make them good π-donors. Porphyrin is formed by linking together four pyrrole units by their α-position via methane bridges (also denoted as meso carbon atoms). Porphyrins are planar structures, and the atomic arrangement gives it an extended π-system where only 18 out of 26 π-electrons contribute to the delocalized conjugated π-system. Consequently, the gap between HOMO and LUMO decreases and can absorb energy with wavelengths within the visible region [40, 41].

Perhaps the most fascinating aspect of porphyrins are their characteristic UV-Visible absorption spectra. These spectra are characterized by the Soret band and the Q-bands in the visible light region (Figure 1.8). The Soret band has strong absorption at around 400 nanometers, whereas the Q-bands show absorption in the 480-700 nm range. The total number and intensity of these bands can provide powerful information about the molecular arrangement of the porphyrin and whether it is metalleted (coordinated to a metal) or not. The spectra of the porphyrins were interpreted by the four-orbital model. This model was proposed by Martin Gouterman in the 1960s [42, 43]. Four energy levels are needed to explain the absorption spectra of porphyrins. The transitions of these four energy levels occur through two HOMOs and two LUMOs. These energy levels can be altered by the addition of a metal ion in the center and the substituents on the ring that influence the absorption spectra of the porphyrin. Higher splitting of the two energy

states gives rise to the Soret band, which has a high energy state with high oscillator strength. Whereas, a lower energy state with low oscillator strength gives rise to Q-bands [44].

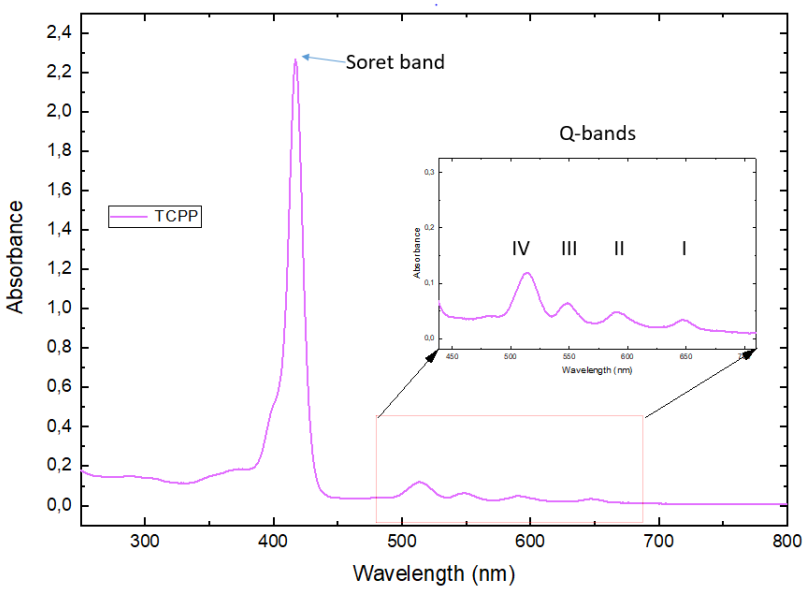


Figure 1.8: An illustration of a typical absorption spectrum of a free-base porphyrin. The Soret band and the Q-bands are the characteristics of the porphyrin.

Porphyrins have a great variety of properties. A free-base porphyrin is a porphyrin without a metal center and usually exhibits a red-orange color in solutions. These properties can be tuned by binding with varieties of metal-ions in the center of the porphyrin ring or at the meso-positions of the molecule (Figure 1.9). Porphyrins usually bind with a metal ion having chargers of 2+ or 3+ to form a complex. This addition of metal usually makes the metalloporphyrins very stable. At the same time, the symmetry in the molecule increases, which gives a more simplified absorptions spectrum for visible light [44]. The four Q-bands for a typical free-base porphyrin normally decrease to two Q-bands in a porphyrin metal complex (Figure 1.10). The two Q-bands are denoted as α and β bands by the pictorial classification, where the α band is at a longer wavelength than the β band. The relative intensities of these two bands can be a qualitative indicator of how strong the metal is connected to the center of the porphyrin. If α > β, the metal-porphyrin complex is stable and has a square-planer geometry, e.g. (Ni(II), Pd(II), Sn(IV), Cd(II)). Whereas, when β > α, the metal will easily be substituted by protons [4] (p. 84-96). The symmetry of the porphyrin can also be increased by protonating the porphyrin by an acid. This leads to the addition of two further protons to the central nitrogens. As a consequence, the porphyrin changes in color, and the four Q-bands collapse to two. The color change can also be affected by substitution in the meso- or β-pyrolle positions. The meso substitution changes

the whine red color of the free base to deep emerald green in solution, coinciding with a redshift in the position of the Soret band (sometimes as much as 40 nm, reliant on the meso substituent). Meanwhile, the β-pyrolle substitution yields a magenta color. The redshift of the spectrum can also be observed when the porphyrin is in an aqueous solution and the degree of redshift are in correlation with the particular meso-substituents. Furthermore, the incorporation of diamagnetic metals (i.e. zinc or aluminum) into the phosphor promotes photoactivation. Alternatively, substitution with a paramagnetic metal like iron or manganese inhibits photoactivation [45]. Metal ions of small sizes can form metal porphyrins with in-plane coordination mode. Otherwise, for metal ions with a larger size, formation happens through out-of-plane coordination mode, which decreases the symmetry [41].

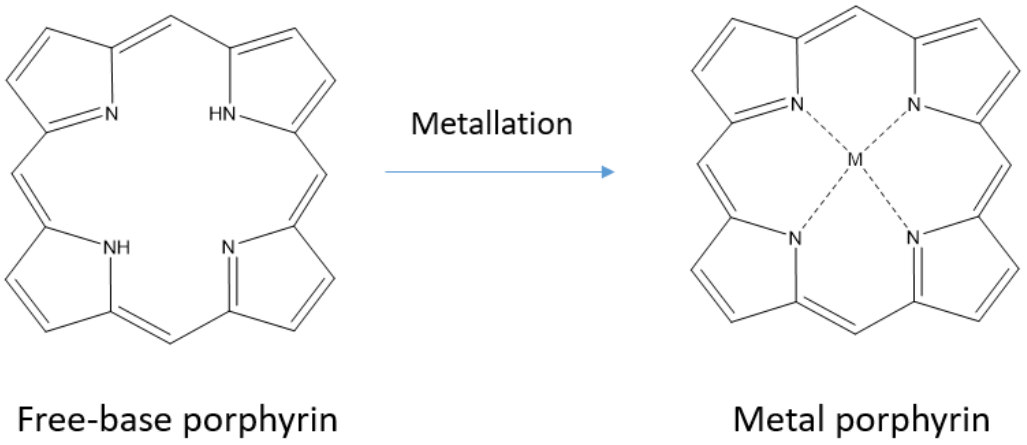


Figure 1.9: Schematic illustration of the incorporation of metal into a free-base porphyrin.

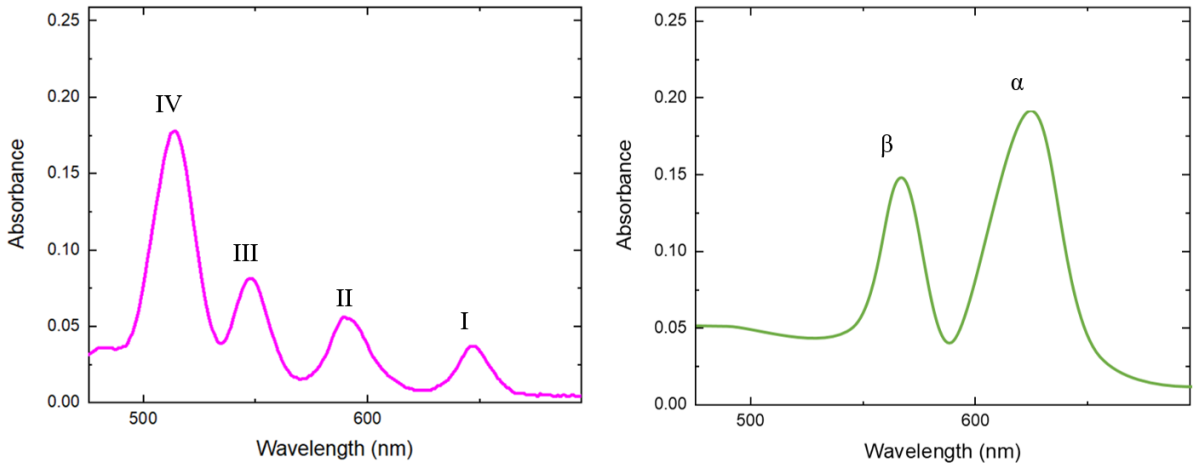


Figure 1.10: Left: Characteristic a free-base porphyrin with four Q-bands. Right: Metallated porphyrin with two Q-bands.

### 1.4.3 Naming porphyrins

Porphyrins were commonly given trivial names. Two different nomenclatures were introduced for better communication, the Fisher´s, and the IUPAC. The Fisher´s nomenclature uses a lower-case Greek alphabet (α, β, ϒ, δ) to describe the substituted meso-positions (Figure 1.11), while accordingly, the IUPAC uses numbers (5, 10, 15, 20). The Greek alphabet or the number at the beginning of their names indicates that they are meso-substituted. Using Fisher´s or the IUPAC nomenclature system is up to the author. The IUPAC system also has a numbering scheme for every carbon and nitrogen atom in the pyrrole ring, which is favorable for complex systems [4] (p. 6-12).

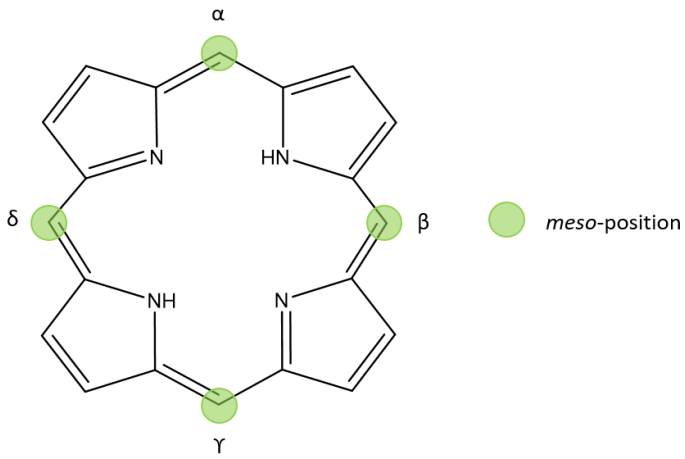


Figure 1.11: Schematic illustration of Fisher's numeration of meso-carbons.

### 1.4.4 Porphyrins as photosensitizers

Light with a short wavelength is used in direct antimicrobial treatment. However, irradiation with short wavelengths such as UV may not only kill bacteria but also damage healthy cells and tissue. The wavelength of a therapeutic source is therefore important. This side effect is avoided by using PDT/PDI, where ROS is produced under visible light illumination. It has been reported that this method can effectively kill bacteria/tumors without damaging the mammalian cell. The success of damaging bacteria is highly dependent on the chemical structure and electric charge of the photosensitizer (PS) molecule [14, 46]. Moreover, PDT has high efficiency, low toxicity,

and a short duration of action, which makes them minimally invasive on healthy tissues [47]. Similar results have also been reported for porphyrin-based material used in PDI [48].

In biomaterials, the penetration depth is dependent on the wavelength used. The lower energy red light has a deeper penetration than blue light [49], which can be used to design photosensitizers for a particular use. Porphyrin is an excellent photosensitizer as the bandgap can be tuned by incorporating metal-ions. For PDT, a red light absorbing photosensitizer is required, due to its large penetration depth in organic matter. While this is less important in PDI and for surface treatments where penetration depth is of less concern. Photosensitizers used in organic matter need to be biocompatible. Several papers have reported that porphyrin-based material shows good biocompatibility [50-52].

A downside with PDI/PDT is that there is a challenge in the long-term use of porphyrin since it can become photobleached under illumination. A strategy that has been proven to prolong the lifetime and increase the stability of the porphyrins is by incorporating other antimicrobial agents. The addition of antimicrobial agents to photosensitizers may also increase the efficacy of killing bacteria. Lyutakov et al. [53] reported that porphyrin with the addition of silver nanoparticles would increase porphyrin stability at the expense of decreasing the ROS production. Nevertheless, the material showed great results in killing both gram-negative and gram-positive bacteria. In addition, incorporating porphyrins with metals is reported to increase its stability, henceforward, also increase the lifetime of the material [54, 55].

### 1.4.5 Porphyrin used in this thesis

The porphyrin used in this thesis is 4,4’,4’’,4’’’-(porphine-5,10,15,20-tetryl)tetrakis(benzoic acid), abbreviated as TCPP (Figure 1.1). TCPP as powder yields a color from dark blue to purple to black. The powder is soluble in water and ethanol. The negatively charged carboxylate form of TCPP can be coordinated with cations in the center or the peripheral positions.

## 1.5 Previous work

This section presents some of the prior works related to antibacterial materials. The synthesis of porphyrins-based materials will be presented, followed by the evaluation of different

porphyrin systems against gram-positive and gram-negative bacteria. Lastly, attention will be given to known antimicrobial materials against gram-positive *E. faecalis*.

### 1.5.1 Fabrication of porphyrin-based material

There are various methods reported in the literature for synthesizing porphyrin-based materials. Some of the most common methods reported are solvothermal/hydrothermal synthesis [56]. Table 1.1 contains an overview of selected works, focusing on reported porphyrin-based materials and the following synthesis (especially the use of TCPP porphyrin and zirconium as the metal-ion [50, 52, 57, 58]. Note that some of the presented materials in this section are also evaluated for PDI, which is presented in the next section.

Porphyrin-based materials have been synthesized using the hydrothermal/solvothermal approach at temperatures between 80 and 120 °C from 4 to 24 hours [50, 56, 59-61]. An interesting discovery from Jiang et al. [61] is that the metal-organic frameworks (MOFs) materials such as PCN-225 (ZrTCPP MOF) and PCN-225(Zn) exhibits high chemical stability in aqueous solutions with a pH ranging from 1 to 11. Other papers have also reported that porphyrin-based nanoparticles have high stability in water, contrary to irregular porphyrin aggregates that are prone to grow into larger agglomerates [51, 58]. Jiang et al. [61] reported that the fabrication of the porphyrin material was conducted by a solvothermal synthesis heated at 120 °C for 12 hours. Furthermore, they suggested that the porphyrin is prone to protonation as function of pH and concluded that PCN-225 can be used for pH sensing [61]. It is challenging to produce phase-pure ZrTCPP MOFs due to a high degree of polymorphism. In 2019, the group Shaikh et al. [62] explored the synthesis of these MOFs also by solvothermal synthesis at 120 °C for 16 hours. Their work identified three different types of phase-pure ZrTCPP MOFs, PCN-222, PCN-223, and MOF-525 (Figure 1.12). They revealed that the framework formation is controlled by adjusting TCPP and modulators with different concentrations and acidity. In addition, they suggested that the MOFs formation might also be affected by the steric effect and miscibility with the reaction solvent. They concluded that MOF-525 is a less stable phase than the others due to formation under rapid conditions [62].

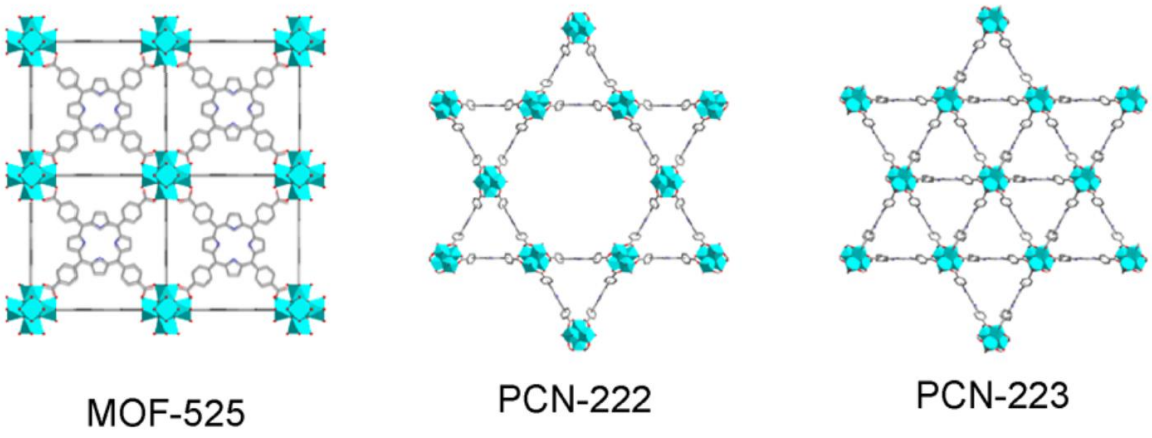


Figure 1.12. Illustration of Zr-MOFs structure based on meso-tetra(4-carboxyphenyl)porphyrin (TCPP). Adapted from [62].

Several papers have synthesized the porphyrin-based material PCN-224 (ZrTCPP). The approach is quite similar, as the synthesis involves solution-based method or solvothermal method. Nie et al. [52] and Zhang et al. [57] used a solution-based method approach, with heating to 90 °C for 5 hours under stirring to create PCN-224 MOF nanoparticles. Han et al. [58] used a similar approach, however, they used a higher temperature and longer time, 120 °C and 24 h. Another group, Chen et al. [50] explored the synthesis of PCN-224 nanoparticles by solvothermal methods. The solution was heated to 120 °C for 1 h in DMF, which is significantly shorter in comparison to the other papers.

In 2013, So et al. [63] reported an interesting route for synthesizing porphyrin-based materials (L2-MOF and DA-MOF). DA-MOF was synthesized from [5,15-di(4-pyridylacetyl)-10,20-diphyenyl]porphyrinatonzinc-(II), (1,2,4,5-tetrakis(4 carboxyphenyl)benxene], and zinc-(II)acetate($Zn_2^{4+}$), whereas L2-MOF was synthesized from 4,4'-bipyridine, 5,10,15,20-tetrakis(4-carboxphenyl)porphyrin, and $Zn_2^{4+}$. They explored the use of a layer-by-layer liquid approach to synthesize thin films based on porphyrin, which is different from the common synthesis of these materials. This method involves a much milder condition for synthesis, where the highest temperature applied is 40 °C. They suggested that the mild conditions provided the incorporation of free-base porphyrins in MOF. Furthermore, the thickness can be controlled by the number of cycles. The films can be used for light-harvesting and efficient energy carriage in solar energy devices.

Fabrication of porphyrin-based materials with metal cations is generally divided into two main strategies: coordination of the metal at the meso-substituted functional groups such as carboxylate, or metalation of the porphyrin core. As mentioned earlier, So et al. [63] reported non-metallated porphyrin in MOF and confirmed this by optical measurements. Characterization of the incorporation of metal-ions on porphyrin-free bases can be performed by UV-Vis absorption spectra. As seen in Figure 1.13, they suggested that the porphyrin is a free base according to the obtained four Q-bands. Similar results have been reported by Mu et al. [64] and Liu et al. [65], which is in contrast to Ribeiro et al. [66] that reported the two Q-bands is in accordance with a free-base unsymmetrical porphyrin. Furthermore, Han et al. [58] reported that when TCPP was metallated, the four Q-bands turned into two bands because of the increased symmetry in the macrocycle. Other papers have also been using UV-Vis absorption to characterize the porphyrin-based material leaned on redshift or blue shift. Sun et al. [67] reported the successful fabrication of 2D nanosheets of TCPP and metals as the Soret band of porphyrin at 416 nm in the free TCPP became redshifted when incorporated with metals (Zr, Zn, and Cu), as seen in Figure 1.14. The redshift of the Soret band with the addition of broadening is also observed when nanoparticles of porphyrin-based material are immersed in water [68]. A redshift of the Soret band indicates J-aggregation, which is structured in a head-to-tail fashion, where the planes are stacked side-by-side [69]. An interesting report from Zhang et al. [57] states that incorporating of Ag atoms into a ZrTCPP MOF frame did not show any significant change in the UV-Vis absorption spectra. They suggested that this indicates a successful incorporation of Ag into the MOF without changing the original framework.

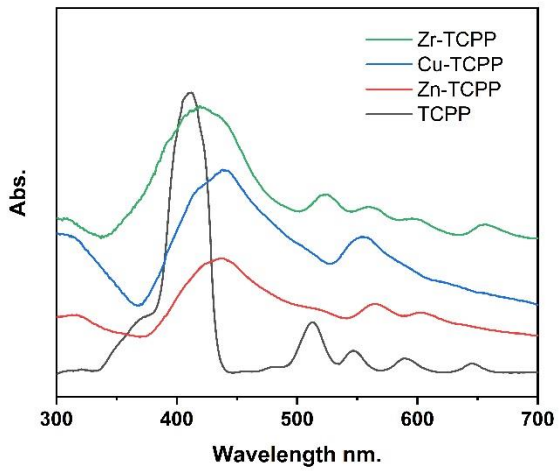


Figure 1.13: UV–Vis absorption spectra of TCPP, Zn-TCPP, Cu-TCPP and Zr-TCPP. Image from [67].

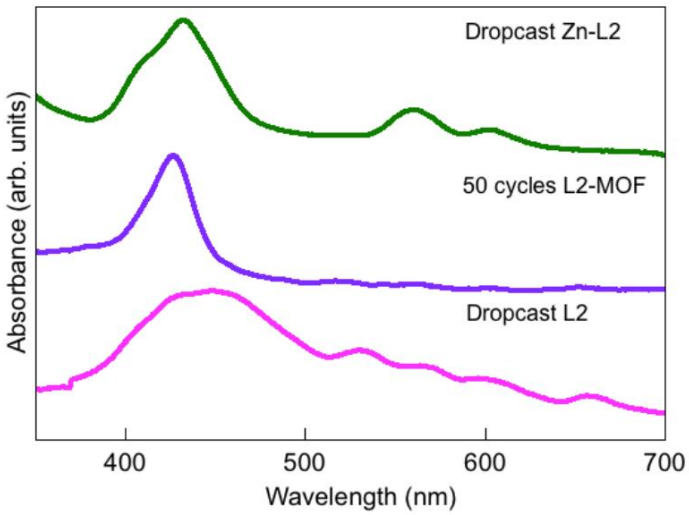


Figure 1.14: Comparison of UV-Vis spectra of L2 porphyrin in the drop-cast form (magenta), 50 cycles of L2-MOF film (purple), and drop-cast Zn-L2 (dark green). These samples were deposited onto transparent ITO glass. Image from [63].

**Table 1.1 Overview of reported synthesis of porphyrin-based materials**

| System | Methods | Reaction time (h) | Highest Temp. used in the synthesis (°C) | Growth | Shape | Characterization techniques | Ref |
|---|---|---|---|---|---|---|---|
| Zn-TCPP | One-pot solvothermal synthesis | 16 | 80 | 2D | Nanosheets | TEM, AFM, PXRD, UV-Vis absorption, FL | [67] |
| Cu-TCPP | One-pot solvothermal synthesis | 16 | 80 | | | | |
| Zr-TCPP | One-pot solvothermal synthesis | 24 | 120 | | | | |
| ZPM@Ag(2) | ZPM: solvothermal synthesis | 24 | 120 | 3D | Nanoparticles | SEM, TEM, XRD, FTIR, XPS and BET analysis, DRS, PL, ESR | [56] |
| | | 4 | 80 | | | | |
| | ZPM@AG(2): hydrothermal synthesis | 4 | 80 | | | | |
| DA-MOF | Layer-by layer synthesis in liquid | - | 40 | 3D | Thin film | SE, SEM, AFM, UV-Vis absorption, fluorescence polarization | [63] |
| L2-MOF | | | | | | | |

| | | | | | | | |
|---|---|---|---|---|---|---|---|
| PCN-225 | Solvothermal synthesis | 12 | 120 | 3D | Single crystals | PXRD, TGA, FTIR, SEM, EDS, fluorescence | [61] |
| PCN-225(Zn) | Solvothermal synthesis | 12 | 120 | | | | |
| PCN-224 | Solution based | 5 | 90 | 3D | MOFs | SEM, TEM, contact angle, FTIR, XRD, EDS, UV-Vis, Fabric strength tester, TGA, DTG, DPBF | [52] |
| PCN-WFC | In situ growth method | 5 | 90 | | | | |
| PCN-224 | Solution based | 5 | 90 | 3D | Nanoparticles | SEM, TEM, XRD, FTIR, XPS | [57] |
| PCN-224-$Ag^{+}$ | Solution based | overnight | - | | | | |
| PCN-224-Ag-HA | Solution based | 4 | Room temperature | | | | |
| PCN-224 | Solvothermal synthesis | 1 | 120 | 3D | Nanoparticles | SEM, TEM, XRD, Photoluminescence (PL), HR-TEM, EDS, XPS | [50] |
| PCN-224(Ti/Zr) | Solvothermal synthesis | - | 120 | | | | |
| PCN-222 | Solvothermal synthesis | 16 | 120 | 3D | Polycrystallines | PXRD, SEM, $^{1}$H NMR Analysis, TGA, Gas Adsorption Isotherms, ICP-MS | [62] |
| PCN-223 | Solvothermal synthesis | 16 | 120 | | | | |
| MOF-525 | Solvothermal synthesis | 16 | 120 | | | | |
| PCN-222 | Solvothermal synthesis | 16 | 120 | 3D | MOFs | SEM, TEM, PXRD, DSC, FTIR, and $N_2$- adsorption-desorption | [59] |
| PCN-222 | Solvothermal | 48 | 120 | 3D | MOFs | NMR, FTIR, PXRD, SEM, EDS, TGA, ICP-MS, XPS, MST, UV-Vis, Fluoresecene , RET, PET | [65] |
| | | 24 | 130 | | | | |
| PTTP-Glu-Ac Nps | Nanoreprecipitation method | 96 | Room temperature | 3D | Nanoparticles | UV-Vis, SEM, TEM,$^{1}$H NMR, $^{13}$C-NMR, FTIR, GPC, ESI-MS spectrometry, PL | [68] |

| | | | | | | | |
|---|---|---|---|---|---|---|---|
| Por-2a (porphyrin-cyclodextrin) | Solution based | - | 80 | 3D | - | $^{1}H$, $^{19}F$ NMR, ESI-MS, UV-Vis Absorption, TLS | [66] |
| Por-3a (porphyrin-cyclodextrin) | | | | | | | |
| TCPP-TG | Solution based | 12 | 35 | 3D | Cationic Nanoparticles | UV-Vis, FTIR, SEM, TEM, Fluorescence, ESR, NMR | [51] |
| | | 24 | 35 | | | | |
| MNPNH-TCPP | Coprecipitation method | - | 80 | 3D | Nanoparticles | UV-Vis, FTIR, TEM | [69] |
| MNPSiNH-TCPP | | | | | | | |
| $Cu_{10}$MOF (MOF = PCN-224) | Hydrothermal synthesis | 10 | 130 | 3D | MOFs | SEM, TEM, EDS, DLS, XRD, FTIR, UV-Vis NIR absorption, XPS, Photocurrent and electrochemical impedance spectroscopy, PL | [58] |
| $Cu_{25}$MOF (MOF = PCN-224) | | | | | | | |
| PCN-224 | Solvothermal | 24 | 120 | | | | |
| Zn-TCPP | One-pot Hydrothermal synthesis | 24 | 80 | 3D | MOFs | PXRD, UV-Vis NIR absorption, DLS, Fluorescence imaging, TEM, FTIR, Thermogravimetric analysis | [60] |
| GMOF-LA( ZrTCPP, Au NPs, L-Argininge (L-arg) | Solvothermal and in situ growth | 20-24 | 120 | 2D | MOFs nanosheets | TEM, XRD, EDX, AFM, ICP-OES, FTIR, CLSM | [64] |

### 1.5.2 Antibacterial porphyrin-based materials in the literature

TCPP has shown to be an attractive choice as the active material for PDI method [50, 52, 67]. In 2020, Li et al. [51] investigated cationic porphyrin-based nanoparticles for the inactivation of bacteria. They suggested that the activity of TCPP porphyrin could be enhanced by incorporating triaminoguanidinium chloride (TG) to synthesize TCPP-TG NPs. The electron

spin resonance confirmed that TCPP-TG had a higher singlet oxygen production than pure TCPP. The bacteria used in the paper were gram-negative *E. coli* and gram-positive *S. aureus*. The photoactivation experiment shows that both TCPP and TCPP-TG NPs yield a bactericidal effect against *S. aureus*. Moreover, the experiment shows that TCPP-TG is superior to TCPP and was able to exhibit a bacterial reduction of > 6 log with only 4 min of visible light irradiation against *S. aureus*. Furthermore, only TCPP-TG NPs with light radiation showed a promising bactericidal effect against the gram-negative *E. coli* with a > 6 log bacterial reduction within 6 min of irradiation. This is exceptionally fast, as it has been reported by others authors that it takes 45 min to achieve a 6 log bacterial reduction of *E. coli* [52]. Li et al. [51] concluded that TCPP-TG has a great potential for use in PDI against both negative and positive bacteria, as a consequence of higher production of singlet oxygen, increased water solubility, and enhanced bacteria adhesion. Furthermore, TCPP-TG also showed great biocompatibility [51]. This proves that the activity of TCPP is enhanced by the incorporation of other components.

Khan et al. [68] created porphyrin-based nanoparticles with poly-5,15-diphenyl(2,5′-dithienylene)-10,20-di(3,5-di-O-TEG-tetra-O-acetyl-D-galactopyranoside-phenyl)porphyrin (PTTP-Glu-Ac) ( Figure 1.15). They demonstrated that the nanoparticles exposed to white light induce a strong antibacterial effect against both gram-negative and gram-positive bacteria. In this work, they used *E. coli* and *B. subtilis*. The bacteria suspension was incubated with NPs (18 $\mu gmL^{-1}$) for 15 min in the dark and irradiated with white light for ten minutes with a flux of 22 $mWcm^{-2}$. They discovered that the killing effect against *E. coli* is 99% effective with radiation and 8% in a dark mode. In addition, the higher concentration of NPs also increases bactericidal effect and reaches a maximum at 18 $\mu gmL^{-1}$. Similar findings were reported for the positive bacteria *B. subtilis*. They also concluded that the interaction between the NPS and the bacteria is probably hydrophobic [68]. Porphyrin-based nanoparticles have also been proven in other papers to exhibit inactivation of both gram-negative and gram-positive bacteria by radiation of visible light [50, 52, 56, 57]. However, the use of nanoparticles can also contaminate the environment. The group of Scanone et al. [69] investigated the photodynamic inactivation of porphyrin-based materials with magnetic nanoparticles (MNP). The magnetic nanoparticles were used for immobilizing PS, exploring the possibility of recovery from the environment and reuse by applying a magnetic field. Furthermore, they applied the salt of anthracene derivative tetrasodium-2,2'-(anthracene-9,10-diyl)bis(methylmalonate) (ABMM) in water for the detection of singlet oxygen production. The TCPP induced with MNP had a lower singlet oxygen production than only TCPP as predicted. The bacteria used in the paper

were gram-positive *S. aureus* and gram-negative *E. coli*, and in addition a yeast, *C. albicans*. They reached a 3.0 log decrease in cell survival after 30 min of irradiation against *S. aureus* with MNPSiNH-TCCP and MNPNH-TCPP. With the same condition, MNPSiNH-TCCP reached a reduction of 3.1 log in cell survival against *E. coli*. Against yeast *C. albicans*, MNPSiNH-TCCP showed a 2.1 log decrease in cell survival. In conclusion, both MNP incorporated with TCPP showed great inactivation of bacteria with light irradiation. The remarkable difference between these two MNP is the use of recycling. The MNP with the addition of Si showed a much higher antibacterial effect after recycling. They suggested that this is because the silicon coating is protecting the magnetic core from oxidation [69]. NPs of porphyrin-based material are shown to exhibit a significant bacterial reduction of both gram-positive and gram-negative bacteria, which depends on the concentration of the material.

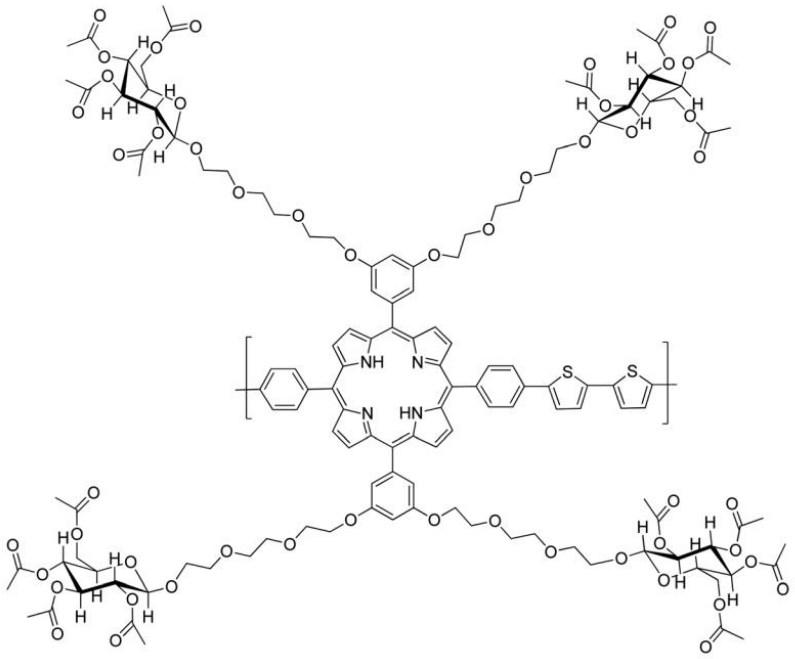

Figure 1.15: Chemical structure of PTTP-Glu-Ac. Adapted from [68].

In 2020, Ribeiro et al. [66] demonstrated that cyclodextrin-porphyrin compounds inactivate *E. coli* bacteria. They created two cationic compounds with the conjugation of a cyclodextrin unit with porphyrin and called them Por 2a and Por 3a. These materials were tested against *E. coli* under white light with an irradiance of 25 $mWcm^{-2}$ and a concentration of 5.0 μM. They observed no evidence of bactericidal effect under dark mode (non-irradiation of the sample). No inactivation of bacteria under dark mode has also been reported by Nie et al. [52] and among others [50, 51, 57, 66]. However, a small amount of dark toxicity has been reported for porphyrin-based material by Khan et al. [68] and Han et al. [58]. Furthermore, Ribeiro et al.

[66] reported that under 20 min exposure to light (400-700 nm), both of the materials (Por 2a and Por 3a) exhibited a bacterial reduction of 3.9 log and 4.0 log against *E. coli*. The Por 3a had a faster inactivation profile than Por 2a, which they concluded is probably due to the fact that Por 3a is a better singlet generator and that Por 2a is less soluble in water than Por 3a [66]. The radiation exposure time used by Ribeiro et al. [66] is significantly shorter than Mao et al. [56], which used 60 min of irradiation exposure time to reduce *E. coli* by 99.7% using ZPM@Ag NPs (ZrTCPP MOF with Ag nanoparticles). This shows that the porphyrin-based materials usually do not exhibit bactericidal effects without light irradiation, and the effect is increased when the material is a powerful singlet generator.

In the paper by Han et al. [58], they incorporated Cu-ions into PCN-224 MOF to enhance its properties for antibacterial effects. The incorporation of Cu-ions gives better photocatalytic property and photothermal effect. The bacteria used in this paper are *S. saureus* and *E. coli*. $Cu_x$MOF shows a bactericidal effect. They reported the highest bacterial reduction of 99.71% against *S. aureus* (see table 1.2 for more data) with 20 min light irradiation (660 nm). Moreover, it was observed that the concentration of Cu-ions had a significant role in the bactericidal effect, as there is a limit of concentration that exhibited the highest bacterial reduction [58]. This was also observed by Mao et al. [56] that from 10 mg to 20 mg of ZPM@Ag NPs a significant increase in bacterial reduction was observed. However, from 20 to 40 mg of ZPM@Ag NPS there was no significant change in bacterial reduction. Another paper has also taken the same approach by incorporating other metals ions into PCN-224. In 2020, Chen et al. [50] incorporated titanium into ZrTCPP MOF. Firstly, they investigated the ROS producing capacity. They used the assay kit 2'-7'dichlorofluorescin diacetate (DCFH-DA) as the indicator to investigate the optimal concentration of PCN-224(Ti/Zr) NPs for ROS generation. The concentration showing the highest ROS production after irradiation with a visible light source (200 $mWcm^{-2}$) for 3 minutes was 50 $\mu gml^{-1}$. In addition, the indicator showed three times higher ROS production for the PCN-224 with the addition of Ti than pure PCN-224. The material was tested against bacteria gram-positive (*S. aureus* and *S. epidermidis*) and gram-negative (*E. coli* and *A. baumannii*), and their corresponding multiple drug-resistant. They discovered that with the radiation from white light, the PCN-224(Ti/Zr) was able to reduce the bacteria with about 96%. In addition, they discovered that the antibacterial effect is stronger when PCN-224 is incorporated with titanium. Furthermore, they concluded that PCN-224(Ti/Zn) has a great biocompatibility and hence, it has a potential use in medical therapy [50]. The antimicrobial

properties of ZrTCPP MOFs (PCN-224) have been demonstrated to be enhanced by incorporating additional metal ions into the structure.

Nie et al. [52] incorporated PCN-224 with woven cotton fabrics (WFC) to create PCN-WFC. They achieved a bacterial reduction of 6 log for both gram-positive and gram-negative bacteria with irradiation of visible light for 45 min. This group observed an interesting connection between the exposure time of irradiation and bacterial reduction. PCN-WFC was incubated with *E. coli* ($10^8$ $CFUml^{-1}$) for 1 h, followed by irradiation for 15 min, 30 min, and 45 min, and exhibited a bacterial reduction of 0, 1.52 log, and 6 log, respectively. This light exposure dependency was also observed by Scanone et al. [69]

**Table 1.2: Overview of porphyrin-based materials evaluated for antimicrobial properties.**

| **System** | **Concentration** | **Microbial culture** | **Inoculum concentration ($CFUml^{-1}$)** | **Exposure time (min)** | **Incubation time** | **Flux ($mWcm^{-2}$)** | **Light source** | **Light mode** | **Dark mode** | **Ref** |
|---|---|---|---|---|---|---|---|---|---|---|
| Por- 2a | 5 µM | *E. coli* | $10^7$ | 20 | 15 min in the dark | 25 | 400-700 nm | 3.9 log | No inactivation | [66] |
| Por- 3a | 5 µM | | $10^7$ | 10 | 15 min in the dark | 25 | | 4.0 log | No inactivation | |
| PTTP-Glu-Ac Nps | 18µgm$L^{-1}$ | *E. coli* | - | 10 | 15 min in the dark | 22 | White light | 99% | 8% | [68] |
| | | *B. subtilis* | | | | | | 98.97% | 8.19% | |
| ZPM@Ag(2) (zirconium porphyrin MOF, Ag nanoparticles | 200 mg $L^{-1}$ | *E. coli* | $10^6$ | 60 | - | - | Visible light | 99.7% | - | [56] |
| | | *S. aureus* | | | | | | 97.3% | | |
| PCN-224 | - | - | - | - | - | - | Visible light | - | - | [52] |
| PCN-WFC | - | *P. aeruginosa* | $10^8$ | 45 | 1 h | - | | 6 log | No inactivation | |
| | - | *E. coli* | $10^8$ | 15 | 1 h | | | No inactivation | No inactivation | |
| | - | | | 30 | | | | 1.52 log | | |
| | - | | | 45 | | | | 6 log | | |
| | - | *S. aureus* | $10^8$ | 45 | 1 h | | | 6 log | No inactivation | |

| | | | | | | | | | | |
|---|---|---|---|---|---|---|---|---|---|---|
| | - | *B. subtilis* | $10^8$ | 45 | 1 h | | | 6 log | No inactivation | |
| PCN-224 | 60 μgmL$^{-1}$ | *S. aureus* and *E. coli* | $10^6$ | 15 | 30 min | - | Visible light | Inactivation | No inactivation | [57] |
| PCN-224-Ag$^+$ | 60 μgmL$^{-1}$ | | $10^6$ | 15 | 30 min | - | | Inactivation | No inactivation | |
| PCN-224-Ag-HA | | | $10^6$ | 15 | 30 min | - | | Inactivation | No inactivation | |
| PCN-224(Ti/Zr) | 50 μgmL$^{-1}$ | MRSA ( methicillin-resistant *S. aureus*) | $10^5$ | 30 | - | - | Visible light | 96.8% | No inactivation | [50] |
| PCN-224(Ti/Zr) | 50 μgmL$^{-1}$ | MRSE (methicillin-resistant *S. epidermidis*) | $10^5$ | 30 | - | - | | 96.2% | No inactivation | |
| | 50 μgmL$^{-1}$ | *E. coli* | $10^5$ | 30 | - | | | 96.4% | No inactivation | |
| | 50 μgmL$^{-1}$ | *A. baumannii* | $10^5$ | 30 | - | | | Inactivation | No inactivation | |
| TCPP-TG | 8 μM | *E. coli* | - | 6 | 30 min in the dark | 8 | Visible light | > 6 log | No inactivation | [51] |
| | 6 μM | *S. aureus* | | 4 | | | | | | |
| MNPSiNH-TCPP | 1 mgmL$^{-1}$ | *S. aureus* | $10^6$ | 30 | 30 min in the dark | 90 | 660 nm | 3.0 log | No (minimal) inactivation | [69] |
| | | *E. coli* | $10^6$ | 30 | 30 min in the dark | 90 | | 3.1 log | | |
| | | Yeast *C. albicans* | | | | | | 2.5 log | | |
| $Cu_{10}$MOF (MOF = PCN-224) | 1.5 mg/mL | *S. aureus* | 5 x $10^7$ | 20 | - | 400 | 660 nm | 99.71% | 15.53% | [58] |
| | | *E. coli* | | | | | | 97.71% | 18.06% | |
| $Cu_{25}$MOF (MOF = PCN-224) | 2.5 mg/mL | *S. aureus* | | | | | | 92.89 % | 21.39% | |
| | | *E. coli* | | | | | | 83.41% | 28.69% | |
| PCN-224 | 0.5 mg/mL | *S. aureus* | | | | | | 96.01% | - | |
| | | *E. coli* | | | | | | 91.76% | - | |

### 1.5.3 Antibacterial activity against bacteria *E. faecalis* in literature

In this section, some literature for the inactivation of gram-positive bacteria *E. faecalis* will be introduced. *E. faecalis* can cause problems in dental health, and concern endodontics. For a more detailed description of the bacteria, see section 2.2.4. The irrigant sodium hypochlorite (NaOCl) is the most commonly used for the inactivation of *E. faecalis* in dental health. However, NaOCl in the root canal in high concentration can increase the risk of cytotoxicity and neurotoxicity [70]. Better methods are therefore needed to fight these bacteria. The efficacy of antimicrobial action may vary depending on different factors, such as bacteria strain, exposure time, light dose, and concentration. Thus, the results reported by various authors may have been influenced by a range of factors as there are no standardized method of performing the experiments. Hence, when evaluating reports on the effects of different systems against *E. faecalis*, this has to be taken into consideration.

In 2018, Wang et al. [71] reported that 3-phenyllactic acid (PLA) has antimicrobial activity against *E. faecalis*. They suggested that PLA damages the cell membrane and leads to leakage of intracellular components. Furthermore, they reported that the antimicrobial activity depends on the concentration of PLA, and the exposure time of PLA to *E. faecalis*. PLA solutions of 5 and 10 mg/ml were exposed to the bacteria for 60 and 30 min, respectively, and results in a bacteria reduction of $\geq 6$ log $CFUml^{-1}$ [71]. The concentration dependency of antimicrobial activity was also later explored by Huang et al. [72] in 2019. This group reported a new type of sensitizers that is distinct from other photosensitizers like porphyrins. Instead of being activated by visible light, these sensitizers can be activated by UV-light, X-rays, microwaves, and ultrasound to produce ROS. Copper-cysteamine (Cu-Cy) NPs with 10, 50, and 100 μM were evaluated against *E. faecalis* under UVA radiation at 360 nm. The result was a bacteria reduction of 1 log, 3 log, and 100%, respectively. In addition, they reported no inactivation of bacteria without light irradiation. Such light dependent were also reported by Ghaffari et al. [73] and Silva Garcez et al. [74]. Cheng et al. [75] reported an increase in bacterial reduction with the increase of exposure time. This group study the phage-derived lysins from isolated *E. faecalis* and name the substance LysEF-P10. It was reported that this phage only affected *E. faecalis* and not other bacteria such as *E. faecium*. It could be switched between active and inactive states by calcium. LysEF-P10 exhibits a bacterial reduction of 4 log with 10 min of exposure to the bacteria without irradiation. The efficiency can be increased by the exposure of 60 min that exhibited a bacterial reduction of 7 log [75]. The dependency of concentration of

the antibacterial material and exposure time to the bacteria are also crucial for non-porphyrin-based material.

In 2013, Yildirim et al. [70] studied the antimicrobial efficiency of PDT of methylene blue (MB), and 5% NaOCl. In this study, they evaluated the antimicrobial efficiency of MB with *E. faecalis* under 660 nm radiation within 1, 2, and 4 min. 1 min irradiation shown a bacterial reduction of 99.8%, while 2 and 4 min resulted in 99.9%. NaOCl has also shown a bacterial reduction of 99.9% with 15 min of exposure time to *E. faecalis*. The results of MB as PDT is not consistent with a later paper in 2017 by Sebrão et al. [76]. This paper reported that 31.2 μmol/L of the MB group under the radiation of 660 nm for 3 min against *E. faecalis* showed no significant reduction of bacteria in comparison to the control group. However, they reported that 25 μmol/L of the rose bengal group (RBG) under the radiation of 523 nm for 3 min against the same bacteria strain, showed a bacterial reduction of 95.67% [76]. In contrast, the reported antimicrobial efficiency of 5% NaOCl by Yildirim et al. [70] was more consistent with Pourhajibagher et al. [77] and Silva Garcez et al. [74]. Pourhajibagher et al. [77] reported that 5.25% NaOCl has a bacterial reduction of 92.6% against *E. faecalis* biofilm. Against the same bacteria strain, it was reported by Silva Garcez et al. [74] that 0.5% NaOCl shown a bacterial reduction of 97.06% with an exposure time of 8 min. On overall, notable variations in antimicrobial efficiency for relatively similar experiments are reported, here with variations from ca. 1 to 3 log activity for relatively similar experiments.

It has been established that biofilm is harder to remove than the planktonic form of the bacteria. In 2018, Khoobi et al. [78] reported that curcumin (CUR)-aPDT shown antibacterial effect against both forms of *E. faecalis*: planktonic and biofilm. CUR-aPDT exhibited a bacterial reduction of 95.0% and 41.2% against planktonic and biofilm *E. faecalis*, respectively, with radiation from the LED light. This concluded that biofilm is harder to remove than the planktonic form of bacteria. Similar results were also reported by Pourhajibagher et al. [77]. They reported that CUR had a lower bacterial reduction against *E. faecalis* with 90.2%. However, they achieved over two times higher bacterial reduction against biofilm *E. faecalis* with 83.6% in comparison to what Khoobi et al. [78] reported. Furthermore, a similar trend was also reported for indocyanine green (ICG) used in PDT. The ICG was also evaluated against planktonic and biofilm *E. faecalis* and showed a bacterial reduction of 82.5% and 75.2%, respectively.

**Table 1.3. Overview of antibacterial activity against *E. faecalis*.**

| System | Bacteria strains | Concentration | Inoculum concentration ($CFUml^{-1}$) | Exposure time (min) | Incubation time | Flux ($mWcm^{-2}$) | Light dose ($Jcm^{-2}$) | Light source | Light mode | Dark mode | Ref. |
|---|---|---|---|---|---|---|---|---|---|---|---|
| 3-Phenyllactic acid (PLA) | *E. faecalis* | 10 mg/mL | - | 30 | - | - | - | . | ≥ 6 log | - | [71] |
| | *E. faecalis* | 5 mg/mL | | 60 | | | | | | | |
| Copper-cysteamine(Cu-Cy) NPs | *E. faecalis* | 100 μM | $10^8$ | 10 | 30 min in the dark | 16 | 10 | UVA (360 nm) | 100% | No inactivation | [72] |
| | | 50 μM | | | | | | | 3 log | | |
| | | 10 μM | | | | | | | 1 log | | |
| | *E. coli* | 100 μM | | | | | | | < 1 log | | |
| | MRSA | 100 μM | | | | | | | >6 log | | |
| | | 50 μM | | | | | | | 2 log | | |
| | *A. baumannii* | 100 μM | | | | | | | < 1 log | | |
| Curcumin(CUR)-aPDT | *E. faecalis* | 40 μM | $1.0 \times 10^6$ | - | 5 min in the dark | 1000-1400 | 72 | LED ( 450 nm ± 30 nm) | 95.0% | - | [78] |
| | Biofilm *E. faecalis* | | | | | | | | 41.2% | | |
| | *P. aeruginosa* | | | | | | | | 81.1% | | |
| | Biofilm *P. aeruginosa* | | | | | | | | 30.2% | | |
| Rose Bengal group (RBG) | *E. faecalis* | 25 μmol/L | $3x\ 10^8$ | 3 | 5 min in the dark | - | 204 | 523 nm | 95.67% | - | [76] |
| Methylene blue group (MBG) | | 31.2 μmol/L | | 3 | | | | 660 nm | No significant inactivation | | |
| 0.2% CHX | *E. faecalis* biofilm | - | $1.0 \times 10^5$ | - | 5 min in the dark | - | - | - | 65.3% | - | [77] |
| 2.0% CHX | *E. faecalis* biofilm | - | | - | | - | - | - | 81.0% | - | |
| 5.25% NaOCl | *E. faecalis* biofilm | - | | - | | - | - | - | 92.6% | - | |
| CUR | *E. faecalis* | 40 mM | | 5 | | - | 360 | 450 nm | 90.2% | - | |
| | *E. faecalis* biofilm | 40 mM | | 5 | | - | 360 | 450 nm | 83.6% | - | |
| Indocyanine green(ICG) | *E. faecalis* | 1000 μg/mL | | 1 | | - | 31.2 | 810 nm | 82.5% | - | |
| | *E. faecalis* biofilm | 1000 μg/mL | | 1 | | - | 31.2 | 810 nm | 75.2% | - | |
| Toluidine Blue Ortho(TBO)/KI | *E. faecalis* | 10 μM TBO/10m M KI | - | 3 | 30 min | - | 40.9 | 635 nm | >4 log | No inactivation | [73] |
| LysEF-P10 (phage-derived lysin from *E. faecalis*) | *E. faecalis* | 20 μg/mL | $10^8$ | 10 | 1 h | - | - | - | 4 log | - | [75] |
| | | | | 60 | | | | | 7 log | | |

| | | | | | | | | | | | |
|---|---|---|---|---|---|---|---|---|---|---|---|
| L+AZ+ (laser light + azulene paste) | *E. faecalis* | - | 4 x $10^7$ | 3 | 5 min | - | - | 685 nm | 99.89% | No inactivation | [74] |
| 0.5% NaOCl | | | | 8 | - | | | - | 97.06% | - | |
| NaOCl | *E. faecalis* (in root canals) | - | 2.58 x $10^8$ | 15 | - | - | - | - | 99.9% | - | [70] |
| Methylene blue (MB) | | | | 1 | 1 min | | | 660 nm | 99.8% | | |
| | | | | 2 | | | | 660 nm | 99.9% | | |
| | | | | 4 | | | | 660 nm | 99.9% | | |

Based on the prior work presented so far, the overall results scatter greatly due to the lack of standardized methods for determining bioassay. Our approach will be to follow the same procedures as for Olsen's work aid for a better comparison to that work. We will pay particular attention to how light and dark affect the bioassay and on that note, we will also explore the bacterial reduction at different light doses, which have been demonstrated to increase the bacterial reduction. In addition, the concentration of antibacterial materials have been presented to increase the bactericidal effect, which we would take into account when evaluating the bacteria assay of ZrTCPP thin film with different layers.

# 2 Theory

This chapter is divided into two parts. The first parts will give some relevant theories of photochemistry and give a deeper understanding of the energy transfer mechanism that leads to ROS production. The second part will focus on bacteria, bacteria growth and biofilm formation.

## 2.1 Porphyrin-based material for inactivation of bacteria

As already mentioned, porphyrins are widely used as sensitizers for the inactivation of bacteria through photodynamic therapy. However, it should be noted that not all materials that absorb light can function as photosensitizers. In fact, most materials lose the energy that is absorbed by converting it to heat. This section will provide the basic principles of photodynamic theory and explain how the excited state of a porphyrin is able to induce photochemical processes instead of converting it to heat.

### 2.1.1 Basic photochemistry

Photochemistry is the part of chemistry concerned with photochemical reactions between light and molecules, and it can be divided into two basic laws. The first law comprehends that a chemical substance must absorb light in order to induce a photochemical reaction. This step is also known as the principle of photochemical activation or Grotthuss-Draper law. The second law is the Stark-Einstein law or also called the photochemical equivalence law. This law formulates that only a single quantum or photon of light is absorbed by each molecule [36] (p. 9-10).

The efficiency of a PS in a photochemical process is determined by singlet oxygen quantum yield, Φ. The singlet oxygen quantum yield is defined as the number of ROS produced per photon of light absorbed [36] (p. 11) :

$$\Phi = \frac{Number\ of\ ROS\ produced}{Number\ of\ photons\ absorbed\ by\ the\ PS}$$

### 2.1.2 Energy diagram

A Jablonski diagram illustrates the electronic states of a molecule and the transition of energy between these states. Accordingly, it describes the various types of non-radiative and radiative transitions in a molecule. The vertical axis consists of energy levels, and the horizontal lines represent electronic energy states [37] (p. 545). The energy levels are also placed into columns to represent different spin multiplicities (e,g. singlet, doublet, triplet). Spin is a quantum property that is carried by elementary particles, which is a form of an intrinsic angular momentum. The spin is oriented in two states and is usually represented as spin up or spin down. Moreover, the transitions between these two states are perceived as a spin-flip. Figure 2.1 describes spin orientation in different energy states.

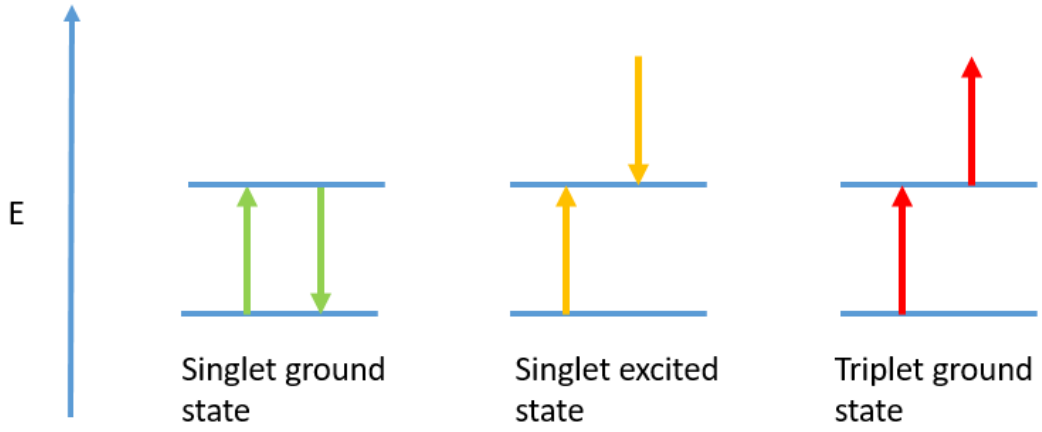


Figure 2.1: Illustration of three different energy levels. An electron in a singlet ground state or singlet excited state has all paired electron spins (following the Pauli exclusion principle). In contrast to the triplet ground state, where the electron spins are no longer paired, which means they have the same spin.

To excite a molecule or an atom, there has to be unfilled atomic of molecular orbitals that the excited electron can move into. A molecular orbital is a mathematical function that describes the behavior of electrons in a molecule in terms of the location and the wave functions. Furthermore, a molecule in the excited state will find different processes to relax back to the ground state. This process may happen through vibrational relaxation, internal conversion, or intersystem crossing (ISC). The latter will be elaborated as it is a key factor in photosensitizing. ISC is a non-radiative process requiring a transition between the two electronic states with different states of spin multiplicity. In other words, the transition requires a change of spin state. Since to change stat of spin is considered as a forbidden transition according to the selection

rules, it is a slow process. The selection rule is a model used to determine the probability of various transitions. Transitions that have a high probability of occurring are called allowed transitions. However, the ones that are less likely to occur are called forbidden transitions. The possible energy transitions of photosensitizers can be explained by the energy model as seen in Figure 2.2. In the case of porphyrin as photosensitizers, when porphyrin is excited by absorption of light, de-excitations are expected to follow three possible routes: non-radiative de-excitation, fluorescence emission, and ISC. As mentioned earlier, the latter process is crucial for the production of ROS [36] (p. 5-8, 14, 28, 36). This mechanism will be described more in detail in the next section.

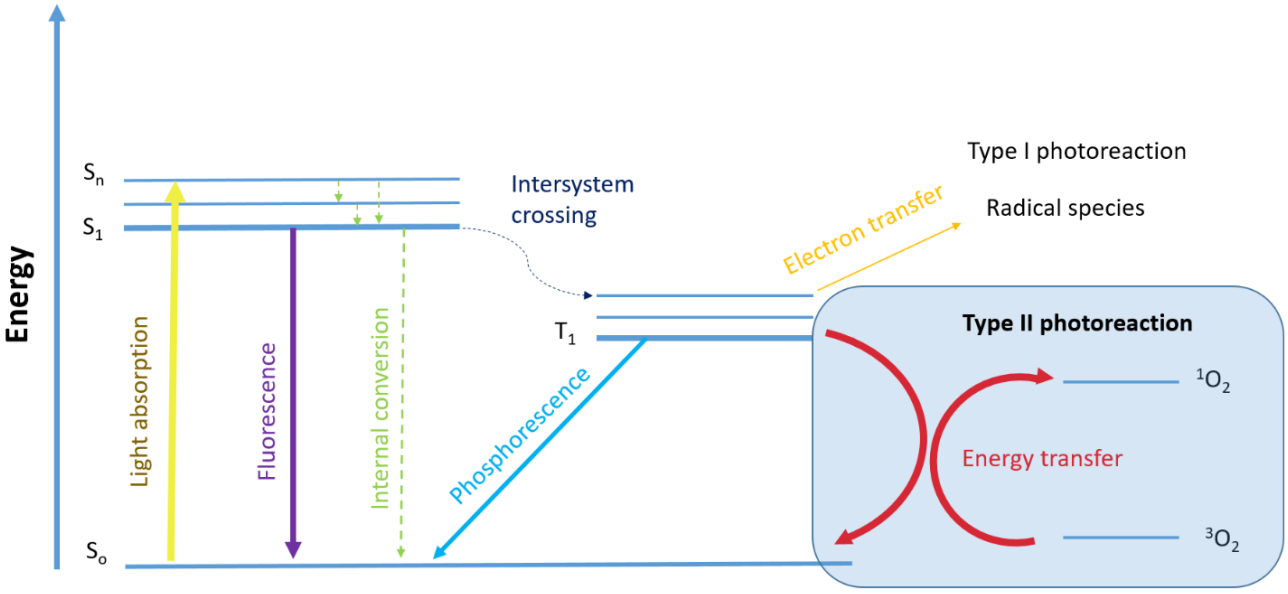


Figure 2.2: A photosensitizer that absorbs light has several possible energy transitions illustrated by a Jablonski diagram. The transitions such as fluorescence and phosphorescence emit light, while internal conversion is a non-radioactive decay process. To produce the ROS, the transition has to go through the intersystem crossing and eventually transfer energy to nearby oxygen molecules. Inspired from [79] (p. 19-20.)

Have in mind that the Jablonski diagram is an oversimplification of the transitions in molecules. It does not provide information on state crossing where the energy levels are dependent on the coordination, nor does it contain coupling with the environment. Nevertheless, the Jablonski diagram can be a useful representation, but the predicted relaxation path can be wrong.

### 2.1.3 Photosensitizing mechanisms

PDI or PDT is a minimally invasive method of killing microbial cells by irradiating a photosensitizing compound to generate highly reactive oxygen species [80]. There are two mechanisms for the generation of ROS; type I and type II (Figure 2.3). Both reactions require oxygen as a reagent. Type I produces hydroxyl radicals (•OH) and superoxide anions ($O^{2-}$) via electron transfer between excited photosensitizer and a substrate, whereas the type II mechanism produces singlet oxygen ($^1O_2$) via energy transfer from the photosensitizers to the oxygen molecule. It has been demonstrated by many authors that the latter mechanism is a simpler process and occurs more in photosensitization processes. Furthermore, it is more effective for treatments against reductions of cells. Thus, the type II mechanism will be the focus as the mechanism behind ROS production and will be explained in detail [14].

The process that induces the type II mechanism starts when a PS in its singlet ground state (GS) absorbs a photon with a specific wavelength. As a result, one of the two-electron in the GS gets excited to the higher-energy orbital. A PS in this singlet excited state is quite unstable. It will fall back to the ground state by losing energy. The loss of energy can go through thermal decay or emission of light. Alternatively, it may go through a third and important process to produce ROS, known as the intersystem crossing. Under certain circumstances (e.g. if a heavy atom is present) the spin of either electron can undergo a forbidden process and flip their spin to align themselves parallel. This means that the electron in the ground state and the electron in the excited state have the same quantum spin which deviates from the Pauli exclusion principle. Through this process, PS moves to a state of lower-energy, the excited triplet state. This state has a longer lifetime than the other singlet excited state as it is more stable due to the decay to the ground state is a “forbidden process” by the quantum selection rules. Its lifetime is on the order of microseconds. The electrons must pair their spin again before the triplet excited state can lose its energy. A longer lifetime is essential to produce ROS. There must be enough time for the excited PS to come in contact with a molecule with a lower energy triplet state. In this case, the targeted molecule is oxygen [81] (p. 122 -124). Oxygen is an interesting molecule, in fact, it is known as one of the few molecules that are stable as triplets in the ground state. Therefore, the interaction between exited triplet-state PS and oxygen in the grounds state is a favorable process [79]. Finally, at this point, the type II mechanism can take place. The interaction leads to the transfer of energy from the excited triplet state of the PS to the triplet ground state of the oxygen molecule. The result is that the triplet excited state of PS falls to the

singlet ground state and the oxygen is converted to a singlet excited state [81] (p. 122-124), [82]. This singlet oxygen is highly reactive, which is responsible for the destruction of cells in contact [80].

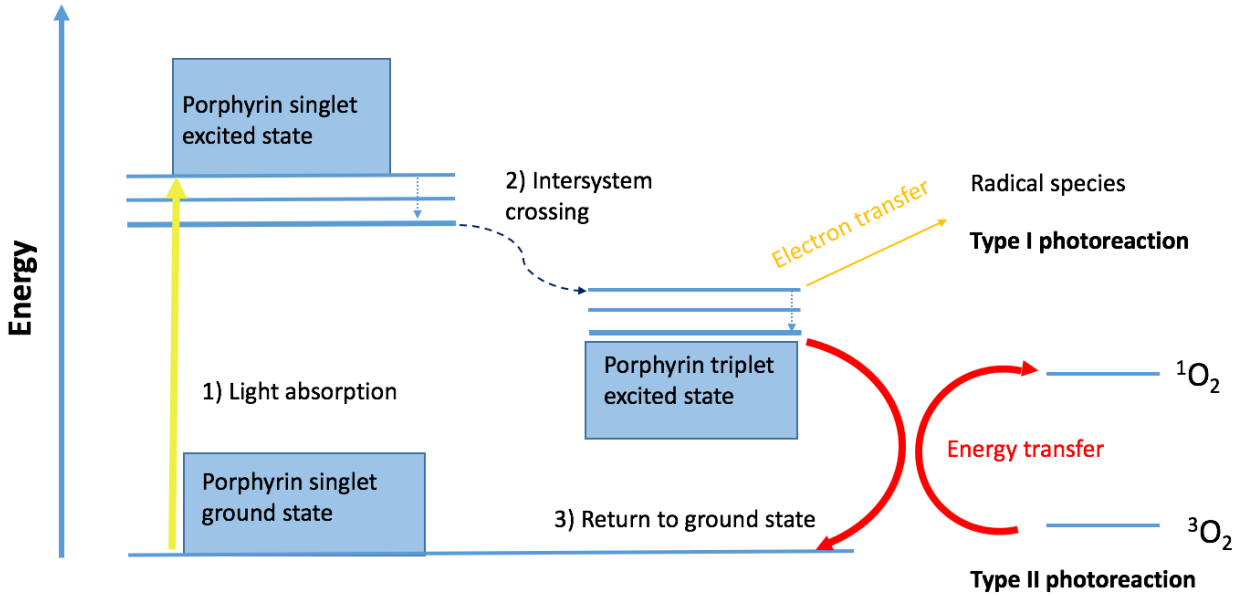


Figure 2.3: A simplified illustration of a Jablonski diagram describing the type I and type II photoreaction. 1) The light energy is absorbed by the porphyrin, which brings it to the singlet excited state. 2) The energy transition goes through intersystem crossing to achieve a triplet excited state. 3) The porphyrin returns to the ground state by transferring the energy to nearby oxygen atoms.

## 2.2 Introduction to bacteria

The following sections are going to provide a basic background in bacteria and the mechanism for fighting against microbes. Understanding how the bacteria cell is build-up gives insight into how to tear it down and inhibit bacteria-surface interactions.

Every organism is made from the basic unit for life, the cell. There are two types of cells to distinguish between, the eukaryotic and the prokaryotic [83]. The eukaryotic cell gives rise to animals, plants, fungi, and protists, while the prokaryotic cell constitutes bacteria and archaea. The prokaryotic cell has a simpler structure than the eukaryotic, Figure 2.4. These cells are missing a true nucleus and usually have a circular molecule of DNA as their only chromosome. A prokaryotic cell under an electron microscope reveals that it has a thick cell wall, where inside there is a cytoplasm. This cytoplasm consists of DNA, carbohydrates, proteins, ribosomes, etc., all mixed in a “soup”. The ribosomes are important for the synthesis of proteins.

Some bacteria have an extracellular polysaccharide layer outside the cell wall. This extra layer may enhance the bacteria's lifetime. The prokaryotic cells are reproduced by a process called binary fission, unlike eukaryotic cells that have a sexual form for reproduction. Binary fission is a form of reproduction where the cell grows to twice its size and then divide into two new cells.

The bacteria are attached to a flagellum, which has a multipurpose. The rotary motor that drives a long helical filament is the reason bacteria are motile. The flagellum may also give features such as adhesion and factors that stimulate immunity [84]. An important component of the prokaryotic cell in this setting is the cell wall. The cell wall can be crucial for designing antibacterial materials.

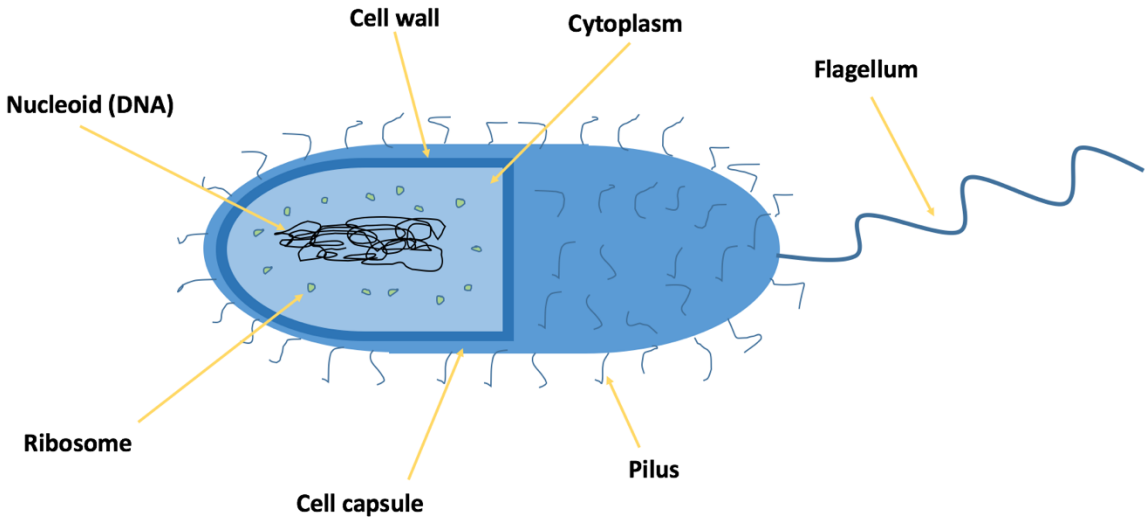


Figure 2.4: A schematic illustration of a prokaryotic cell.

### 2.2.1 Bacteria cell wall

Bacteria is protected and maintained by a cell wall composed of peptidoglycan that surrounds the cytoplasmic membrane. The peptidoglycan must be rigid due to the high intracellular turgor pressure. This pressure can reach up to 50 atm in gram-positive bacteria and 2-5 atm in gram-negative bacteria [85], [86] (p. 10). The peptidoglycan is an elastic and net-like polymer, mainly composed of polysaccharide and peptide chains.

As seen in Figure 2.5, the gram-positive bacteria and gram-negative bacteria have many of the same building blocks. However, they can be differentiated as the gram-negative bacteria has an

additional outer membrane. This addition of an outer membrane makes gram-negative bacteria a more challenging subject for PDI. The outer membrane makes it harder for hydrophobic compounds and higher molecular weight hydrophilic compounds to diffuse through the barrier. Hence, gram-negative bacteria have a lower permeability than gram-positive bacteria [87] (p. 45-46, 142), [86] (p. 133).

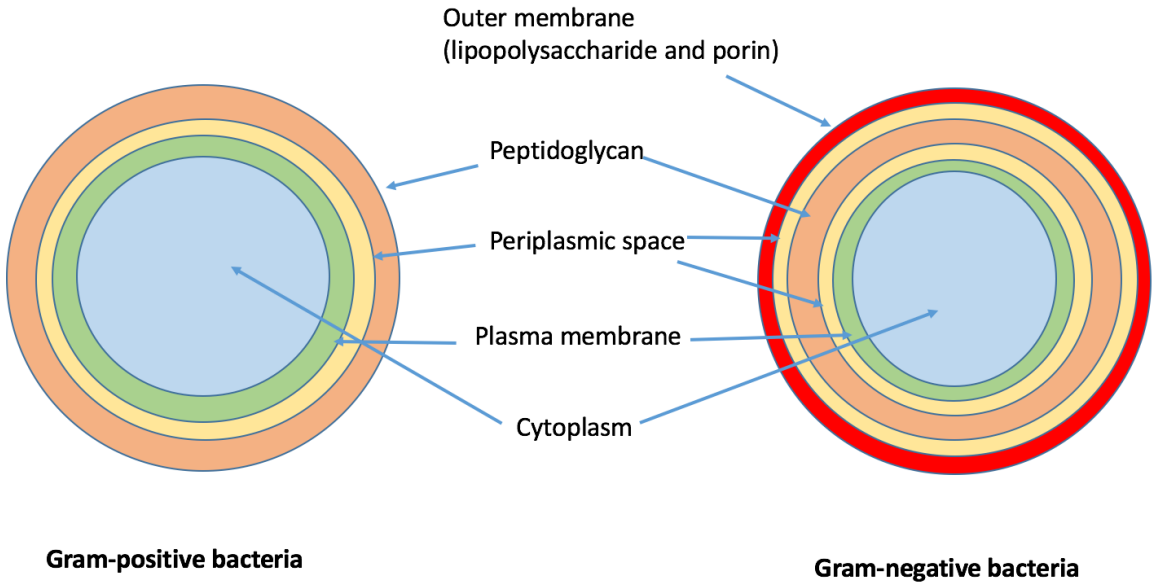


Figure 2.5: A simplified illustration of gram-positive bacteria and gram-negative bacteria cell wall. The difference of layers in gram-positive and gram-negative has an impact on the resistance against antimicrobial agents.

### 2.2.2 Biofilm

Biofilm formation begins with the adhesion of bacteria on a conditioning film as seen in Figure 2.6.i. This conditioning film can be formed by adsorption of plasma proteins when an implanted material is in contact with blood. This film minimizes the anti-properties of the biomaterial surface and aids the attachment of bacteria to the surface. Once the individual bacteria from the same or different species adhere to the surface, they multiply in population. The bacteria colonization will eventually reach a certain population density and then produces extracellular polymeric substances (EPS), Figure 2.6.ii. EPS is the building block for the biofilm matrix. The biofilm will undergo further maturing by forming channels for the intake of nutrients and removals of waste. The formation of channels also leads to clusters breaking off from the biofilm and releases to the environment, Figure 2.6.iv [6] (p. 367-381), [88] (p. 3-6).

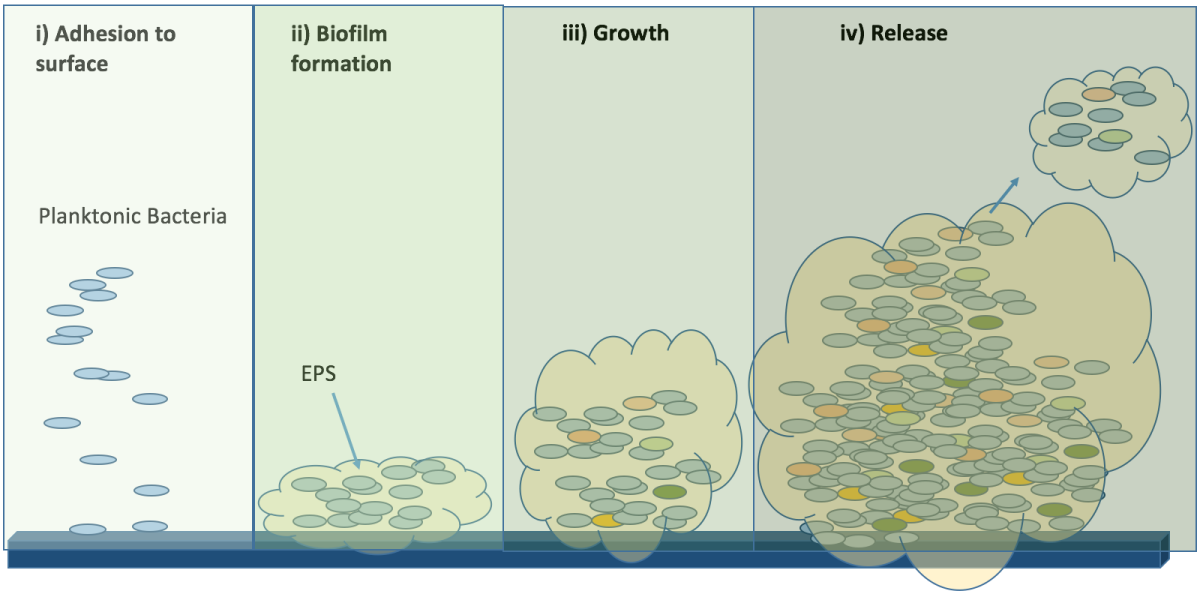


Figure 2.6: Illustration of biofilm formation on a surface. i) Initial attachment of planktonic cells on a surface. ii) Sessile bacteria secrete EPS, which increase cell aggregation and adhesion. iii) Biofilm is growing and maturing. iv) The dispersal of biofilm to the environment.

The cells in the biofilm can take different stages. The stages contribute to strengthening the biofilm community against antibiotics and disinfectants. The two main stages that the bacteria are transferring between are planktonic cells and wall-cell. A biofilm community with different "types" of bacteria strengthens the community by that some bacteria that are more resistant to the antibiotics can cover/protect other bacteria in the community [88] (p. 11-12).

Intercellular communication between the cells in the biofilm community enhances the adaptation of bacteria against the surrounding environment by gene regulation [88] (p. 11-12). The enhanced adaptability can be due to genetic exchange, such as transferring its antibacterial resistance to the next generations.

### 2.2.3 Bacterial growth

When considering bacterial growth, we are usually referring to growth within a bacteria population. This growth mainly happens through binary fission, in which a cell divides into two identical daughter cells. A cell is referred to as being viable when it can undergo binary fission. The growth of bacteria is done in a batch culture, which is a closed system. In this closed system,

the supply of nutrients for growth is limited and the temperature stays constant. This technique used to grow bacteria is divided into four phases, shown in Figure 2.7 [83].

1. **Lag phase.** In this first stage, the bacteria are adapting to the new environment, adjusting themselves to the temperature and the growth media. The binary fission does not take place, but they are building up enzymes and proteins to initiate the next phase.
2. **Exponential phase.** In this second stage, cell division is happening. The population of the bacteria is growing exponentially with a constant time interval called the generation time, $T_g$. Factors that influence the speed of growth are temperature, growth media, and genetic characteristics.
3. **Stationary phase.** The population is constant in this stage. The bacteria are still viable, but the population is not growing due to a limitation in the source for nutrients and buildup of waste material.
4. **Death phase.** The growth media is exhausted and waste production leads to inhibition of cell division and even cell death. The population of bacteria is decreasing at a uniform rate, but at a slower pace than during the exponential phase.

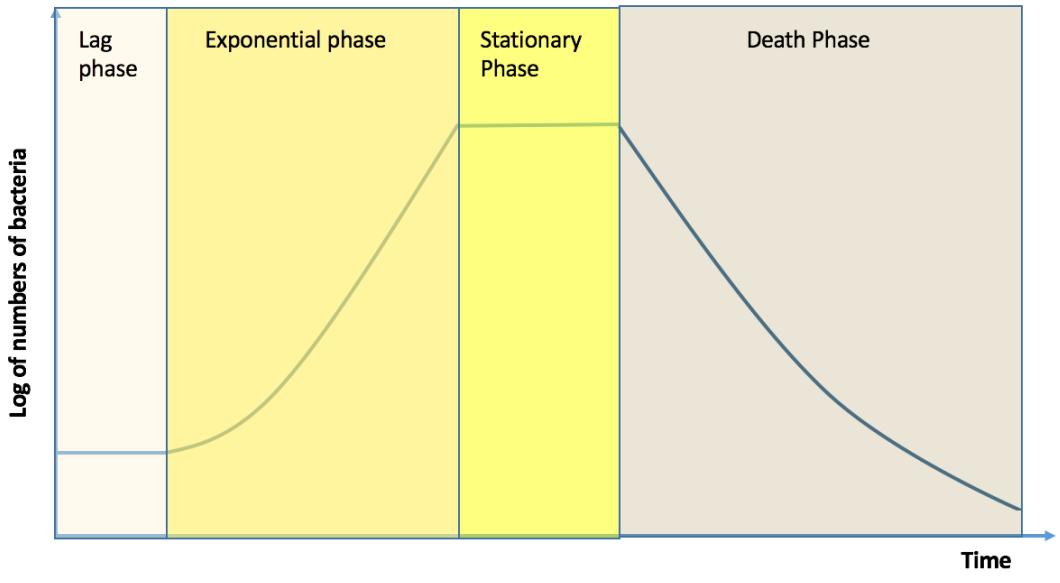


Figure 2.7: Illustration of bacterial growth in a closed system. The bacteria go through four phases: lag phase, exponential phase, stationary phase and death phase.

### 2.2.4 Bacteria in this thesis

As presented earlier, the development of treatments must be custom designed for the bacteria species, as different species have different building blocks. The gram-positive bacteria *E. faecalis* is the bacteria strain applied in this thesis for antibacterial assay. The normal habitat of *E. faecalis* is the human flora [89]. These bacteria are also known as opportunist pathogens [89], as they can induce sickness in the host when the immune defense is weakened [90]. Furthermore, *E. faecalis* are found to be related to root canal infections and post-treatment infections. *E. faecalis* can invade dentinal tubules and adhere to collagen in the dentine. Studies have shown that *E. faecalis* can form a biofilm with the presence of intra-canal medications [91]. Biofilm is a highly structured community of bacteria encapsulated in a carbohydrate matrix and it increases the survival of the bacteria, as mentioned earlier. These species have clinical relevance because they have been associated with therapy-resistant infections [91]. The biofilm of these species can even develop resistance against the strong antibiotic drug vancomycin. Hence, the prevention of biofilm formation would be a better approach because removing biofilm is proven to be difficult [92]

# 3 Methods

In this section, the methods used in this thesis are presented. First, those for growing the thin films, before presenting the methods for characterization of the products. The last part of this section will give the background for the experiments related to the antibacterial assay methods.

## 3.1 Thin films

A thin film is a layer of material with a thickness ranging from nanometers to several micrometers. It is usually applied to a substrate to introduce new properties, such as optical, electrical, and antibacterial. The techniques of deposition of thin films are primarily divided into two categories: chemical and physical techniques. In this thesis, the focus is on chemical deposition techniques. The goal is to bring the precursors into the gas or liquid phase to react with surface species on a substrate. In this chapter, chemical techniques such as spin-coating, (solution in a cell) and ALD will be described in detail.

### 3.1.1 Uniformity

Ideally, the film should cover the entire substrate in a homogenous manner. The surface wettability plays an essential role to succeed this for liquid based approaches and requires some pre-measures. Firstly, the surface must be completely clean to avoid contaminations that hinder homogenous distribution and the creation of “pinholes”. Contaminations can be avoided by cleaning the substrate with water and soap, ethanol, and compressed air for drying. Furthermore, the substrate can be enhanced for thin film deposition by plasma cleaning.

### 3.1.2 Plasma cleaner

Plasma cleaning is a process of removing impurities and contaminants from the surface while introducing polar functional groups (Figure 3.1). The instrument comprises a chamber where the pressure is controlled. The gas or gas mixture present in the chamber is brought to a higher energy state and ionized to form a plasma by the application of an electromagnetic field. Hence, a substrate placed inside the plasma chamber will be bombarded with energetic plasma or dielectric barrier discharge (DBD) plasma. Usually, a mix of gasses such as oxygen and argon

is used in a plasma cleaner. The active species from the plasma break down contaminations on the surface and are removed away by the vacuum system. Meanwhile, radicals bind to the active surface sites all over the substrate. The surface after plasma cleaning will have an increased surface wetting, which increases the adhesion of precursors. One of the distinct advantages of this method is that it is not limited by surface geometries, and easy to operate. The substrate after treatment with plasma cleaning is generally ready to be used in manufacturing.

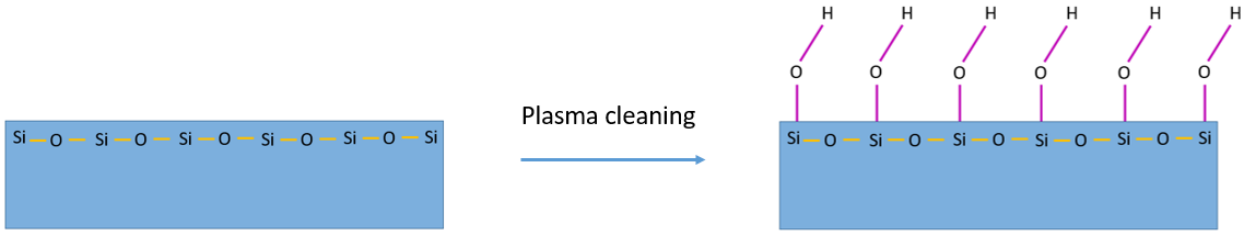


Figure 3.1: Plasma treated silica surface. Hydroxyl groups are attached to the substrate.

### 3.1.3 Spin coating

Spin coating is a method for creating uniform thin films by liquid deposition. A substrate is adhered at the center of the spin-coating machine by vacuum. The instrument used in this work can rotate the substrate up to 8000 rpm. The deposited liquid or sol-gel is dispersed on the substrate by the centrifugal force as presented in Figure 3.2. An increase in spinning speed decreases film thickness. The thickness is also controlled by the concentration and viscosity of the liquid. The liquid used for deposition comprises the desired building blocks dissolved in a solvent that is volatile and easily evaporates. Creating a thin film starts with the deposition of a small amount of the liquid on the substrate by a micropipette (typically 20-40 µl for a 20x20 $mm^2$ glass substrate). The spinning spreads the liquid over the substrate, and excess precursors are ejected off the edge of the substrate. Furthermore, the solvent evaporates leaving the desired molecules distributed homogenously on the substrate (Figure 3.2). Ethanol is commonly used as a solvent due to its high volatility. This method can be used to design thin film in a layer by layer manner using liquids with different kinds of molecules. The advantage of this method is that it is simple, easy to operate, and fast. The challenge with this method is to overcome the "coffee stain effect" that leaves the film less homogenous at the edges. This effect is explained by the fluid flowing outwards and forms more thickness at the edges.


Figure 3.2: A schematic illustration of spin coating. Precursors are deposited on the thin film. The substrate spins and the precursors get distributed evenly by the centrifugal force. The result is a layer of thin film on the substrate.

### 3.1.4 Atomic layer deposition (ALD)

ALD is a method for creating thin films from the vapor phase with an excellent atomic-level control in a heated reaction chamber. This method is based on growing thin films on a substrate by exposing the substrate to alternating pulsate of precursors in the vapor phase, followed by purging of inert gas to remove unreacted precursors. The vapor precursors attach to the active sites on the substrate until it is fully saturated. Once all active sites are depleted, the process stops due to lack of reactive sites, which gives rise to its self-limiting growth mechanism. Hence, it is possible to achieve a monolayer of the precursor. This method is not geometry limited due to the gas phase approach. The ALD cycle is illustrated in Figure 3.3.

The growth of thin film on a substrate is temperature-dependent. The ideal range of temperature that provides controlled growth is called the ALD window. If the temperature is too high, decomposition and desorption can occur. While too low temperature leads to incomplete reaction or condensation of precursors.

The properties of the precursors are the main limitations of this method. The precursors should have good volatility and stability in high temperature and favor sublimation over decomposition at the reaction site. Furthermore, the by-products from the reaction should not compete with the precursors over the reaction sites available. In addition, ideal precursors should also be non-toxic, inexpensive, and incombustible [93] (p. 10-18).

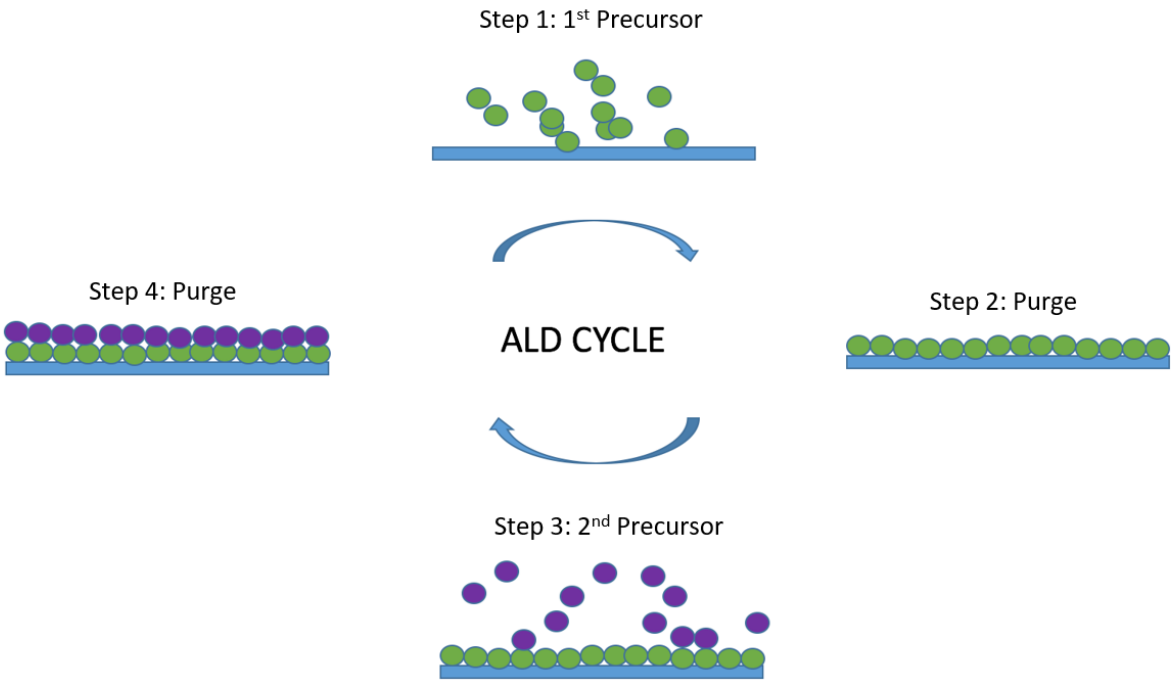


Figure 3.3: A schematic representation of atomic layer deposition cycle. (Step 1) The first precursor in gas phase is introduced into the chamber with the substrate. The precursor attach on the active sites and creates a monolayer. (Step 2) Followed by a purging step with $N_2$ to remove unreacted and excess precursors. (Step 3) Introducing of the second precursor into the chamber to react with the first layer. (Step 4) Another step of purging.

### 3.1.5 Liquid atomic layer deposition (LALD)

Liquid atomic layer deposition (LALD) can be considered as a growth method that can overcome some of the current constraints of ALD. This method is usually much simpler and more versatile, and is also based on a layer-by-layer composition. The advantage of this method is that instead of requiring gaseous-precursors as for ALD, this method uses precursors dissolved in a liquid phase. The building of layer-by-layer also follows the principle of self-limiting growth. Here, different precursors are introduced to a substrate and react with surface species. As the first layer is built, it is followed by a purge step, usually based on a solvent. Thereafter, the next solution is pulsed in to create the next layers and followed by a purging step. That concludes the first cycles, and the thickness can be controlled by the number of cycles. This method gives high precision thickness control, excellent conformality, and the possibility of being automated simply and inexpensive. It can also be performed with a broader diversity of well-known cheap reagents already used in solution chemistry. Note that this

technique is still in development and is summarized in the review article [94]. A more detailed method description of an approach to the LALD will be given in the experimental section.

## 3.2 Characterization techniques

A short introduction of the various characterization techniques: UV-Vis spectroscopy, X-ray powder diffraction (XRD), Fourier-transform infrared spectroscopy (FTIR), scanning electron microscopy (SEM) in combination with energy-dispersive spectroscopy (EDS), atomic force microscopy (AFM), spectroscopic ellipsometry (SE), and contact angle measurements are given in the appendix section A as these are relatively standardized methods used in the group.

## 3.3 Antibacterial assay methods

In this section, the experimental methods used during the antibacterial assays will be explained. Note that the specific experiments in this project are described in more detail in the experimental section.

### 3.3.1 Performing an antibacterial assessment

The antibacterial activity of a material is commonly evaluated with an inoculum concentration around $10^5$-$10^7$ $CFUmL^{-1}$ bacteria. To set this in perspective, infected tissue typically have a microbial concentration around $10^8$-$10^{10}$ $CFUg^{-1}$ [95]. After exposing the active material to prepared inoculum, the bacteria suspension in collected and serially diluted. The serial dilution is illustrated in Figure 3.4, where the bacteria suspension is diluted into several tubes to achieve a different concentration of bacteria. Thereafter, the bacteria in each tube are plated in an agar plate. The term plating refers to the act of transferring the diluted bacterial suspensions onto agar plates. Agar plate is a Petri dish that consists of solidified agar which is a growth medium, that can be applied to culture microorganisms.

The bacterial suspension is commonly dispensed in two ways: drop-wise or spiral pattern. The latter method requires a spiral plater to conduct this plating technique. The next step after plating is to incubate the agar plate overnight under suitable conditions (37 °C, 5% $CO_2$) to allow the bacteria to grow and form CFU. Each CFU represents a single bacteria cell that multiplies into millions of cells piled up onto each other until we can see a single colony of

bacteria cells. An important factor is to avoid overgrowth of bacterial colonies to avoid saturation and allow for accurate counting. The agar plate that shows a countable number of CFU (30-300) will be used to calculate the number of bacteria.

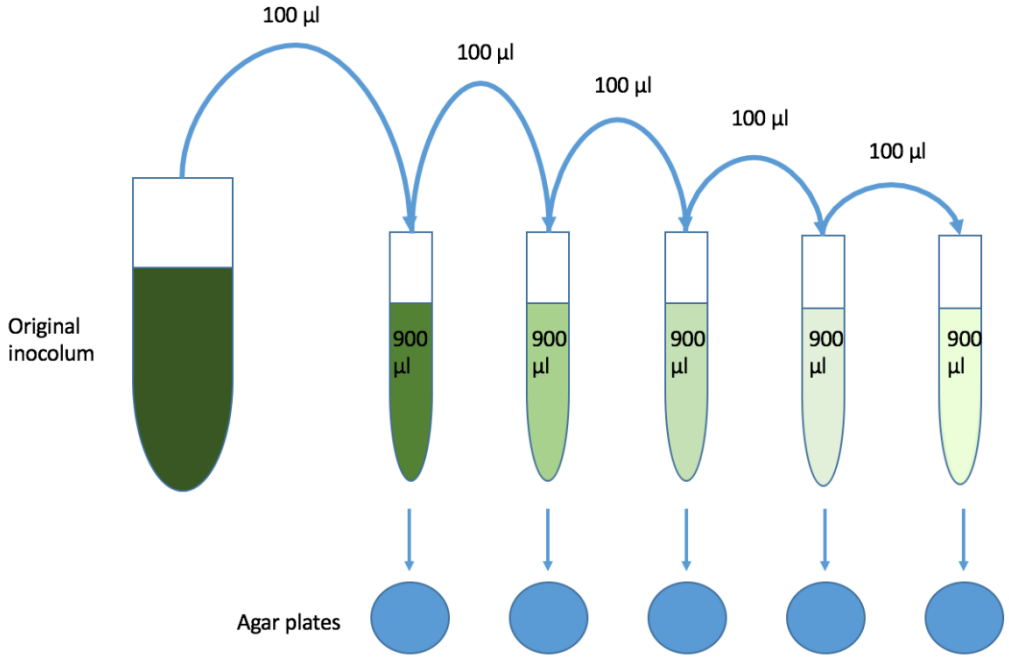


Figure 3.4: Illustration of serial dilution. An original inoculum with unknown concentration is following serial dilutions. The diluted concentrations are placed on an agar plate for counting the number of colonies cultured.

The antibacterial properties of material are determined by comparison of CFU calculation of the active sample to the control sample. The antimicrobial effect is determined by the logarithmic reduction, and this is calculated by subtracting the log(CFU) in the sample from the log(CFU) in the control:

$$\text{Log reduction} = \log(\text{CFU})_{\text{control}} - \log(\text{CFU})_{\text{sample}}$$

A log of reduction of at least 3 is considered to having an antimicrobial effect, while a log reduction of below 0.5 is considered to have no antibacterial activity [96].

Another way of representing the antibacterial effects can be through the percentage reduction by comparing the number of bacteria ($CFUmL^{-1}$) on the control to the number of bacteria on the sample.

Decreased in viable bacteria = viable bacteria in control – viable bacteria in sample

$$\%\ decrease = \frac{decrease\ in\ viable\ bacteria}{viable\ bacteria\ in\ control} * 100$$

### 3.3.2 Confocal laser scanning microscope (CLSM)

Confocal laser scanning microscope (CLSM) offers several advantages over traditional fluorescent microscope such as the possibility to take a set of images at different levels of depth and reconstruct it into 3D images of the targeted sample. Furthermore, it allows to eliminate or reduce the background information away from the focal plane. In a confocal instrument, the coherent light emitted by the excitation source passes through a pinhole aperture that is situated in a conjugate plane (confocal) with a scanning point on the sample and a second pinhole aperture positioned in front of the detector. This allows to focus light to a spot and scans it across the sample to build an image, whereas in the traditional fluorescence microscope the entire specimen is excited at once. CLMS is an ideal tool for imaging biofilms on material surfaces and enables the investigation of the spatial organization of bacteria within a created biofilm. In this study, we used confocal laser scanning microscope (CLSM) system FV1200 from Olympus equipped with a 60x water immersion objective with a working distance of 2 mm.

# 4 Experimental

This chapter provides the chemicals and materials that were used in this thesis, as well as the procedure to make the thin films and their characterization. Finally, the experimental part of the antibacterial assay will be explained.

## 4.1 Reagents and solvents

The origin of the reagents and solvents used in this thesis is shown in Table 4.1, including the supplier, batch number, and chemical formula. Zirconium tetrachloride ($ZrCl_4$) was been kept in a glove box, while other chemicals were kept in a standard chemical cabinet.

**Table 4.1: Overview of all chemical used in the first part of the experiment.**

| Chemical | Abbreviation | Linear formula | Purity | Molecular weight (g/mol) | LOT number | CAS number | Supplier |
|---|---|---|---|---|---|---|---|
| 4,4',4'',4'''-(porphine-5,10,15,20-tetryl)tetrakis(benzoic acid) | TCPP | $C_{48}H_{30}N_4O_8$ | 98% | 790.77 | 117ESi19 | 14609-54-2 | PorphyChem |
| Zirconium(IV) chloride | - | $ZrCl_4$ | 99.95+%-Zr | 233.03 | 27478100 | 10026-11-6 | Strem Chemicals, Inc. |
| Zirconium(IV) oxychloride octahydrate | - | $ZrOCl_2*8H_2O$ | 99% | 286.22 | - | 13520-92-8 | Fluka |
| Distilled water | DI water | $H_2O$ | Type-2 | 18 | - | - | Distilled at UiO |
| Ammonia solution 28% | - | $NH_3$ | - | - | - | 1336-21-6 | VWR |
| Ethanol absolute | EtOH | $C_2H_5OH$ | ≥99.8% | - | 19A164011 | 64-17-5 | VWR |
| Hydrochlorid acid fuming 37% | - | HCl | - | - | - | 7647-01-0 | Merck |

| | | | | | | | |
|---|---|---|---|---|---|---|---|
| 0.9% saline solution | | 0.9% NaCl | - | - | - | - | Produced at UiO |
| Sodium Chloride | - | NaCl | 99.5% | 58.44 | K27736133 | 7647-14-5 | BDH Chemicals |
| Potassium bromide | - | KBr | ≥99% trace metals basis | 119 | BCCC7830 | 7758-02-3 | Sigma-Aldrich |

### 4.1.1 Preparation of precursors

The various solutions used in this work were made when needed. The main solutions that were used the most will be presented in this section (Table 4.2). Two different solutions were prepared. The first solution was prepared by dissolving TCPP (0.066 mg) in ethanol (40 ml) with the aid of stirring by a magnet bar. The second solution was prepared by dissolving $ZrOCl_2*8H_2O$ (1.5 mg) in 40 ml ethanol with the aid of stirring by a magnet bar. The solutions were stored in a light-blocking amber flasks and stirred on a magnetic stirrer for 3 days at room temperature (37 °C). The TCPP solution was evaluated by UV-Vis absorption to confirm that the TCPP powder is completely dissolved in ethanol after the third day (not shown in this thesis).

**Table 4.2: Overview of precursors used in this work to deposit ZrTCPP films by spin coating.**

| Chemical | Amount | Concentration (M) |
|---|---|---|
| EtOH | 40 ml | - |
| TCPP | 0.066 g | $2.09*10^{-3}$ |
| Zr | 1.50 g | $1.31*10^{-1}$ |

## 4.2 Substrates

Thin films were deposited on microscope cover glasses $SiO_2$ (ø = 20 mm, VWR). In addition, the silicon substrates Si(100) 2x2 $cm^2$ were used for ellipsometry measurements and electropolished steel substrates were used for FTIR measurements.

**Table 4.3 Overview of substrates.**

| Substrate | Size | Supplier |
|---|---|---|
| Glass ($SiO_2$) | 20 mm | VWR |

| | | |
|---|---|---|
| Silicon wafer | 2 x 2 $cm^2$ | Siliconwafers.com, univeristywafers.com |
| Electropolished steel substrates | 2 x 2 $cm^2$ | Astrup |

### 4.2.1 Substrate pre-treatment

The glass substrates were cleaned using TechniCloth TX606 wipers (Texwipe) soaked in distilled water and soap. Thereafter, the soap was washed away with distilled water, followed by rinsing with ethanol. At last, the substrates were dried by compressed air. The silicon substrates were wiped with wipers soaked in ethanol, followed by compressed air drying. The electropolished steel substrate did not need any additional cleaning after peeling off the outer layer of protective polymer.

### 4.2.2 Plasma cleaner:

The substrates were further treated with a plasma cleaner at 0.7 Torr (Harric Plasma) using air as process gas. The substrates were treated with plasma for 5-10 minutes.

### 4.2.3 Sample handling

The substrates and the films were stored on a glass plate in a plastic CD covers in order to decrease contaminations. The solutions of Zr and TCPP were stored in amber glass bottles to block UV- and blue light.

## 4.3 Spin coating

A WS-400-6NPP spin coater (Laurell Technologies) was used to deposit films by the spin-coating method. A range of parameters was varied and tested for the depositions to identify the conditions for the formation of homogeneous films. The parameters varied were rotational speed of the spin coater, time, deposited droplet size, concentration of the precursor solutions, and the number of deposited layers.

In this thesis, several approaches were performed on the spin coater. The standard protocol that were mostly used is shown in Figure 4.1.

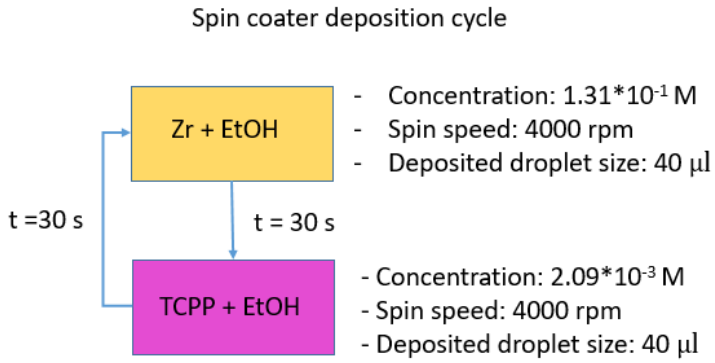


Figure 4.1: The standard protocol for a one deposition cycle of ZrTCPP film in a spin coater.

## 4.4 ALD

The glass substrates were coated with a thin layer of $ZrO_2$ of by ALD to enhance adhesion. The glass substrate after pre-treated described in section 4.2.2 was introduced into a reaction chamber. This chamber is then introduced into an ASM Microchemistry Ltd F-120-type hot-wall- reactor using $ZrCl_4$ and water as precursors. We followed the procedure described by Olsen [97].

## 4.5 Layer-by-layer liquid deposition

This procedure was inspired by the layer-by-layer liquid deposition described in section 3.1.5. The instrument was set up by Ola Nilsen and Per-Anders Stensby Hansen, as shown in Figure 4.2. The closed reaction chamber is fabricated as described in section 4.5.1. The procedure is conducted at room temperature both with light and in darkroom. The interior of the chamber is composed of four tubes. Three for the different chemicals and one for waste. The 20 ml syringes were connected to home-made syringe pumps to control the pumping of solutions. The pumps were controlled by a separate controller. Figure 4.3 demonstrates the principle of LbL liquid deposition cycle. The reaction cell was connected to a UV-Vis absorption spectrometer (OceanOptics USB2000+) and the data were recorded by OceanView. The cell was evaluated under the light microscope after the procedure.

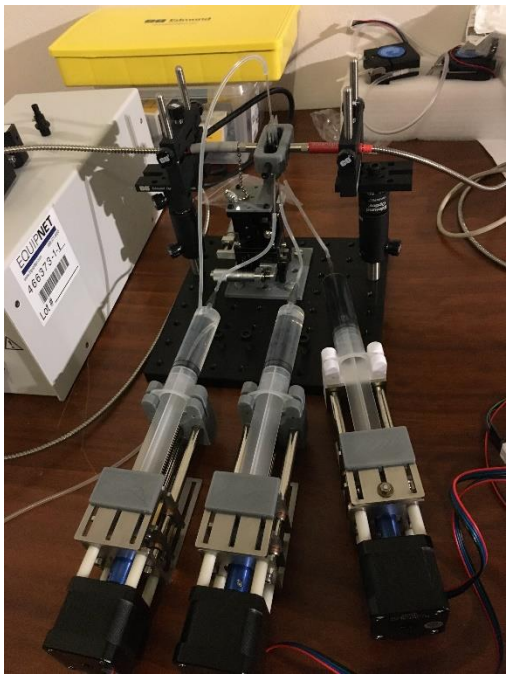

Figure 4.2: The setup of Layer-by-Layer liquid deposition.

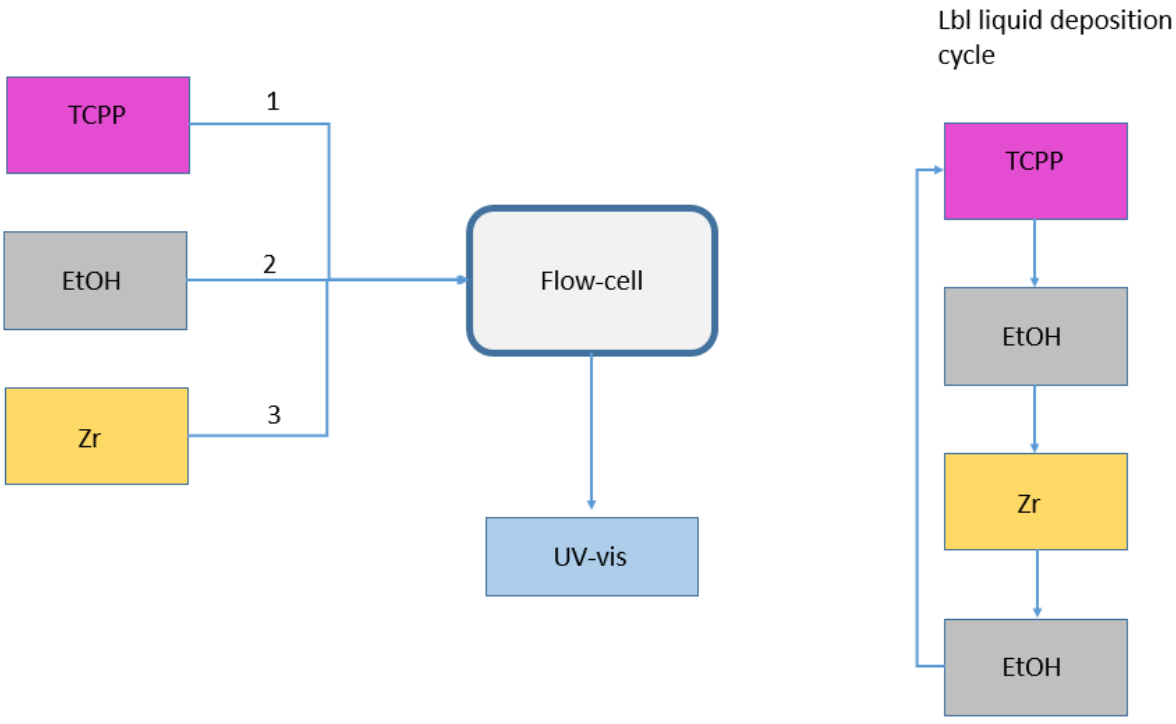


Figure 4.3: A schematic illustration of the LbL liquid deposition and the cycle of deposition.

### 4.5.1 Fabrication of flow-cell

The frame of the framework was made of PLA by 3D-printing, by Ola Nilsen. The cell walls consisted of glass slides (25 x 50 $mm^2$) that were pre-treated as glass substrates described in

section 4.2.1, followed by plasma cleansing (section 4.2.2) or covered with a layer of $ZrO_2$ by ALD (section 4.4). The adhesive material used to glue the cell together was superglue and silicone. The cell was dried at room temperature for 3 days before use.

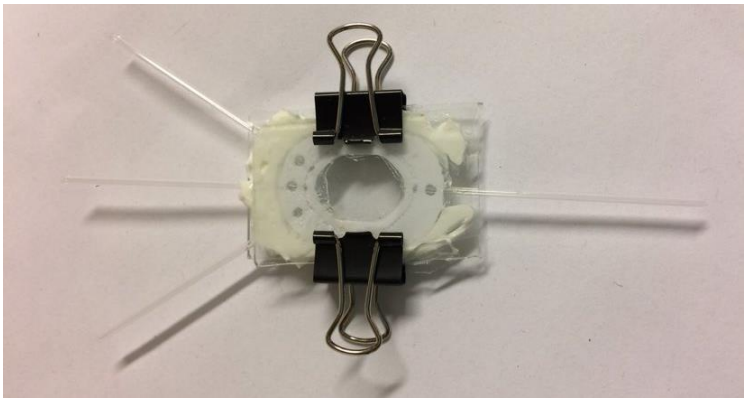

Figure 4.4: An image of the flow-cell used in layer-by-layer liquid deposition.

**Table 4.4: Materials used to build flow-cell**

| Material | Size | Supplier |
|---|---|---|
| Premiere glass slides | 25 x 50 $mm^2$, 1.0 mm | Premiere |
| Capillary tubes | 1.3-1.5x100 mm | Vitrex |
| Sanitary silicone | - | Casco |
| Silicone | - | Pattex |
| 3D PLA printed frame | - | Clas Ohlson |
| Blinder clips | 15 mm | Deli |
| Soft-ject syringes | 20 ml | Henkesasswolf |
| Silicone tubes | 1 x 3 mm | "Sentrallageret" |

## 4.6 Characterization techniques

### 4.6.1 UV-Vis spectroscopy

A Shimadzu UV-3600 UV-Vis-NIR spectrophotometer was used for measuring the transmittance of thin films and absorption of solutions in the range 250 – 900 nm. The spectrophotometer is equipped with a 50 W halogen and deuterium lamp as a light source. The detectors used in the instrument were a photomultiplier tube (PMT) (180-900 nm) and InGaAs photodiode (900-1700 nm). The software used was UVProbe.

### 4.6.2 UV-Vis used in LbL deposition

The instrument used for UV-Vis absorption measurement was USB2000+ spectrometer controlled by the OceanView software. All from OceanOptics.

### 4.6.3 Ellipsometry

Measuring thickness and the refractive index was performed on a J.A. Woollam alpha-SE spectroscopic ellipsometry. The wavelengths used for measurement were from 250 nm to 900 nm with incident angle of 70°. The software used to fit the data was CompleteEASE.

### 4.6.4 Contact angle

The contact angle of the thin films was measured on a Theta Lite (Biolin Scintific) contact angle meter. The software used to collect the data was OneAttension.

### 4.6.5 FTIR

Fourier transform infrared spectroscopy (FTIR) measurements of the films were performed using Bruker Vertex 70 spectrometer equipped with Pike VeeMAX III specular reflection accessory with an angle of incidence at 75°. All data were acquired in the reflection mode using 64 scans in the wavenumber range of 4000 - 370 $cm^{-1}$ and 2 $cm^{-1}$ resolution. Films for FTIR measurements were deposited on electropolished steel substrates. FTIR measurement of the pure organic compound was performed using the same instrument in the transmission mode. The potassium bromide (KBr) pellet for the measurement was prepared using a laboratory hand press.

### 4.6.6 AFM

Atomic force microscopy (AFM) measurements for 5 layers ZrTCPP films were performed in noncontact mode using Park XE70 instrument from Park Systems. The RMS roughness was

calculated as an average value from three cross-section line profiles picked in three different regions on a scanned sample. The AFM images were processed using Gwyddion 2.56 software.

### 4.6.7 XRD

A Bruker AXS D8 Advance diffractometer with LynxEye strip detector in standard Bragg-Brentano configuration was used as the XRD instrument for the characterization of thin films. A Ge (111) focus monochromator was used to select single wavelength Cu Kα1 ($\lambda = 1.5406$ Å) radiation. The data analysis was performed using the software DiffracEva from Bruker, and Origin 9.1. The thin films were mounted in a well-type sample holder

### 4.6.8 SEM and EDS

The scanning electron microscopy (SEM) was performed by a Hitatchi TM3000 Tabletop Microscope. This system is incorporated with the EDS system Quantax 70 from Bruker. EDS measurements were made with an acceleration voltage of 15 kV and 3000x magnification.

## 4.7 Materials and methods

In this section, the experimental work performed at NIOM is described. The practical work was originally planned to be performed by Martin Tran under supervision of Melania Rogowska. However, due to Covid-19 regulations, Martin Tran was not admitted to the building to obtain training and the practical work was therefore performed fully by Melania Rogowska with communication with Martin Tran. The ZrTCPP films fabricated in the experimental part above will be evaluated against *E. faecalis*.

### 4.7.1 Bacteria

Stock cultures of *Enterococcus faecalis* OGRF1 (ATCC 47077) were stored at -80 °C in brain heart infusion (BHI) supplemented with 30% glycerol. The fresh cultures were prepared by growing *E. faecalis* overnight (ON) for 18 hours in tryptone soya broth (TSB) in incubator (Panasonic MCO-19M multi gas incubator) at 37 °C and 100% humidity under normal atmospheric conditions supplemented with 5% $CO_2$. For ON culture preparation, the sterile

inoculating loop was dipped in the stock cultures and transferred into the 10 ml TSB. The ON cultures were centrifuged at 5000 G (6682 rpm) for 5 minutes and resuspended in 0.9% (w/v) saline solution (Milli-Q) to an optical density at 600 nm ($OD_{600}$) of around 1.0 using a spectrophotometer (Thermo Scientific Spectronic 200E spectrometer). $OD_{600}$ of 1.0 corresponds to about $10^8$ $CFUml^{-1}$ (CFU = colony forming units). The bacteria suspension was then diluted 1:10 in 0.9% (w/v) saline solution to achieve a desired bacteria concentration of approximately $10^7$ $CFUml^{-1}$. Green fluorescent protein (GFP) expressing *E. faecalis* OG1RF:pMV158 was used to control the adhesion of bacteria to the surfaces with fluorescence microscopy (488 nm, Olympus). Stock cultures were stored at -80 °C in BHI and the ON cultures were prepared as described above.

### 4.7.2 Materials

The antibacterial properties of the materials were studied with 5 layers ZrTCPP films deposited on microscope cover glasses (*ø* = 20 mm, VWR) and uncoated cover glass substrates as controls. The glass substrates were precleaned with soap and water, ethanol and plasma cleaner. In all experiments the samples were placed into sterile 12-well culture plates (clear polystyrene, flat bottom plates, Corning® Costar®, Kennebunk, ME, USA). All chemicals used during the antibacterial assays are given in Table 4.5. BHI medium was prepared by mixing 37.04 g BHI with 1 L $H_2O$, whereas TSB medium by mixing 30.12 g with 1 L $H_2O$, following by autoclaving at 121 °C for 30 minutes. The BHI agar plates were prepared by mixing 22.22 g BHI with 9.14 g agar powder in 600 ml $H_2O$. The medium was autoclaved at 121 °C for 30 min and cooled to about 60 °C. The BHI agar liquid was dispensed into the plastic sterile Petri dishes, allowed to dry and stored in a fridge.

**Table 4.5 Chemicals used in the antibacterial assays.**

| Chemical | Abbreviation | Supplier |
|---|---|---|
| Milli-Q® water | $H_2O$ | Merck Millipore |
| 0.9% saline solution | 0.9% NaCl | Prepared at NIOM |
| Phosphate buffered saline | PBS | Lonza, BioWhittaker™ |
| Brain heart infusion CM1135 | BHI | Oxoid, Thermo Scientific™ |
| Tryptone soya broth CM0129 | TSB | Oxoid, Thermo Scientific™ |
| Agar bacteriological LP0011 | Agar | Oxoid, Thermo Scientific™ |
| Propidium iodide | PI | *Bac*Light™, Thermo Scientific™ |
| SYTO™ 9 | SYTO 9 | *Bac*Light™, Thermo Scientific™ |

Figure 4.5 Preparation of BHI agar culture plates.

### 4.7.3 Light source

The irradiation source used in the bacteria inactivation experiments was a single irradiation chamber (Polylux PT, Dreve, Unna, Germany) equipped with three compact blue light tubes (Osram 9W/71) emitting in the wavelength range 400-520 nm, with the maximum emission at around 450 nm (Figure 4.6). The average irradiance of the light tubes was 19 $mWcm^{-2}$ (±5%). The emission and absorption spectra of the irradiation source and the ZrTCPP film mainly overlap in the region 400-490 nm (Figure 4.7). The measured stability of the lamp irradiance (19 $mWcm^{-2}$) was achieved after 20 min. The light dose ($Jcm^{-2}$) can be calculated as follows:

$$\frac{\mathrm{mWcm^{-2}}}{1000} * \mathrm{time\ (s)} = \mathrm{Jcm^{-2}}$$

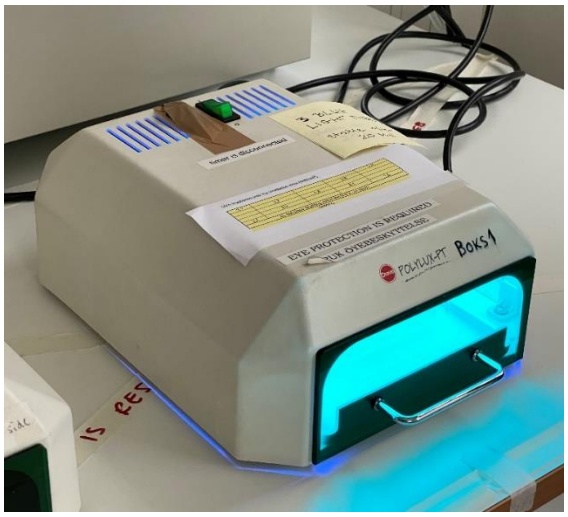


Figure 4.6 Light box used in the bacteria inactivation experiments.

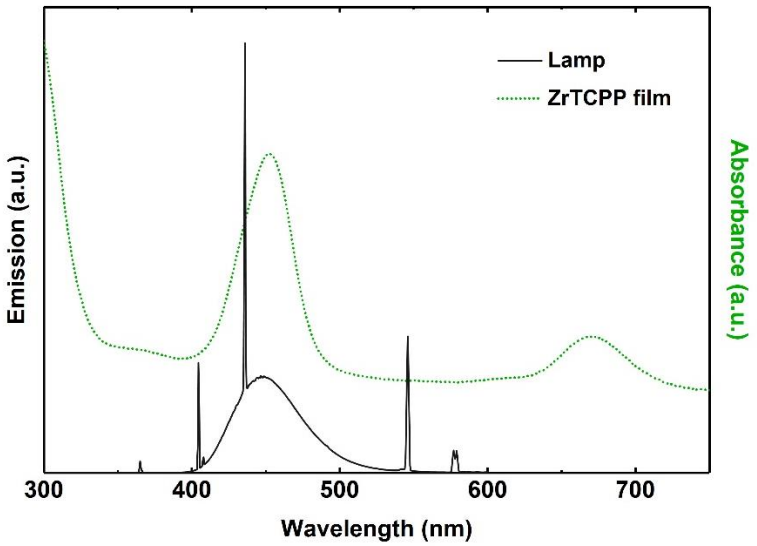


Figure 4.7 Emission spectrum of the irradiation source used in the bacteria inactivation experiments and absorption spectrum of the ZrTCPP film. Optical characterization of the lamp system was performed by the Norwegian Radiation and Nuclear Safety Authority.

### 4.7.4 Antibacterial phototoxicity on planktonic bacteria

The phototoxic effect of combined exposure of ZrTCPP films and blue light irradiation was evaluated against planktonic cultures of *E. faecalis*. The irradiation dose tested was 22.8 J/cm$^2$, 11.4 J/cm$^2$ and 5.7 J/cm$^2$, corresponding to 20, 10 and 5 min of irradiation.

### 4.7.5 Adhesion of bacteria

To determine the adhesion of bacteria on the ZrTCPP films and to confirm that all attached bacteria are removed from the surfaces using vortex method, the control experiment was performed using fluorescence microscopy. The overnight cultures of fluorescent *E. faecalis* OG1RF:pMV158 were centrifuged at 5000 G for 5 minutes and resuspended in 0.9% NaCl to $OD_{600}$ = 1.00 corresponded to 4.88 x $10^8$ $CFUml^{-1}$. The bacteria suspension was then diluted 1:10 in 0.9% NaCl to achieve a desired bacteria concentration of 4.72 x $10^7$ $CFUml^{-1}$. Six ZrTCPP films were placed into 12-well plate and exposed to 1 ml of prepared bacteria suspension followed by 90 min incubation (37 °C, 100% humidity and 5% $CO_2$). After incubation, three films were removed from the wells and transferred to 50 ml Falcon tubes containing 10 ml glass beads 3 mm in diameter (Merck) and 5 ml of 0.9% NaCl and vortexed for 30 s. The other three ZrTCPP films were washed in 0.9% NaCl by dipping the surfaces in saline solution using tweezers. All surfaces were placed on the glass microscope slides using double-sided tape and analysed with fluorescence microscopy using 100x oil immersion objective (488 nm).

### 4.7.6 Phototoxicity of ZrTCPP films

The ON cultures of *E. faecalis* were centrifuged at 5000 G for 5 minutes and resuspended in 0.9% NaCl to $OD_{600}$ = 1.02 corresponded to about 5.8 x $10^8$ $CFUml^{-1}$. The bacteria suspension was then diluted 1:10 in 0.9% NaCl to achieve a desired bacteria concentration of about 5.6 x $10^7$ $CFUml^{-1}$. ZrTCPP films and controls were placed in two 12-well plates and exposed to 1 ml of prepared bacteria suspension followed by 90 min incubation (37 °C, 100% humidity and 5% $CO_2$). During all procedure the samples were protected from light using Al foil. One of the 12-well plate with half of the samples was placed in the irradiation chamber and irradiated with blue light. The irradiation dose tested was 22.8 $J/cm^2$, 11.4 $J/cm^2$ and 5.7 $J/cm^2$, corresponding to 20, 10 and 5 min of irradiation. The light box was turned on 20 min before treatment to assure the radiation stability. After irradiation, the samples were placed back in the incubator for 30 min to allow the reactions to continue in the dark. The films were removed from the wells and transferred to 50 ml Falcon tubes containing 10 ml glass beads 3 mm in diameter and 5 ml of 0.9% NaCl and vortexed for 30 s. The suspension was serial diluted in PBS and plated onto BHI agar plates (25 µl). The supernatant from the wells was also serial diluted and plated onto BHI agar plates. After approximately 24 h incubation (37 °C, 100% humidity and 5% $CO_2$) the colonies were counted (30-300 colonies) and $CFUml^{-1}$ was calculated. Experiments were performed in nine replicates (n = 9) for light dose 22.8 $J/cm^2$ and 11.4 $J/cm^2$, whereas for the

light dose 5.7 J/cm$^2$ only in three replicates (n = 3). To verify the inoculum concentration, the $OD_{600}$ and the diluted 1:10 bacteria suspension were plated onto BHI agar plates during each experiment (Table 4.6).

**Table 4.6 Real concentrations of *E. faecalis* used in the experiments for different light doses**

| Experiment | $OD_{600}$ = 1.02 (CFUml$^{-1}$) | 1:10 (CFUml$^{-1}$) |
|---|---|---|
| 1 / 22.8 J/cm$^2$ | 6.08 x $10^8$ | 5.36 x $10^7$ |
| 2 / 22.8 J/cm$^2$ | 5.44 x $10^8$ | 5.68 x $10^7$ |
| 3 / 22.8 J/cm$^2$ | 5.80 x $10^8$ | 5.40 x $10^7$ |
| 1 / 11.4 J/cm$^2$ | 5.40 x $10^8$ | 5.36 x $10^7$ |
| 2 / 11.4 J/cm$^2$ | 6.20 x $10^8$ | 5.76 x $10^7$ |
| 3 / 11.4 J/cm$^2$ | 6.00 x $10^8$ | 5.76 x $10^7$ |
| 1 / 5.7 J/cm$^2$ | 5.96 x $10^8$ | 6.20 x $10^7$ |
| **Average** | **5.84 x $10^8$** | **5.65 x $10^7$** |

### 4.7.7 Antibacterial phototoxicity on biofilm

The phototoxic effect of ZrTCPP films and blue light irradiation was also evaluated against established 24 hours biofilm of *E. faecalis*. The irradiation dose tested was 22.8 Jcm$^{-2}$ corresponding to 20 min of irradiation.

### 4.7.8 Control of biofilm formation

For biofilm development, ON culture of *E. faecalis* was diluted 1:100 in TSB. Three ZrTCPP films and three controls were placed in 12-well plate and exposed to 1.5 ml of bacteria suspension. The samples were incubated for 24 hours (37 °C, 100% humidity and 5% $CO_2$). The bacteria on the surface were stained using SYTO 9 green fluorescent nucleic acid stain from LIVE/DEAD BacLight$^{TM}$ Bacterial Viability Kit according to the manufacturer's instructions (see below). The ZrTCPP films and controls were placed on the glass microscope slides using double-sided tape and analysed with a confocal scanning laser microscopy using 60x water immersion objective. A diode laser emitting at 473 nm was used for SYTO 9 stain. The collected images were processed using ImageJ/Fiji software.

### 4.7.9 LIVE/DEAD BacLight protocol

The LIVE/DEAD BacLight Bacterial Viability Kit contains 300 µl SYTO 9 green fluorescent nucleic acid stain (3.34 mM solved in dimethylsulfoxide (DMSO)) and 300 µl PI (propidium iodide) red fluorescent (20 mM solved in DMSO). The stains are stored in freezer at -20 °C and kept in dark. The SYTO 9 and PI stains are kept separately, but a 1:1 ratio mixture of both stains is also combined in a microfuge tube. The stain was diluted in 0.9% NaCl with the ratio 3 µl stain per 1 ml 0.9% NaCl and the solution was covered with Al foil. Before staining bacteria, the TSB was removed from the wells and the films were washed with 0.9% NaCl. The stain solution was then transferred to each film placed in 12-well plate to completely cover the biofilm (400 µl) followed by 15 minutes dark incubation at RT under Al foil. The stain solution was removed and the films were washed twice with 0.9% NaCl. The films were placed on the glass microscope slides and analysed with a confocal scanning laser microscopy.

### 4.7.10 Phototoxicity of ZrTCPP films

For biofilm development, ON culture of *E. faecalis* was diluted 1:100 in TSB. ZrTCPP films and controls were placed in two 12-well plates and 1.5 ml of bacteria suspension was transferred to each well to completely cover the films. The plates with films were incubated for 24 hours (37 °C, 100% humidity and 5% $CO_2$). The TSB was removed from the wells and replaced by 1 ml of 0.9% NaCl. One of the 12-well plate with half of the samples was placed in the irradiation chamber and irradiated with blue light with a light dose of 22.8 $Jcm^{-2}$ corresponding to 20 min of irradiation. The light box was turned on 20 min before treatment to assure the radiation stability. After irradiation, the samples were placed back in the incubator for 30 min to allow the reactions to continue in the dark. The films were removed from the wells and transferred to 50 ml Falcon tubes containing 10 ml glass beads 3 mm in diameter and 5 ml of 0.9% NaCl and vortexed for 30 s. The suspension was serial diluted in PBS and plated onto BHI agar plates (25 µl). After approximately 24 h incubation (37 °C, 100% humidity and 5% $CO_2$) the colonies were counted (30-300 colonies) and $CFUml^{-1}$ was calculated. Experiments were performed in five replicates (n = 5). Phototoxicity of the ZrTCPP films against established biofilm was also analyzed using confocal scanning laser microscopy with 60x water immersion objective. The irradiated and non-irradiated ZrTCPP films with established biofilm were stained with SYTO 9 and PI stains as described above. A diode laser emitting at 473 nm and a helium-neon laser emitting at 543 nm were used for SYTO 9 and PI stains respectively. The collected images were processed using ImageJ/Fiji software

# 5 Results

This chapter is organized into two main sections; the first section describes the fabrication and characterization of ZrTCPP films, while the second describes the antibacterial assay of ZrTCPP films against gram-positive *E. faecalis*.

## 5.1 ZrTCPP thin films

### 5.1.1 Deposition by spin-coating

This method was inspired by Olsen's protocol of creating ZrTCPP thin films by spin-coating. The aim of this work was to improve the homogeneity of the ZrTCPP thin films. The substrates were cleaned with water and soap, followed by plasma cleansing as described in section 4.2.2. The pre-treating of the substrate is essential for the stability of the thin films, as proved by Olsen.

A challenge from earlier work was to remove the "coffee stain effect" on the edges of the substrate. Various parameters were tested, such as changing the solution volume of deposition, rotational speed, spin time, and concentration. Two significant results that lead to the new improved thin film will be described.

Two solutions for the deposition of the thin film by spin coating were prepared. One with 1.4 g $ZrOCl_2 \cdot 8H_2O$ and the other with 0.09 g of TCPP, each dissolved in 40 ml of ethanol. Then, the mixtures were stored for 24 hours. During storage, the solution with Zr became completely transparent and the other solution with TCPP exhibited a dark purple color. Furthermore, a rapid color change to dark green was observed when these two precursors were combined. The fabricated thin film was highly pigmented, which was correlated to the use of highly concentrated precursors. Furthermore, the observed film became darker when more layers were deposited, as seen in Figure 5.1. Unfortunately, the "coffee stain effect" was still prominent. The concentration of precursors used in this section is provided in Table 5.1. The parameters used in this deposition were the spin duration (t) between each deposition which was 30 seconds, the rotation spin speed (RSS) was 1200 rpm and the deposited droplet volume (DV) was 40 µl.

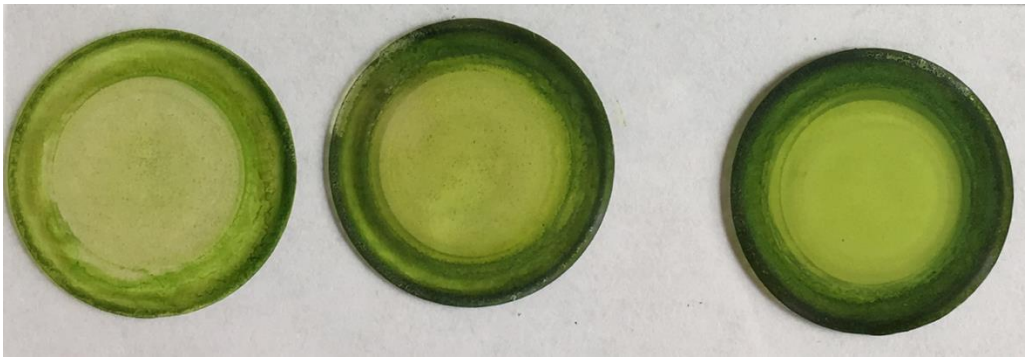

Figure 5.1: ZrTCPP films deposited on $SiO_2$ glass substrates with 5, 10 and, 15 layers, respectively, from left to right. (Parameters: t = 30 s, RSS = 1200 rpm and DV = 20 µl).

**Table 5.1: The precursor's concentration used for the first attempt of spin coating**

| **Precursor** | **Concentration** |
|---|---|
| $ZrOCl_2 \cdot 8H_2O$ | $3.1 \cdot 10^{-2}$ M / 40 ml ethanol |
| TCPP | $2.8 \cdot 10^{-3}$ M / 40 ml ethanol |

The result above proved a correlation between number of depositions and color of the film. Another experiment was to explore the deposition of the thin film at different spin speeds. At low speed (400 rpm), the film was far from homogeneously distributed, as shown in Figure 5.2. An increase in rotational speed from 800 rpm up to 2500 rpm increased the homogeneity of the thin film and decreased the "coffee stain effect", as shown in Figure 5.3. However, the film thickness decreased simultaneously. Table 5.2 presents the concentration of precursors used in this experiment.

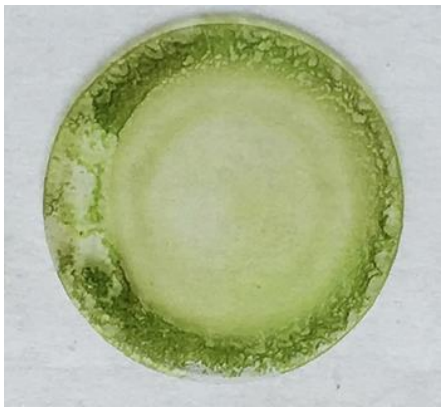

Figure 5.2: ZrTCPP film deposited on $SiO_2$ glass substrate with low rotational speed. (Parameters: t = 30 s, RSS = 400 rpm, and DV = 20 µl).

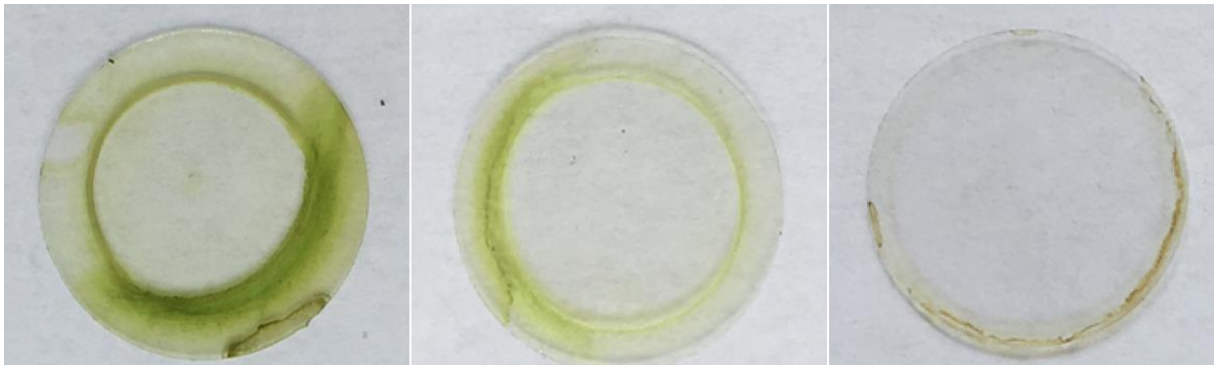

Figure 5.3: ZrTCPP films deposited on $SiO_2$ glass substrates with alternating speed. Increasing from left to right. (Parameters: t = 30 s, RSS = 800, 1200, 2500 rpm, respectively, and DV = 20 µl).

**Table 5.2: Concentration of precursors used in spin speed experiment.**

| **Precursor** | **Concentration** |
|---|---|
| $ZrOCl_2 \cdot 8H_2O$ | $7.8 \cdot 10^{-3}$ M |
| TCPP | $1.3. \cdot 10^{-3}$ M |

The result above demonstrated that a high concentration of precursors would increase the thickness of the film deposited on the substrate. Moreover, it demonstrated that the "coffee stain effect" could be decreased, while simultaneously increasing the homogeneity with the increase of rotational speed. Hence, further exploration of the fabrication of thin film was based on these factors.

The two precursors were prepared by dissolving both 1.31 x $10^{-1}$ M $ZrOCl_2$ x $8H_2O$ and 2.09 x $10^{-3}$ M TCPP in 40 ml of ethanol. The mixtures were stored in amber glasses with an addition of a magnet bar and were stirred on a magnetic stirrer for three days. The solution of Zr became fully transparent, while the solution of TCPP was purple. The thin film was deposited at 4000 rpm, solution volume of 40 µl, and 30 seconds between each deposition. Figure 5.4 reveals that the obtained thin film was homogeneously green. The “coffee stain effect” was successfully removed, and the film was reflecting light evenly. Table 5.3 contains a summary of parameters that were used to fabricate the thin film, as shown in Figure 5.4.

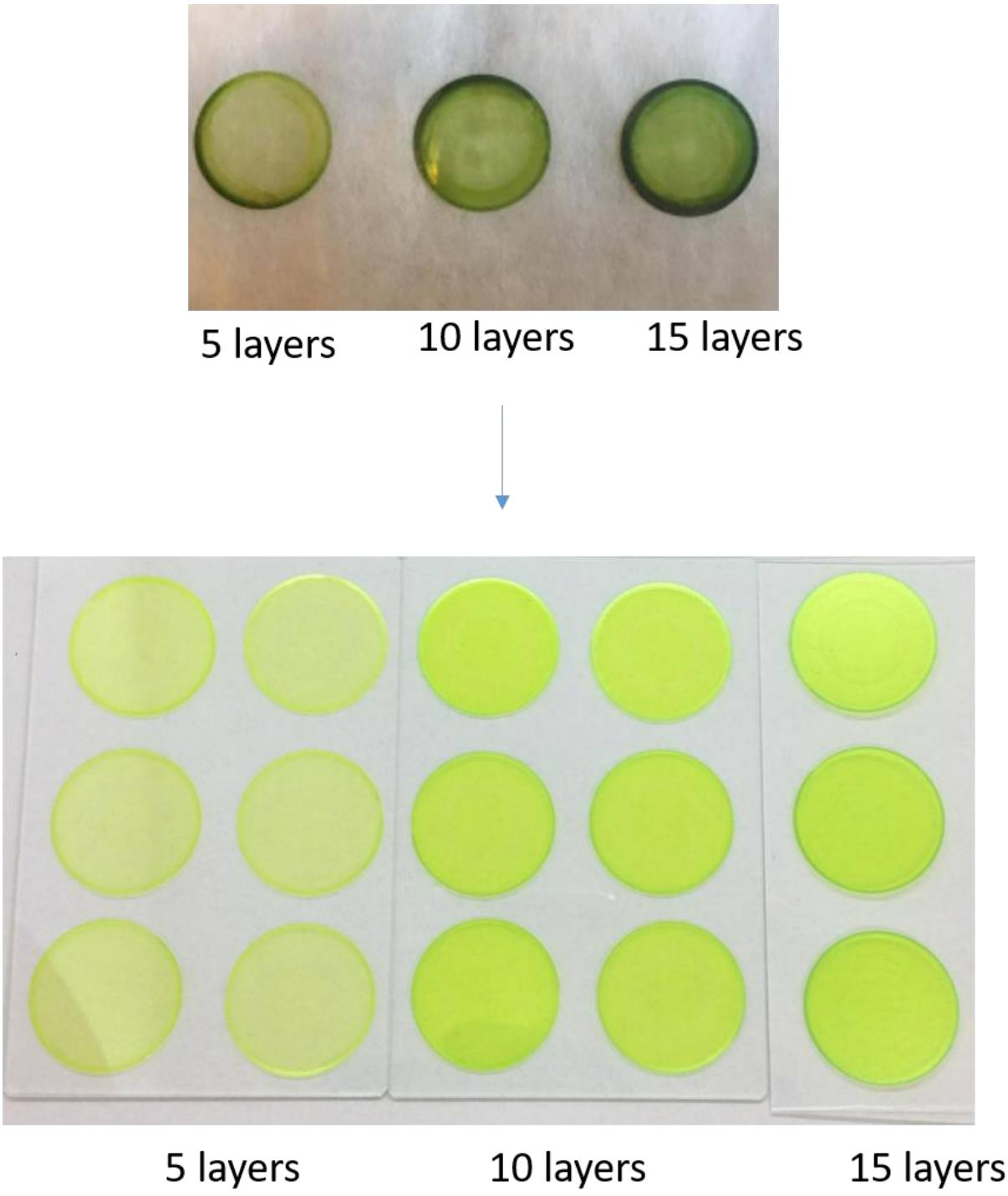


Figure 5.4: A comparison of the ZrTCPP film fabricated by Olsen (top section) to the ZrTCPP films deposited in this thesis (bottom section). (Parameters: t = 30 s, RSS = 4000 rpm, and DV = 40 µl).

**Table 5.3. Summary of parameters used in spin coating for deposition of ZrTCPP**

| | |
|---|---|
| Ink order | i) $1.31 \cdot 10^{-1}$ M $ZrOCl_2 \cdot 8H_20$ / 40 ml EtOH<br>ii) $2.09 \cdot 10^{-3}$ M TCPP/ 40 ml EtOH |
| Deposited droplet volume | 40 µl |

| | |
|---|---|
| Spin speed | 4000 rpm |
| Spin duration | 30 seconds |
| Number of cycles | 5 |
| Substrate | $SiO_2$ |
| Substrate pre-treatment | Section 4.2.2 |

### 5.1.2 Optical properties

After the successful fabrication of ZrTCPP thin films by spin coating, the films were studied by UV-Vis to explore the optica properties of the hybrid material. UV-Vis transmittance measurements were performed on three ZrTCPP thin films with a different number of layers. All three films with 5, 10, and 15 layers showed a Soret band at 452 nm and only one Q-band at 669 nm, as seen in Figure 5.5. The lack of the characteristic four Q-bands of a free-base porphyrin indicates that the Zr was incorporated into the center core of TCPP [58]. The redshift of the Soret band also confirmed the successful fabrication of ZrTCPP thin film. In addition, the diffuse reflection, as seen by a reduction in overall transmission, increased with increasing layers.

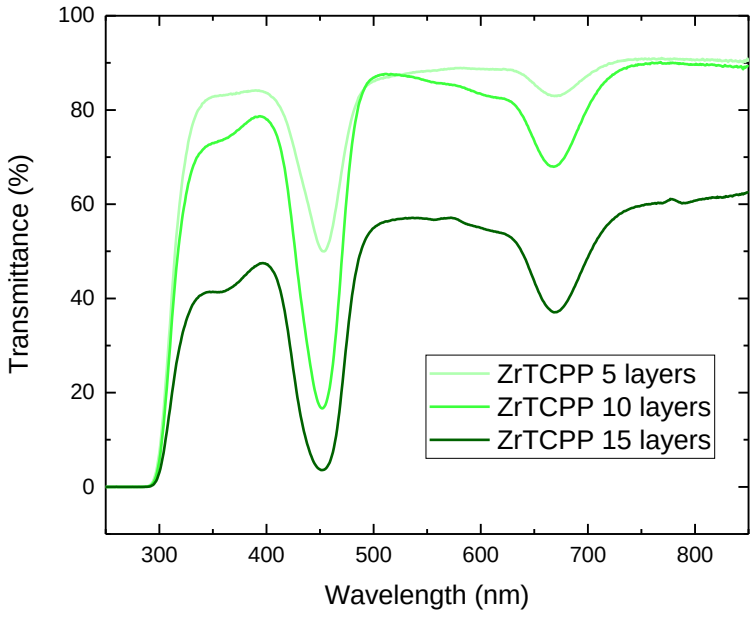


Figure 5.5: UV-Vis transmittance spectra of ZrTCPP thin films with 5, 10 and, 15 layers.

### 5.1.3 FTIR

FTIR measurements were carried out to verify the hybrid nature of ZrTCPP thin film deposited by spin coating. The ZrTCPP samples were fabricated with the standard protocol as described in section 4.3. and the Zr-sample was prepared by depositing 10 layers of Zr-solution by spin-coating. All samples were deposited on an electropolished steel substrate. The TCPP pellet was prepared by mixing TCPP and KBr in a mortar and used a hand press to create a transparent pellet. FTIR analysis of the hybrid ZrTCPP films provide information on the presence of the organic moiety in the films, Figure 5.6.i-ii. In the spectrum of the free-base porphyrin (TCPP), the peaks at 965 $cm^{-1}$ and 1112 $cm^{-1}$ are attributed to the N-H in-plane and out-of-plane bending vibrations of the pyrrole group. This peaks disappeared as the zirconium ion is inserted into the porphyrin ring to form hybrid ZrTCPP complex. Furthermore, the band at 3314 $cm^{-1}$ in the TCPP spectrum is related to the N-H stretching vibrations of the core porphyrin. The broad band at 1251 $cm^{-1}$ is attributed to the axial deformation of the C-N bond, indicating that the structure contains the subunits of pyrrole. Three absorption peaks at 1604, 1505 and 1404 $cm^{-1}$ correspond to the aromatic benzene ring skeleton vibrations, whereas the stretching vibration located at around 1694 $cm^{-1}$ is attributed to C=O groups of the carboxyl acid group. Moreover, the broad absorption for OH band stretching vibrations was seen at around 2600-3600 $cm^{-1}$. The interaction between TCPP and Zr ions in the hybrid ZrTCPP films showed slight changes in the peak position and intensity.

The spectrum for the pure $ZrO_2$ film deposited using a spin coating method display a strong and broad band around 2700 - 3700 $cm^{-1}$ centered at around 3250 $cm^{-1}$ that corresponds to the OH stretching vibrations [52] of free water adsorbed during the drying step, and another band at 1627 $cm^{-1}$ assigned to the OH bending vibrations due to the chemically adsorbed water. Moreover, the weak band at 681 $cm^{-1}$ is attributed to the Zr-O stretching vibrations modes [57]. This weak absorption for Zr-O bond was also observed for ZrTCPP films that confirms the presence of the metal component in the hybrid structure.

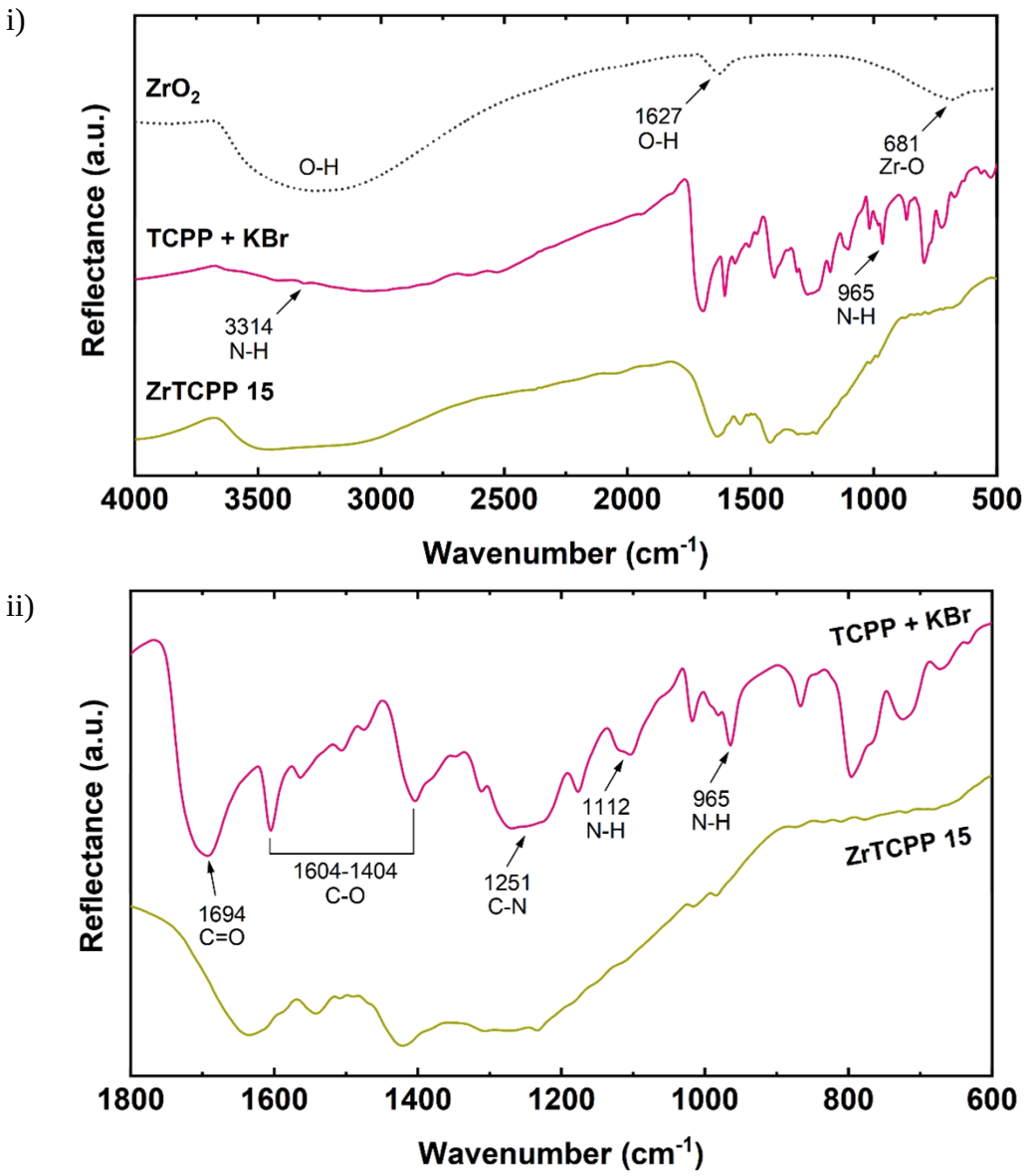


Figure 5.6: FTIR reflection spectra of: (a) $ZrO_2$, TCPP and ZrTCPP 15 (4000-500 $cm^{-1}$) and (b) TCPP and ZrTCPP 15 (1800-600 $cm^{-1}$).

The FTIR spectra of the ZrTCPP films deposited with different numbers of deposition cycles (5, 10 and 15) show similar features, however the intensity of the peaks varies depending on the TCPP/Zr content (Figure 5.7). Furthermore, the decrease of the broad absorption for OH groups around 2700-3700 $cm^{-1}$ with the number of deposition cycles indicates that the water molecules are removed from the sample with higher thickness of the film. The FTIR analysis proved the hybrid nature of deposited ZrTCPP films and that both TCPP and zirconium ions were incorporated into the film.

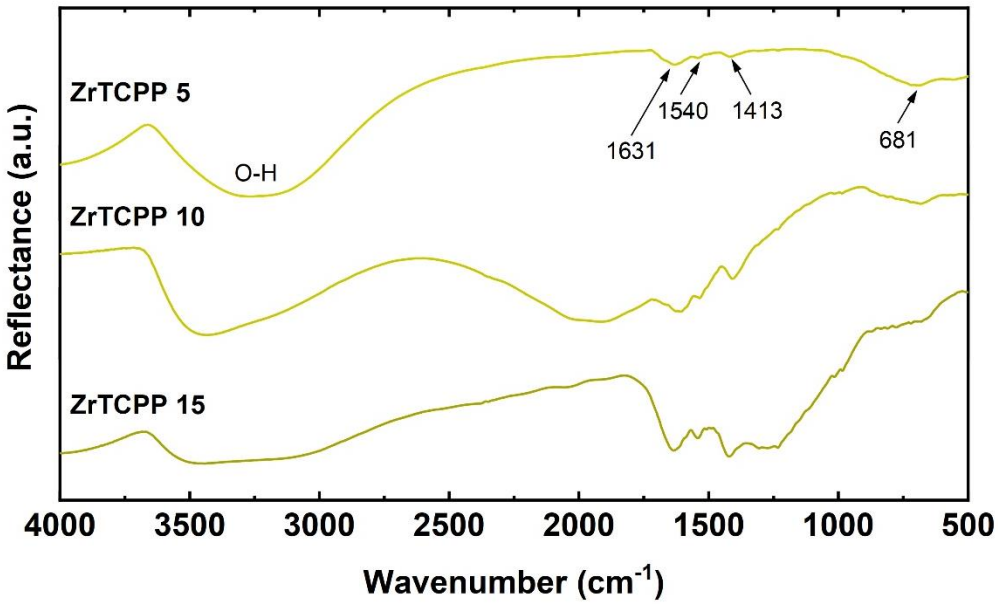


Figure 5.7 FTIR reflection spectra of ZrTCPP films with 5, 10 and 15 layers.

### 5.1.4 Reproducibility

To evaluate the reproducibility of the developed synthesis protocol of the deposition process, a campaign of six replicas with five layers of ZrTCPP and three replicas with ten layers were performed. All sample followed the same standard protocol described in section 4.3 and was fabricated on the same day. The resulting films were evaluated by UV-Vis transmittance measurements. Figure 5.8.i-ii showed that the synthesis protocol of these films was highly reproducible with a relative standard deviation of 1.43% for (n = 6) 5 layers and 11.70% for (n = 3, including one outlier) 10 layers at 452 nm. However, the relative standard deviation is lower at the 669 nm for five and ten layers, 0.34% and 1.95%, respectively.

i)

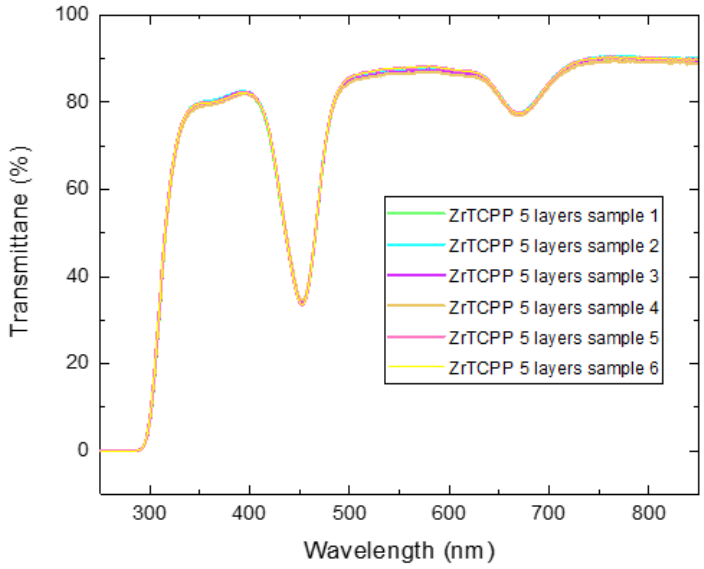


ii)

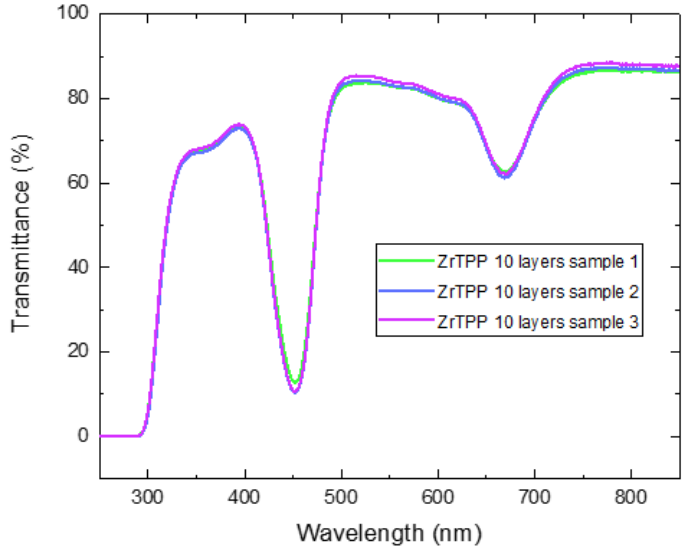


Figure 5.8: UV-Vis transmittance spectra of ZrTCPP. i) 6 samples of 5 layers ZrTCPP thin films. ii) 3 samples of 15 layers ZrTCPP thin films.

### 5.1.5 Saturation

While the spin-coating principle appears robust and reproducible, we also wanted to evaluate if a possible self-limiting type of reaction could take place. This was performed by excessive addition of one reactant to observe if this would lead to excessive growth or not. Both the Zr and TCPP reactants were tested for saturation by comparing a series of excessive use of one of the reactants with the standard procedure. For Zr, the number of deposited Zr sequences within one cycle was increased between 1-7 while the TCPP was kept to one. A total of 5 cycles with standard protocol as described in section 4.3 were used for all experiments. Figure 5.9 shows a

color change of the thin film by changing the number of deposited Zr per cycle. In addition, it was observed that the film also became less shiny and rougher for increased sequences of Zr exposure. Hence, it was proven difficult to assess if the color change is due to an increase of saturation or precipitation of a material we assume is $ZrO_2$. For TCPP, the number of deposited TCPP sequences within one cycle was increased between 1-5 while the Zr was kept to one. Increasing amount of TCPP did not exhibit any significant optical change of the thin films, which indicates that TCPP was fully saturated.

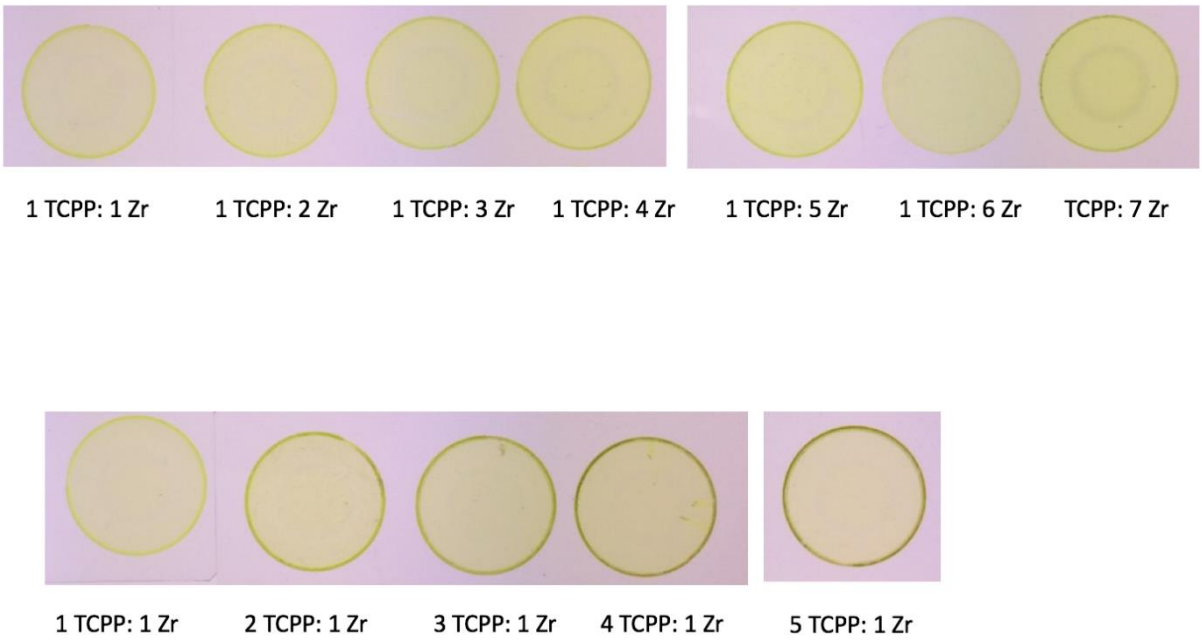


Figure 5.9: Thin film of ZrTCPP from the saturation evaluation.

To evaluate that the ZrTCPP films were saturated with precursors, UV-Vis measurements of the films were performed. As seen in Figure 5.10.i, an increase of Zr leads to an overall reduction in transmittance, most likely due to increased diffuse scattering from precipitated $ZrO_2$. In contrast, the spectra of different amount of TCPP shows no significant change (Figure 5.10.ii).

i)

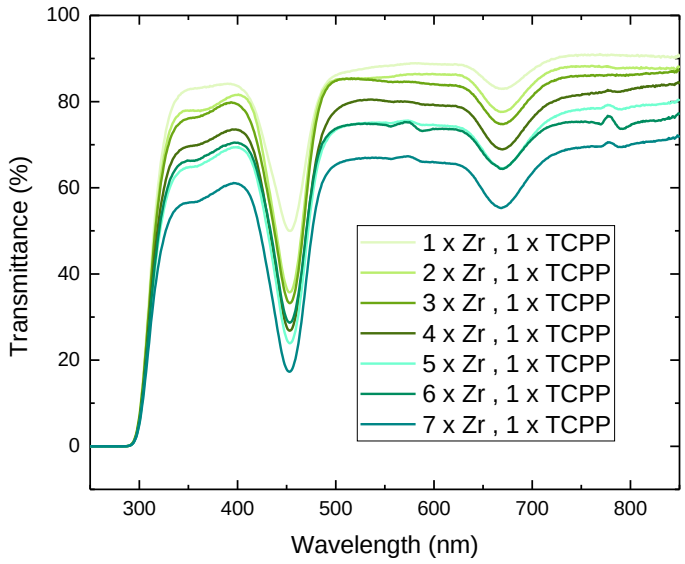


ii)

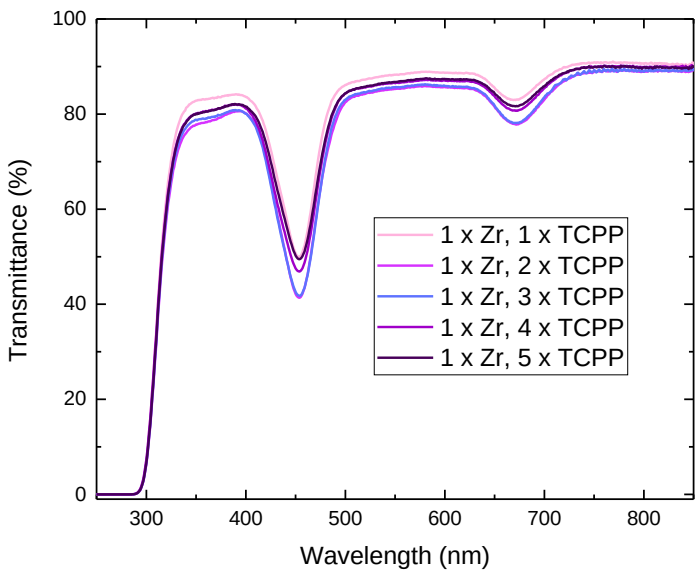


Figure 5.10: UV-Vis transmittance spectra of ZrTCPP thin films. i) Evaluation of Zr saturation. ii) Evaluation of TCPP saturation.

The intensity of the Soret and Q-bands were calculated by subtracting the overall background and is given in Figure 5.11 and 5.12. This shows very little variation from 2 cycles of Zr, indicating saturation almost from the first cycle of Zr exposure. The variation is also very little for TCPP, indicating saturation.

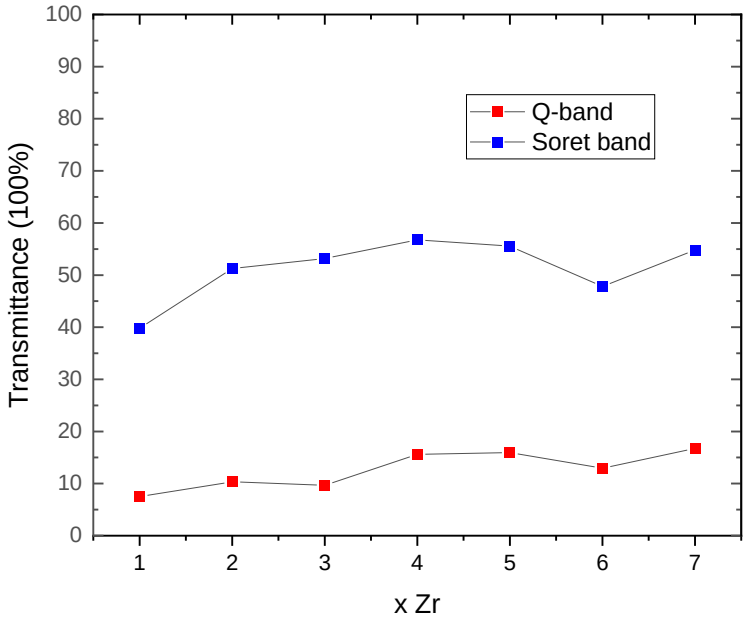


Figure 5.11: Variation in UV-Vis transmittance of the absorption at 450 nm (Soret-band) and 675 nm (Q-band) with increasing number of Zr-layers added to the protocol.

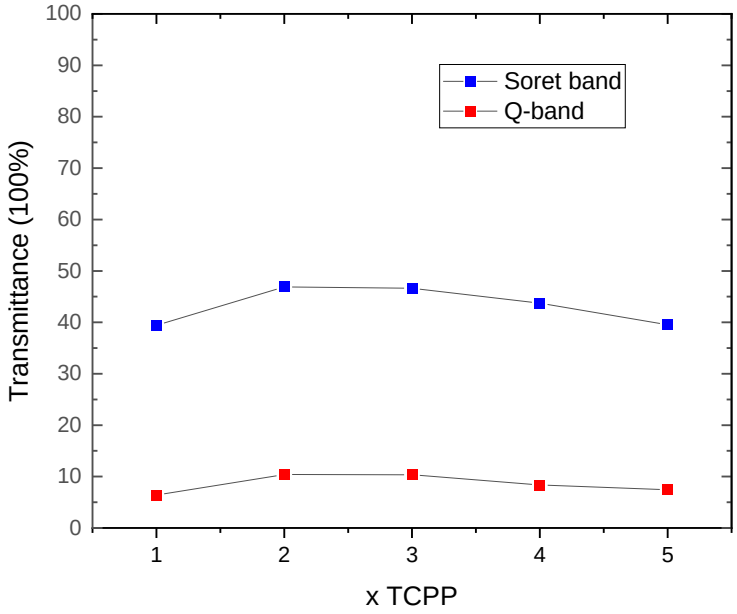


Figure 5.12: Variation in UV-Vis transmittance of the absorption at 450 nm (Soret-band) and 675 nm (Q-band) with increasing number of TCPP-layers added to the protocol.

### 5.1.6 Absorbance of solutions with different concentration

In order to explore the molar absorption coefficient and the stoichiometry effects of ZrTCPP, the ratios of Zr and TCPP with different concentrations were evaluated by UV-Vis absorption. Note that the Zr and TCPP solutions were highly diluted in comparison to the concentration used to grow thin film by spin-coating. This was necessary to achieve good measurements and prevent direct precipitation of ZrTCPP.

In the first experiment, solutions of Zr ($8.13 \times 10^{-4}$ M) and TCPP ($2.45 \times 10^{-5}$ M) dissolved in ethanol were prepared. For each UV-Vis measurement, the amount of Zr was kept constant. Meanwhile, the amount of TCPP was gradually increased to create five solutions, where the Zr and TCPP volume ratio ranged from 1:1 to 1:5. In order to study the effect of mixing Zr and TCPP, solutions of only TCPP and only Zr were also measured, which acted as a reference to analyze and compare with the obtained data. Figure 5.13 shows that the UV-Vis spectra of TCPP exhibited typical free-base porphyrin features with a strong Soret band (416 nm) and four Q-bands between 513 nm and 664 nm [51]. In addition, the Soret band exhibited a neck, which indicated H-stacking of the TCPP in ethanol [98]. Moreover, there was no absorption for Zr, as expected. UV-Vis absorbance spectra reveal that the 1 to 1 ratio of TCPP and Zr exhibited a

split of the Soret band, where the second peak was at 450 nm. In addition, the spectrum was slightly read-shifted. In the magnified area of the Q-bands, the four peaks showed a lower intensity and red-shifted in comparison to spectra of only TCPP solution. Furthermore, it was observed that as the concentration of TCPP increased, the peak at 450 nm decreased, and the spectra became more similar to the free-base TCPP. The results proved that new chemical bonds between TCPP and Zr emerged.

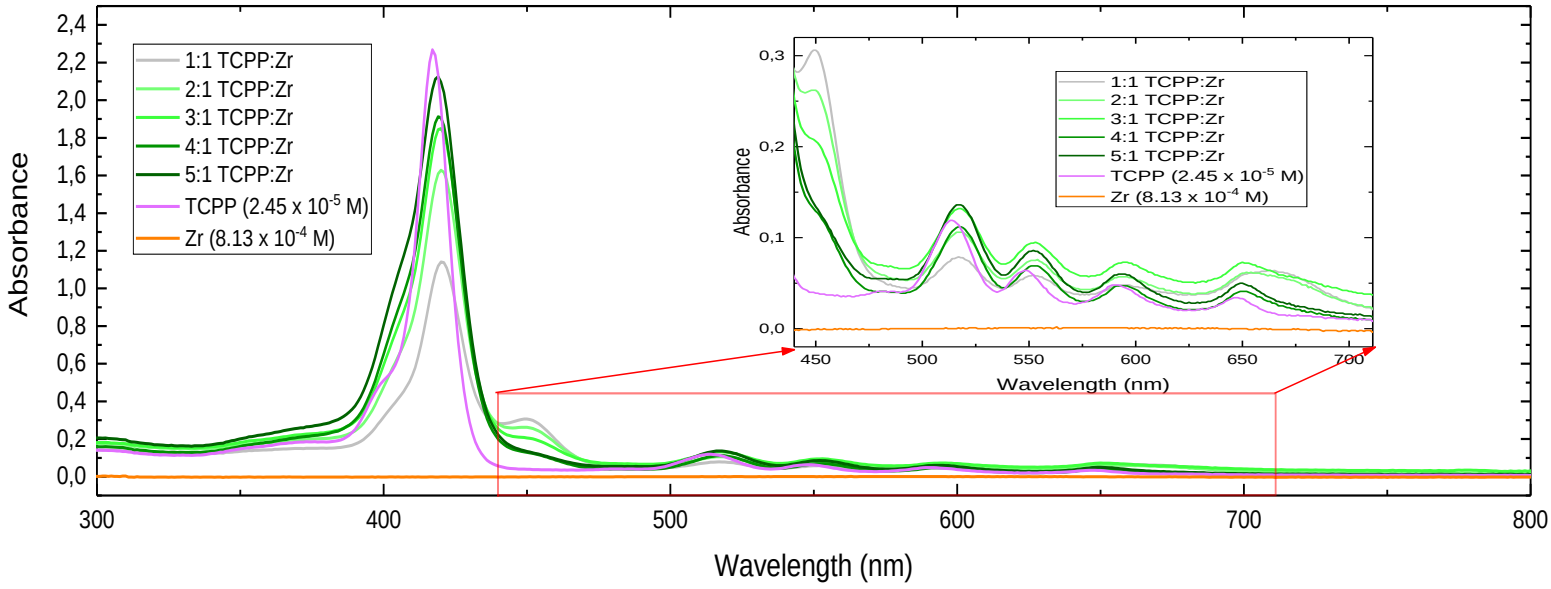


Figure 5.13: UV-Vis absorbance spectra of ZrTCPP solution with different concentration ratios.

The second part of the experiment was to explore the increase of zirconium in respectively to TCPP, which was also performed by the UV-Vis absorption measurement. The solutions of Zr ($1.3 \times 10^{-4}$ M) and TCPP ($3.92 \times 10^{-5}$ M), both dissolved in ethanol, was prepared. It was used at a different concentration than above to achieve better data while increasing the volume of TCPP. For each measurement, the amount of TCPP was kept constant. However, the amount of Zr was increasing. The spectrum for only TCPP, only Zr, and the 1:1 ratio of Zr and TCPP was as expected. As shown in Figure 5.14, the peak at 416 nm decreased with the increasing Zr. Interestingly, the peak at 450 nm also decreased with the increasing Zr, except for the ratio of 3:1. Comparing the peak ratio of the split Soret band, it clearly revealed that with the increasing amount of Zr, the peak at 450 nm is growing, while the peak at 416 nm is decreasing. In addition, the redshift of the spectrum was clearly shown at 664 nm. Moreover, the four Q-bands were shifting towards only one Q-band with the increasing amount of Zr, which indicates higher symmetry of the porphyrin. The molar absorption coefficient was calculated by

analyzing the UV-Vis absorbance spectrum further, Appendix B.1. With the assumption that the molar absorption coefficient of ZrTCPP can be transferred from that in solution to the one condensed on the substrates, and a density of ZrTCPP as provided by Morris et al. [99], the thickness was determined to be around 55 nm.

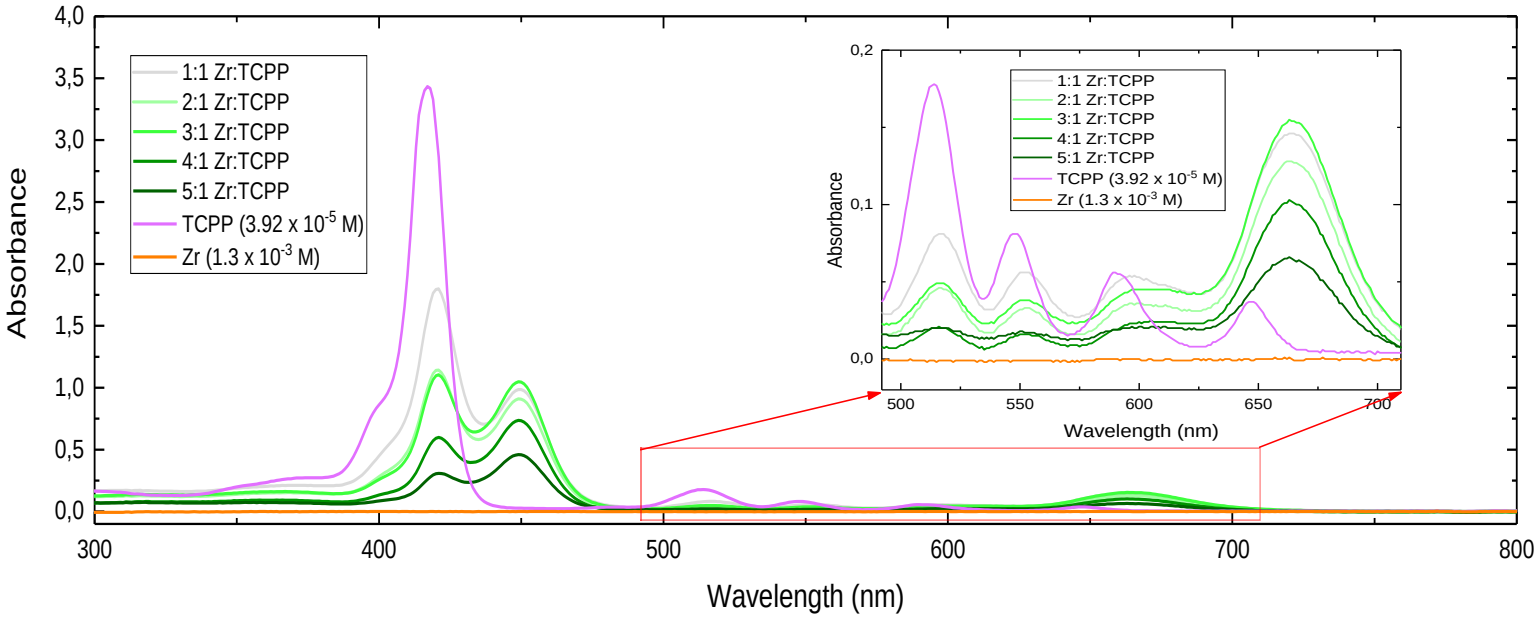


Figure 5.14: UV-Vis absorbance spectra of ZrTCPP solution with different concentration ratios.

### 5.1.7 Washing step

We wanted to explore the possibility of growing a thin film with an additional washing step of ethanol between the depositions of precursors. If so, a process very similar to ALD-type of growth could be achieved. The cycle started with the deposition of Zr, followed by a cleansing step with ethanol. Finally, after the deposition of TCPP, the washing step was performed, which concluded the first cycle of deposition. The amount of ethanol varied, as shown in Figure 5.15. The obtained results showed that the washing step did not wash away the precursors. However, we observed that by increasing the amount of ethanol in washing did reduce the film thickness. By looking at the samples, there was no difference in thickness between two and three-time more ethanol. Hence, it was sufficient to use two times ethanol in cleansing. These results inspired the second method of thin film fabrication.

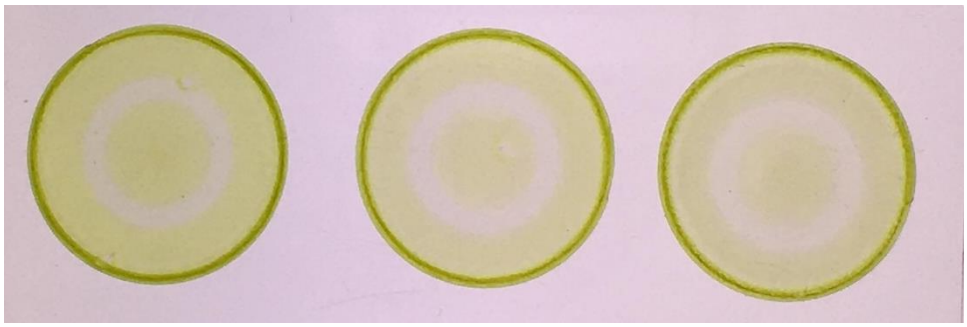

Figure 5.15. The deposition of the thin film included a washing step with ethanol. (a) 1 x EtOH. (b) 2 x EtOH. (c) 3 x EtOH.

### 5.1.8 Layer-by-layer liquid deposition

The result from section 5.1.7 showed that it was possible to include a washing step in the cycle of film deposition. This washing step resembled the purge step in ALD described in section 3.1.4, which inspired the exploration of the second method for fabrication of thin film, a layer-by-layer liquid deposition in a confined chamber. The chemical reaction and growth of thin film in situ were studied by UV-Vis absorption, where absorption was measured as a function of scan number (time).

From the UV-Vis absorption measurement in situ, the obtained absorption data for the Soret Band will be presented, while the Q-bands exhibited a very low intensity and will not show good representative data. Note that the spectrum of 448 nm was shifted along the Y-axis for more readable data. The first step of the cycle was to introduce TCPP solution into the chamber where the observed color was light purple, which corresponds to the initial peak for the spectra of 415 nm as seen in Figure 5.16.i. Then, followed by a step of ethanol for washing. As a result, the peak of porphyrin was observed to decrease. Finally, followed by a deposition of Zr and ethanol, which concluded the first cycle and did not exhibit any significant change in the spectrum. However, when the second cycle started, we observed an initial peak of TCPP at 415 nm, which quickly disappeared. Then, absorption of spectra 448 increased, which indicates that TCPP reacted with Zr in a rapid manner. Then, followed by a wash with ethanol, which decreased the absorption. Moreover, unexpectedly the absorption rapidly decreased to zero when Zr was introduced, which indicated that the Zr removed the ZrTCPP hybrid material in the chamber. The same trend was observed to be repeated for each following cycle. The introduced porphyrin that quickly reacts with Zr is also well illustrated by the contour plot.

(Figure 5.16.ii). In addition, it also illustrates the repetitive pattern of the reaction for each cycle. Figure 5.17 is a summary of the deposition cycle.

i)

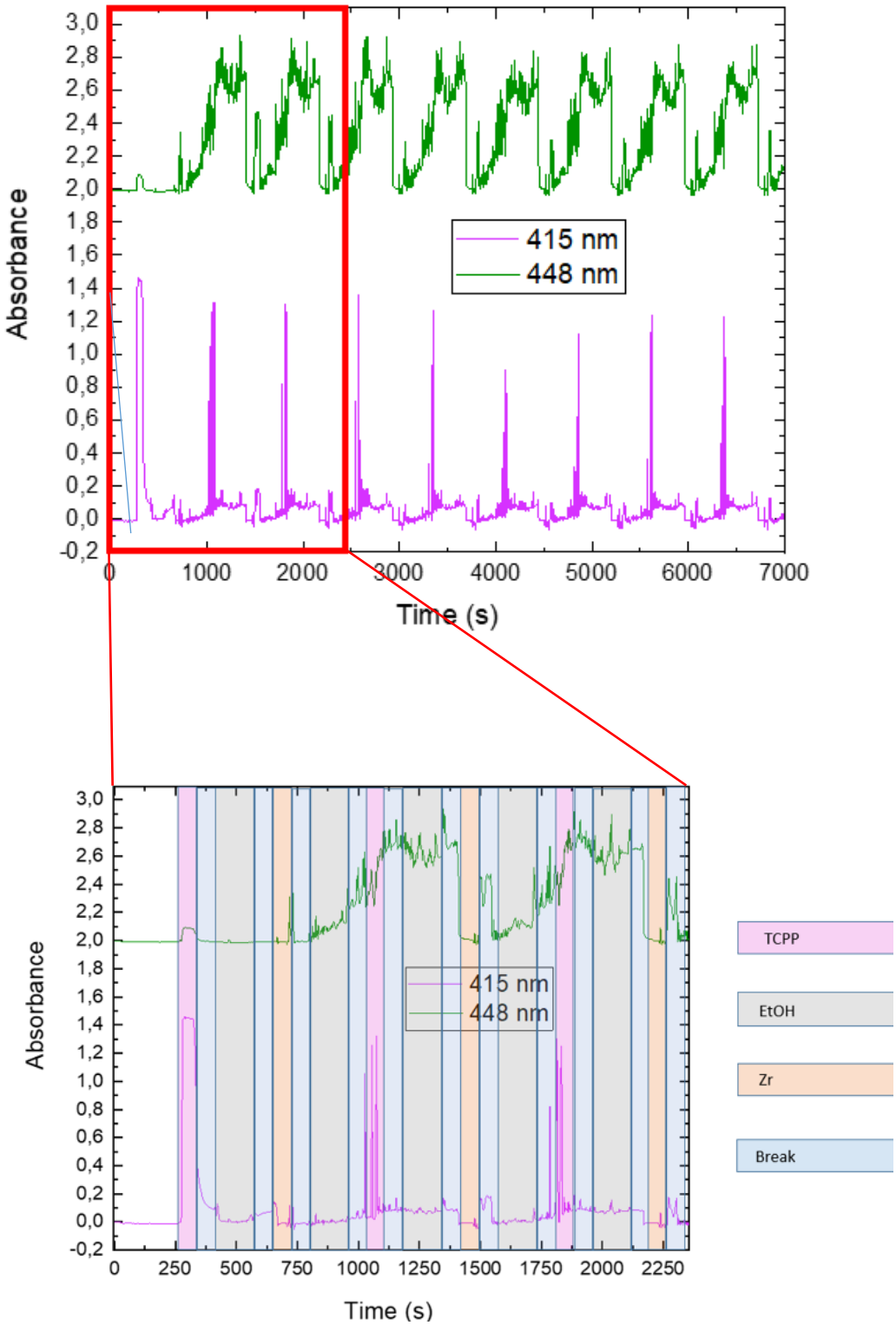

ii)

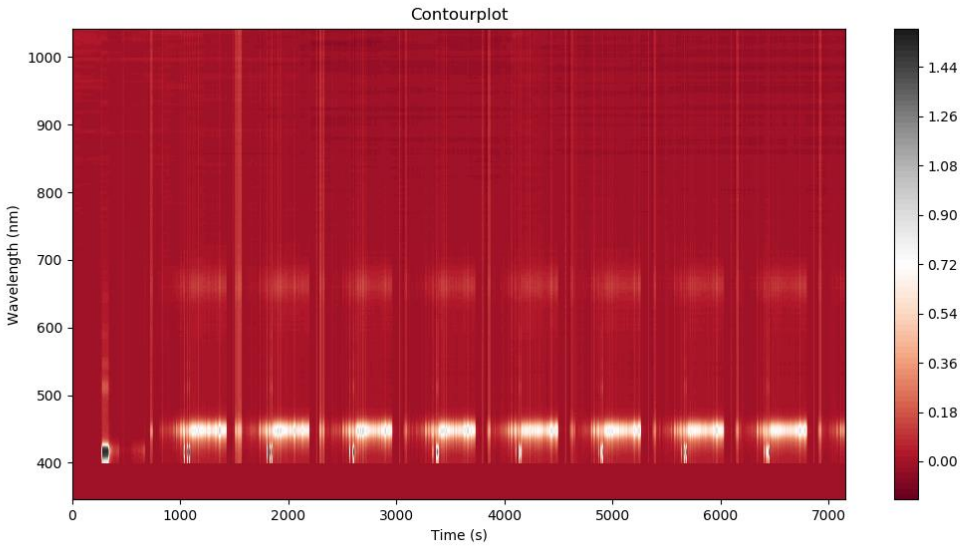


Figure 5.16: i) Absorbance data from UV-Vis plotted as function of time (s). The enlarged area shows the depositions. ii) Contour plot that presents the intensity of absorbance.

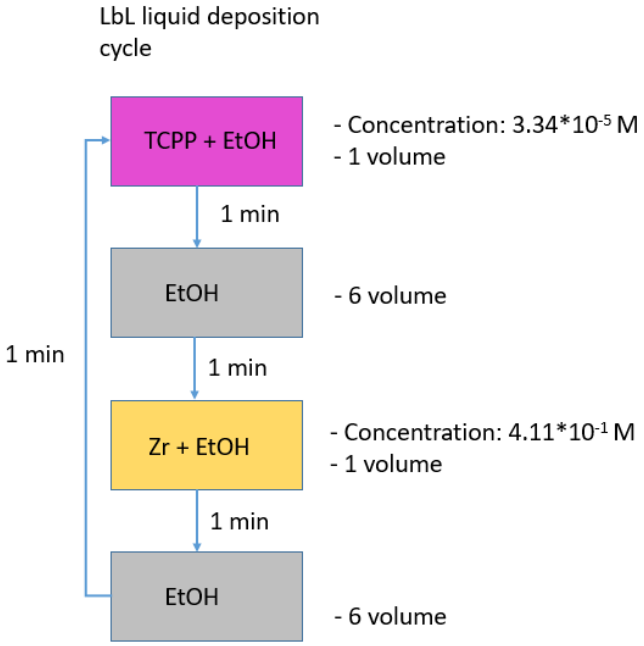


Figure 5.17. A schematic illustration of the LbL liquid deposition cycle. One volume represent the quantity of solution needed to fill the volume inside the flow-cell one time.

Olsen has proved that a glass substrate coated with an additional layer of $ZrO_2$ by ALD promoted the attachment of precursors in comparison to an untreated surface. Therefore, the glass wall of the chamber was coated with $ZrO_2$ by ALD to aid the growth of the film. In addition, the TCPP solution was prepared with ammonia to increase the incorporation of Zr into the core center. However, it was observed that the layer of coating and addition of ammonia did not exhibit any additional benefits in comparison to the glass wall treated with plasma. We observed a similar trend as the experiment above. We decided to continue the exploration of LbL liquid deposition with a plasma cleansed glass wall, as this was more favorable to produce.

Further exploration was to increase the exposure time to evaluate if that would favor the chemical reaction between Zr and TCPP (Figure 5.19). The result showed a similar trend as the earlier experiment (Figure 5.18). Hence, the obtained result demonstrated no growth of thin film even though clear exposure of the different reactants are seen. However, it was interesting that the chemical reaction was repetitive down to its smallest details in fluctuation of intensities, as shown in Figure 5.18, even though the reaction time was 1 hour for each deposition sequence.

i)

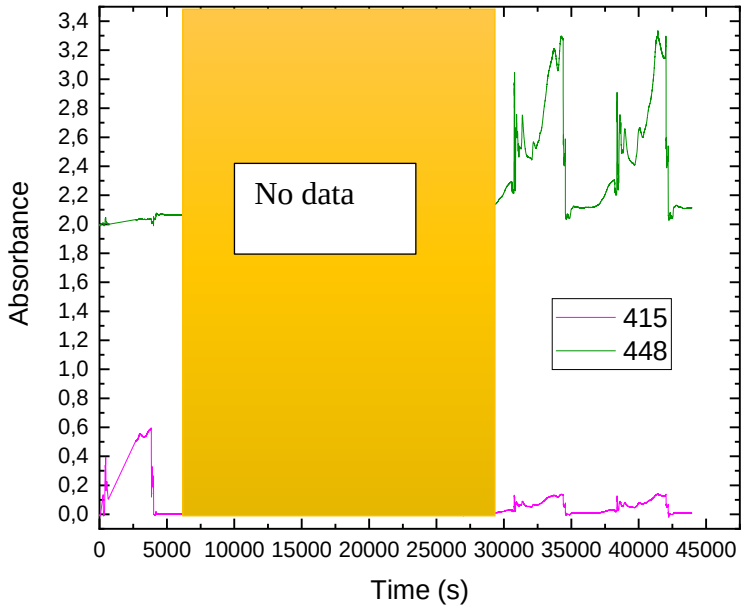

ii)

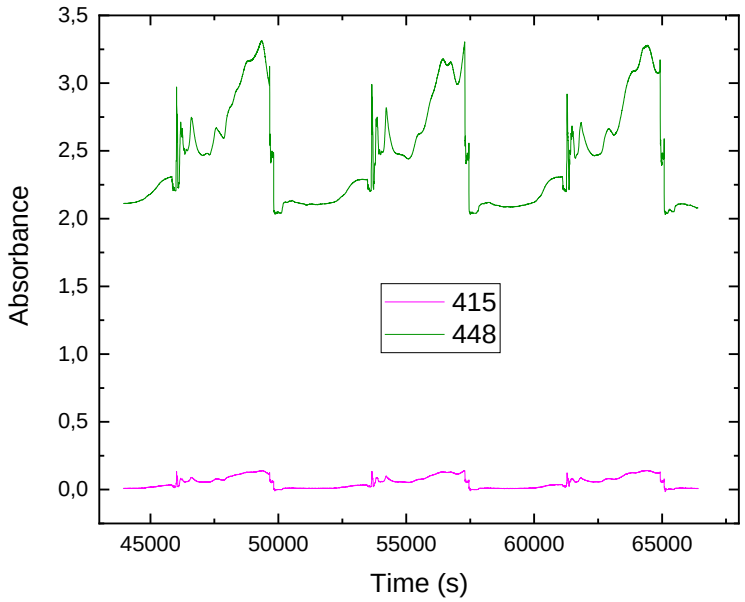
Absorbance
Time (s)
415
448
3,5
3,0
2,5
2,0
1,5
1,0
0,5
0,0
45000
50000
55000
60000
65000

iii)

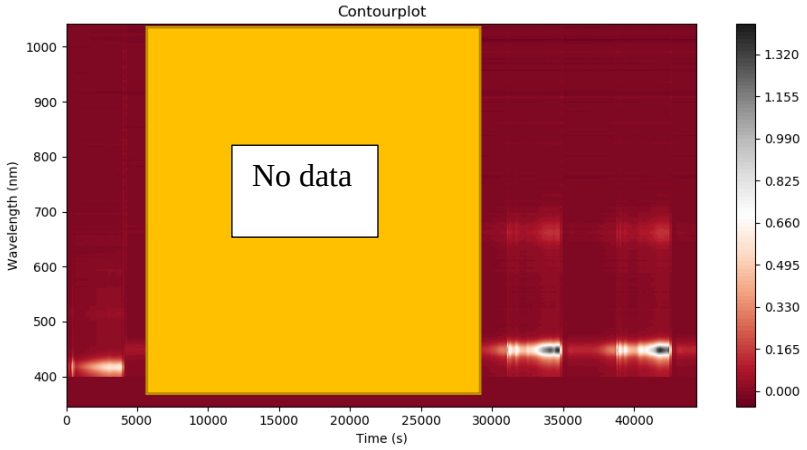
Contourplot
No data
Wavelength (nm)
Time (s)
1000
900
800
700
600
500
400
0
5000
10000
15000
20000
25000
30000
35000
40000
1.320
1.155
0.990
0.825
0.660
0.495
0.330
0.165
0.000

iv)

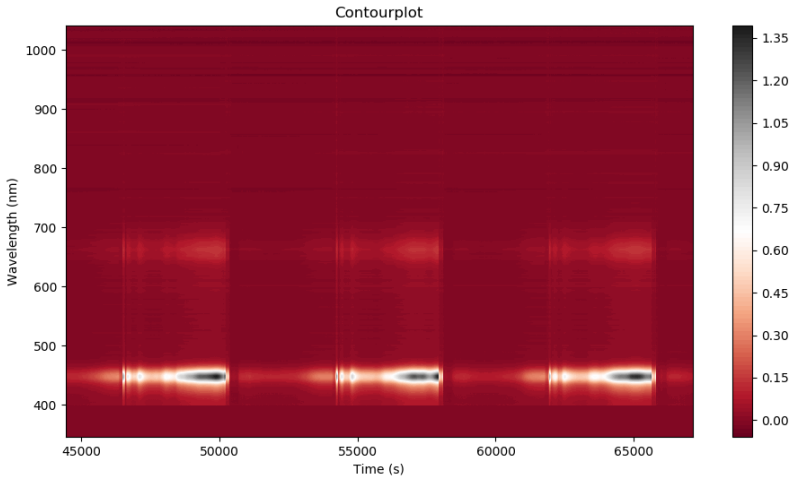
Contourplot
Wavelength (nm)
Time (s)
1000
900
800
700
600
500
400
45000
50000
55000
60000
65000
1.35
1.20
1.05
0.90
0.75
0.60
0.45
0.30
0.15
0.00

Figure 5.18: i) Absorbance data from UV-Vis plotted as function of time (s). ii) Part 2 of (i). iii) Contour plot that presents the intensity of absorbance. iv) Part 2 of (iii).

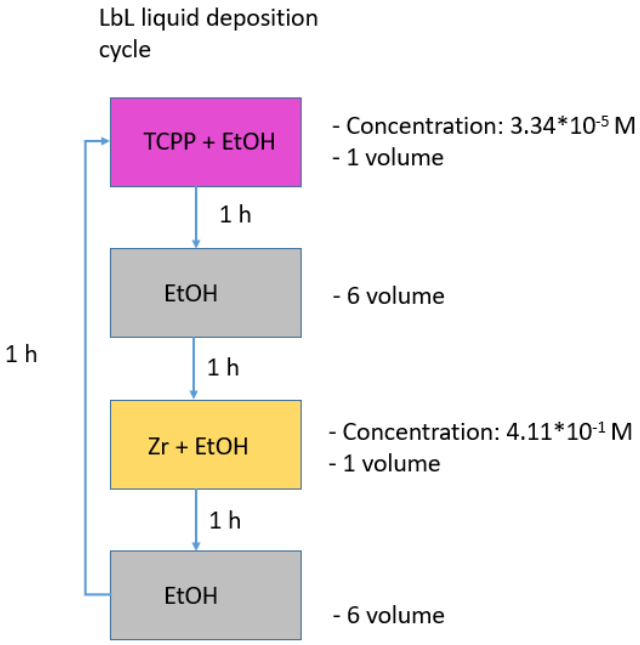


Figure 5.19. A schematic illustration of the LbL liquid deposition cycle. One volume represent the quantity of solution needed to fill the volume inside the flow-cell one time.

Further work was to increase the concentration of TCPP, which rather resulted in the precipitation of ZrTCPP in the chamber. Therefore, the measurement was disturbed and not included. Considering that ZrTCPP may produce photoactivated molecules and, in theory, affect its own growth, an experiment was performed in complete darkness and without any UV-Vis measurements. (UV-Vis measurements do require a light source.) Nevertheless, the flow-cell after the experiment was observed to be similar to the flow-cells from the experiment above as inspected with a light microscope.

Finally, the deposition of TCPP in a cycle was performed twice, as seen in Figure 5.21, in order to evaluate the reaction in the chamber with more volume of TCPP. The detector reached saturation when TCPP was introduced, seen as sharp transitions in color in the contour plot Nevertheless, the contour plot shows that even with twice the volume of TCPP to Zr (Figure 5.20), the reaction is similar to the results above.

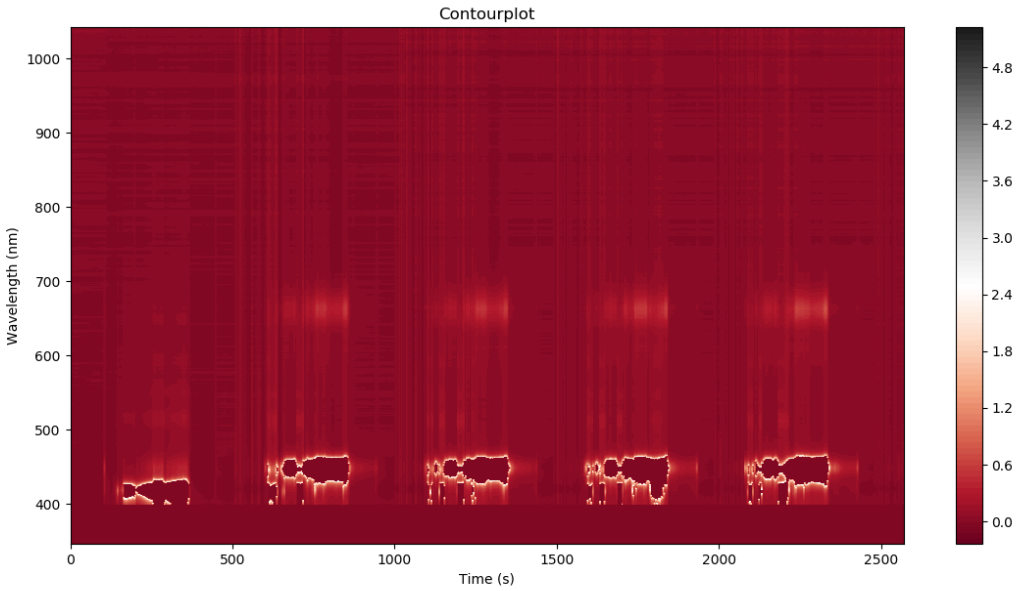


Figure 5.20. Contour plot that presents the intensity of absorption.

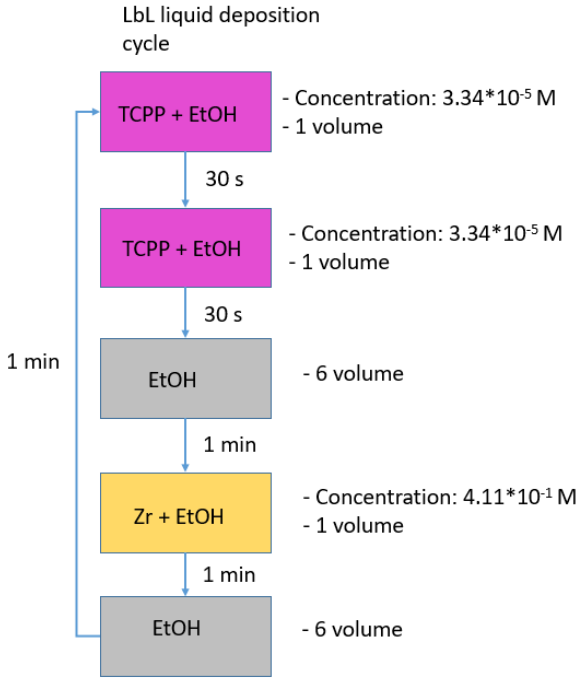


Figure 5.21: A schematic illustration of the LbL liquid deposition cycle. One volume represent the quantity of solution needed to fill the volume inside the flow-cell one time.

### 5.1.9 Stability in aqueous solution

As an overall aim of the ZrTCPP films is to use for antibacterial properties, they will also be exposed to a solution. During the antibacterial experiment, the thin film samples will be submerged into the bacteria suspension in saline solution and incubated for 140 min. Hence, the thin film samples have to be stable in water and do not dissolve over at least this time period. To test if the films are stable in water, 5 layers of ZrTCPP were prepared by the standard protocol (section 4.3), afterward immersed in DI water for 3 hours (Figure 5.22.i). We observed that that the initial green color of the thin film gradually changed into a brown color, where the surface was covered with small air bubbles (Figure 5.22.ii). This was not expected as it has been reported that the ZrTCPP framework is very stable in an aqueous solution [61]. The change of color was further characterized by UV-Vis (Figure 5.23). The transmittance spectra showed that the strong Q-band at 672 nm for ZrTCPP film disappeared after the film was immersed in water for three hours. In addition, we observed a blue shift of the Soret band and weak four Q-bands.

i)

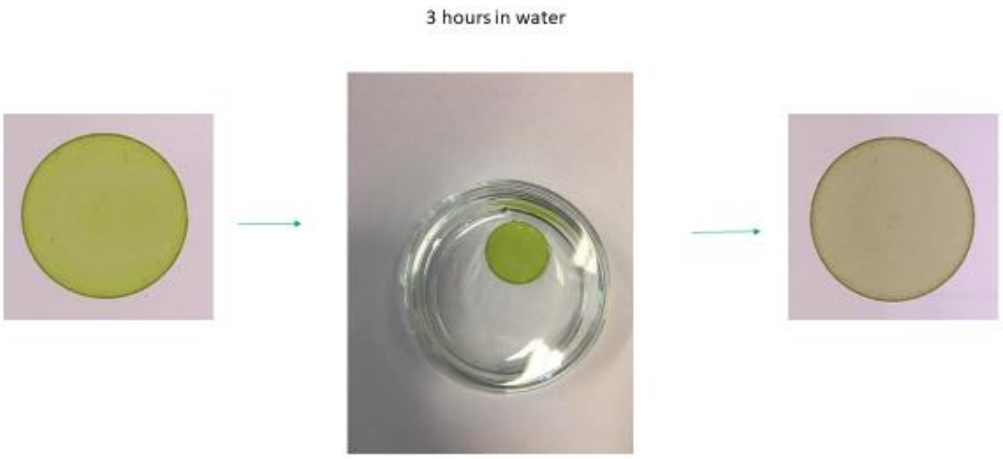


ii)

Figure 5.22: i) Thin film immersed in water for 3 hours. ii) Color comparison. On the left side is ZrTCPP thin film before submerged in water. On the right side is ZrTCPP thin film after submerged into water.

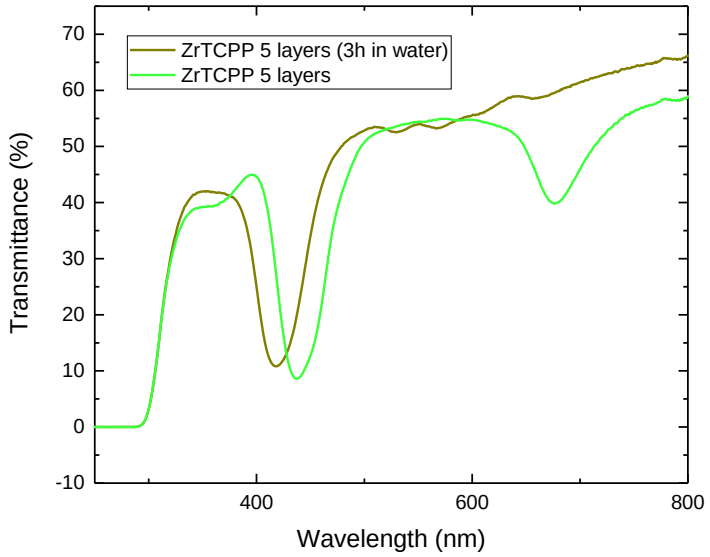


Figure 5.23: UV-Vis transmittance spectra of 5 layers ZrTCPP film before and after water treatment.

The results above suggested that the film in water exhibit a similar characteristic of a free-base porphyrin, which indicate that Zr was leaked into the water. In order to understand the interaction of Zr and TCPP in water, an approach to titration was performed. First, a green solution was prepared by mixing Zr-solution and TCPP-solution. Furthermore, the mixture was then added into a beaker with DI water and the green color turned brown-green-yellow, as shown in Figure 5.24. By adding more solution of Zr, the color turned back to bright green, which was contrary to adding more TCPP, the color turned muddy brown.

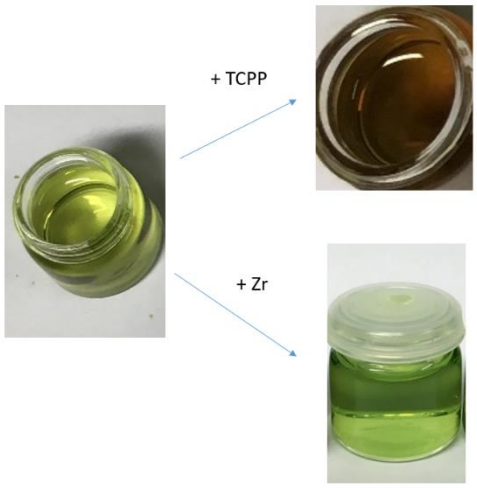


Figure 5.24: ZrTCPP solution in water. The mixture exhibited a green color by adding more Zr and brown with more TCPP.

Figure 5.25 illustrates that the addition of more Zr shift the equilibrium towards the ZrTCPP hybrid. Subsequently, 5 layers of ZrTCPP were immersed in DI water with the addition of 600 µl Zr dissolved in ethanol. After 3 hours in the solution, the thin film was still green, and the integrity was still intact.

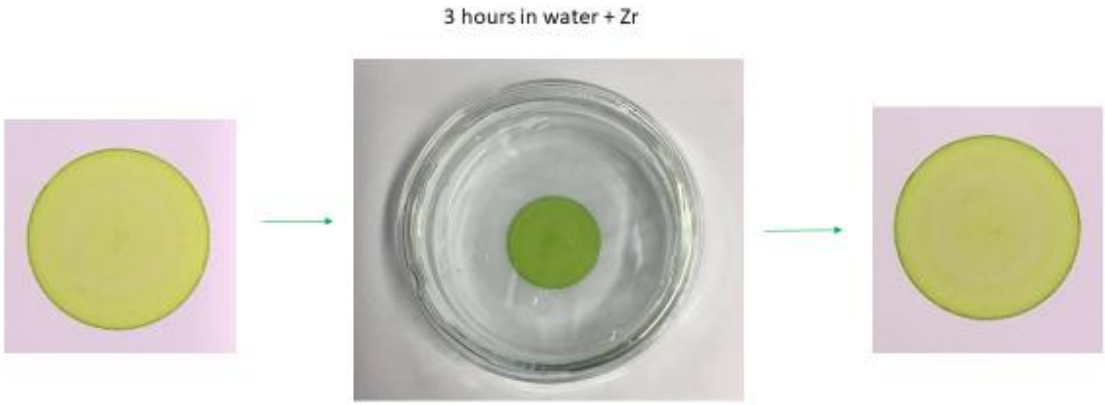


Figure 5.25: 5 layers of ZrTCPP in water with the addition of Zr do not change color.

### 5.1.10 Recovery of lost Zr in the water

Observation from earlier experiments suggested that Zr leached out from the thin film in contact with water. Furthermore, we wanted to study if it was possible to recover the integrity of the film. The thin film with 5 layers of ZrTCPP was immersed in DI water for 3 hours. It was thereafter air-dried. The film was brown as expected. After 24 hours, the thin film was immersed back into DI water with the addition of Zr dissolved in ethanol for three hours. We observed that the film had not recovered entirely back into the strong green color. However, it seemed that it had a light green tint to it. UV-Vis transmittance in Figure 5.26 showed that the peak at 420 nm was broadening and exhibited a weak middle split at 420 nm and 450 nm. This confirms that some zirconium was able to get back into the thin film.

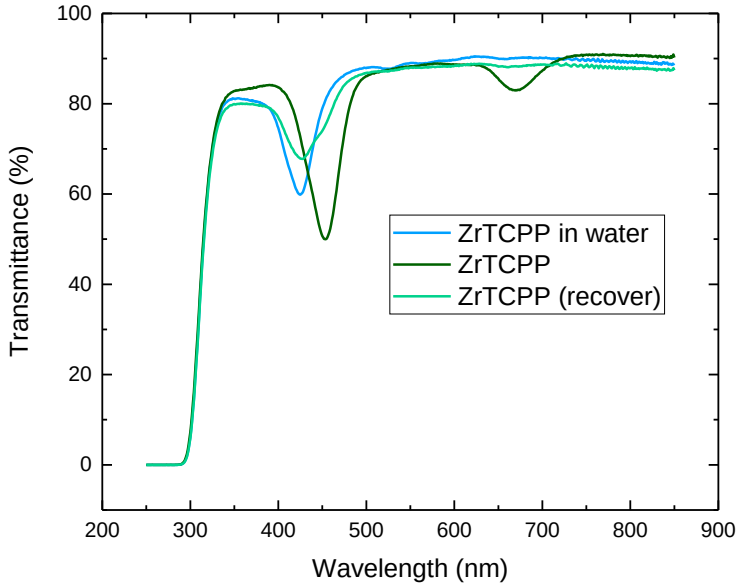


Figure 5.26: UV-Vis transmittance of ZrTCPP film before and after water treatment. Also, ZrTCPP film after recovery approach.

### 5.1.11 Stability at various pH-levels

From Olsen's thesis, it was suggested that the addition of ammonia ($NH_3$) would favor the incorporation of metals into the core center of TCPP because deprotonated TCPP was more susceptible to positively charged ions. Based on this, to prevent Zr from detachment at the core center of TCPP, the thin film was tested against different levels of pH. A thin film of 5 layers with ZrTCPP was immersed into three solutions with different pH for 3 hours. Distilled water was mixed with HCl and $NH_3$ to achieve solutions with pH around 2 and 8-9, respectively. The third solution was untreated distilled water with a pH of around 7. As shown in Figure 5.27, the thin films that were exposed to basic and neutral water exhibited the same brown color.

Meanwhile, the film in acidic water was observed to be green but was partly dissolved into the solution. The films were further characterized by UV-Vis transmittance. Figure 5.28 shows that the film treated in acidic water exhibited a Soret band at 448 nm and shifting of the Q-band. The spectra indicate that the porphyrin was protonated, which explained the green color. Moreover, for the thin film exposed in basic and neutral water, the Soret band was blue-shifted, and the prominent Q-band at 672 nm disappeared, but four low-intensity Q-bands were observed.

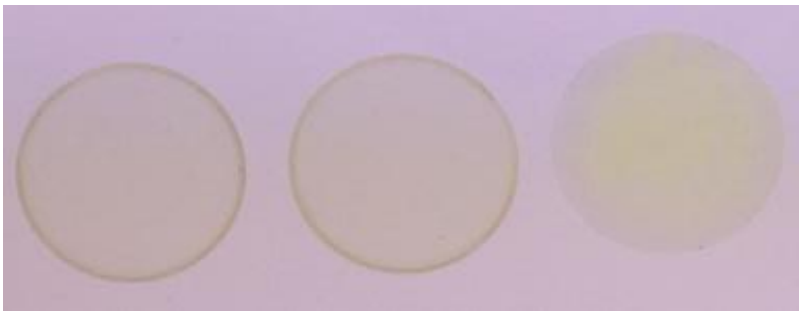

Figure 5.27: 5 layers ZrTCPP film treated in different solutions. On the right: treated with basic water. In the middle: treated with neutral water. On the left: treated with acidic water.

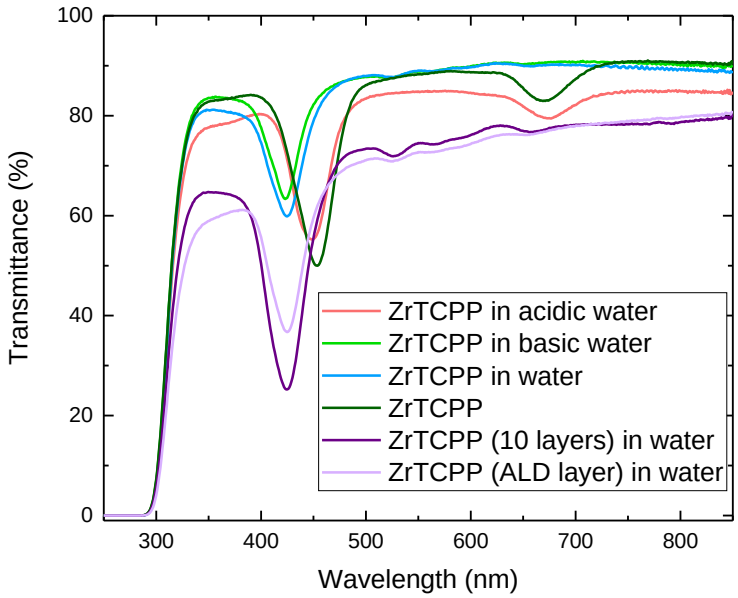


Figure 5.28. UV-Vis transmittance of ZrTCPP films treated in different solutions.

Apart from studying the films, the solution can also be analyzed by UV-Vis to seek for traces of leakage. As expected, the spectra for acidic water that was light green showed leakage of ZrTCPP (Figure 5.29). The basic water and neutral water were transparent and clear. First, the

clearness of neutral water was confirmed by UV-Vis that shows no absorbance. Surprisingly, the spectrum of basic water showed some leakage of TCPP. Basic water should increase the bonding of the metal ion at the center of the TCPP. However, it can also enhance formation of $ZrO_2$ as precipitate.

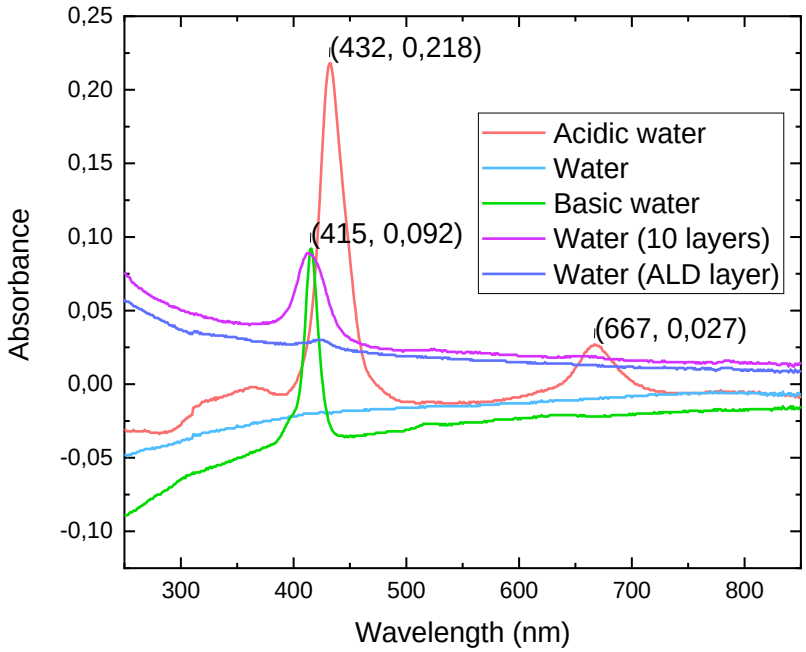


Figure 5.29: UV-Vis absorbance spectra of different solutions.

UV-Vis absorbance of TCPP and ZrTCPP solutions in water were also evaluated to compare with the obtained data. It was observed a blue shift and broadening of the Soret band and redshift of the Q-band for ZrTCPP solution in water (Figure 5.30). This is contrary to only TCPP in water, where it was observed a middle split of the Soret band and four Q-bands.

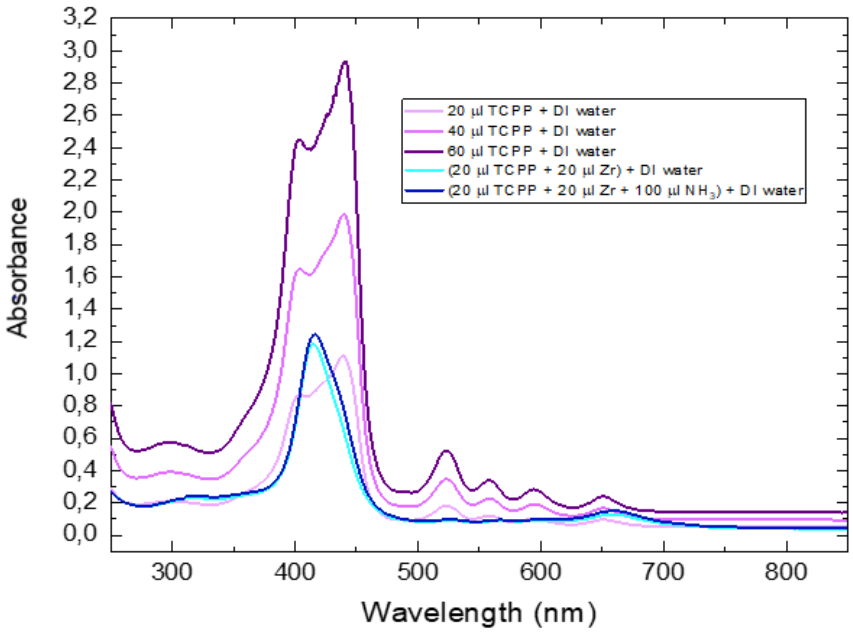


Figure 5.30: UV-Vis absorbance spectra of ZrTCPP and TCPP solution in water.

### 5.1.12 Elemental mapping by EDS

The results from the water test experiment suggested that Zr was leaked from the thin film. Nevertheless, there was still film on the substrate. To explore if the remaining film after exposure to water had Zr, and EDS mapping was performed. For each sample, measurement was performed at three points to ensure quality. Table 5.5 presents the results of different samples when looking for Zr in EDS.

**Table 5.5: Summary of EDS results**

| Sample | Indication of Zr in the sample (Yes/No) |
|---|---|
| ZrTCPP 5 layers | Yes |
| ZrTCPP 10 layers | Yes |
| ZrTCPP 15 layers | Yes |
| ZrTCPP 5 layers after 3 hours in DI water | Yes |
| ZrTCPP 10 layers after 3 hours in DI water | Yes |
| ZrTCPP 5 layers after 3 hours in acidic water | Yes |
| ZrTCPP 5 layers after 3 hours in basic water | Yes |

### 5.1.13 Saline solution

The stability of 5 layers ZrTCPP films were also evaluated in 0.9% NaCl for 3 and 24 hours. The UV-Vis transmittance shows a split Soret band at 427 nm and 446 nm after 3 hours in 0.9% NaCl (Figure 5.31). Interestingly, the transmittance at 427 nm is the same after 24 hours. However, the peak at 446 nm decreased. Also, the four Q-band became more prominent.

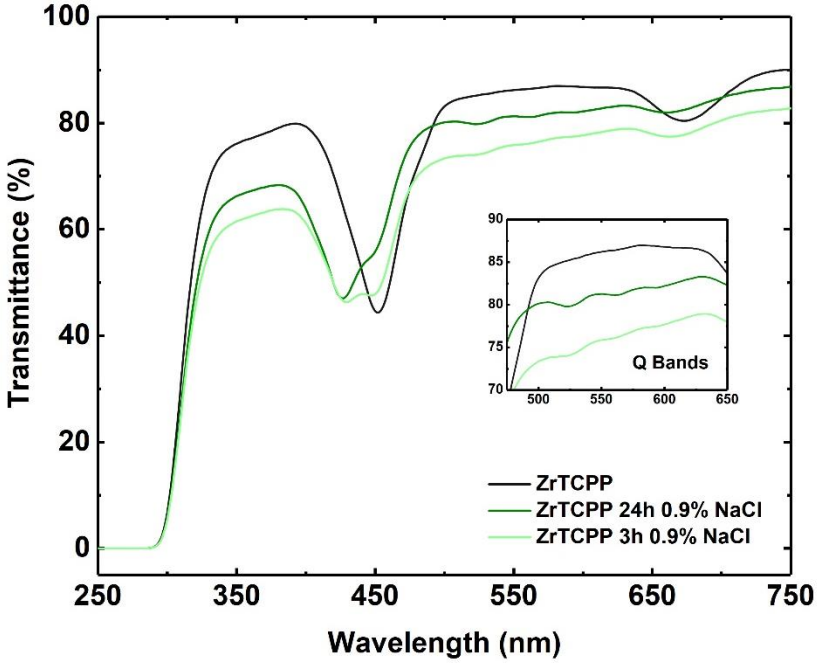


Figure 5.31: UV-Vis transmittance spectra of ZrTCPP immersed in 0.9% NaCl for 3 and 24 hours.

### 5.1.14 Contact angle

The WCA on ZrTPP films was measured using the Theta Lite (Biolin Scintific) contact angle meter. The photographs (Figure 5.32) show that these surfaces were at the border line between hydrophobic and hydrophilic. Furthermore, it was observed that the hydrophobicity decreases with increasing number of layers, 5, 10, and 15, respectively.

i) ii)

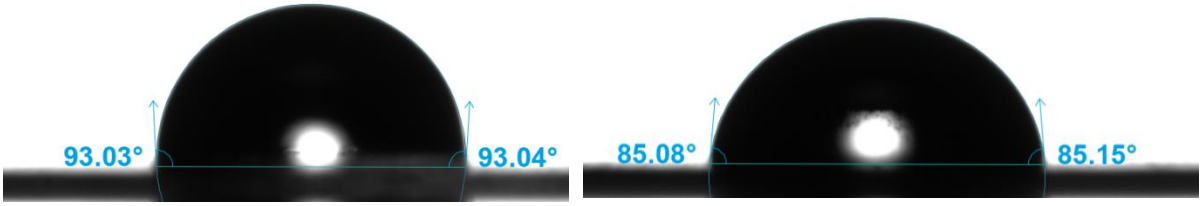


iii)

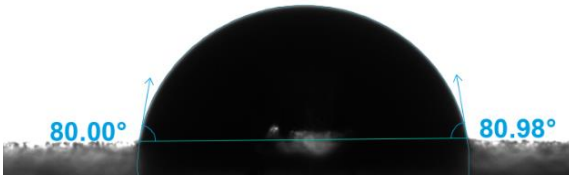


Figure 5.32: Photographs of the contact angle for ZrTCPP thin films with different layers. i) 5 layers. ii) 10 layers. iii) 15 layers.

### 5.1.15 XRD

The crystallinity of deposited ZrTCPP films was evaluated with XRD, which resulted in the diffractograms in Figure 5.33. The obtain patterns show that the films are mostly amorphous. The observed peak around 2θ = 6-7° was suggested to be an indication of ZrTCPP hybrid. Moreover, this peak intensity increased with increasing deposition of Zr in a cycle with samples prepared in section 5.1.5 (Figure 5.33.ii).

i)

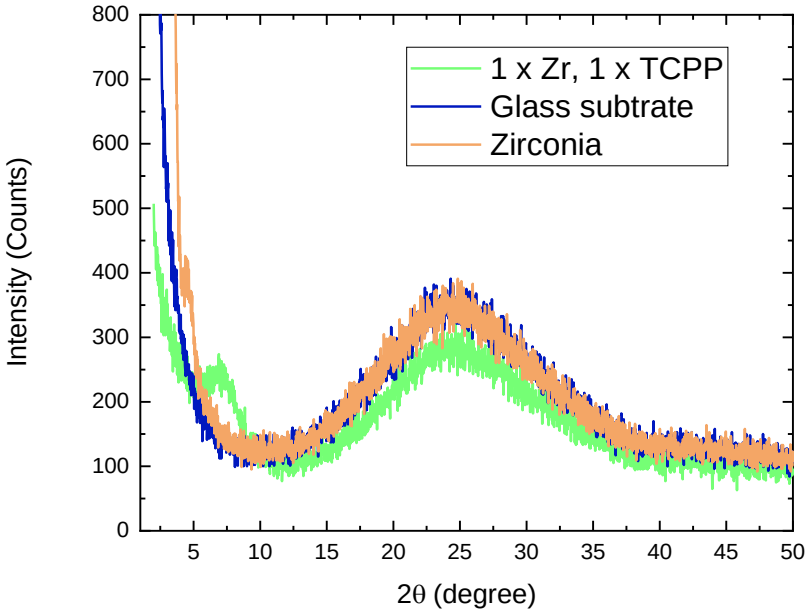


ii)

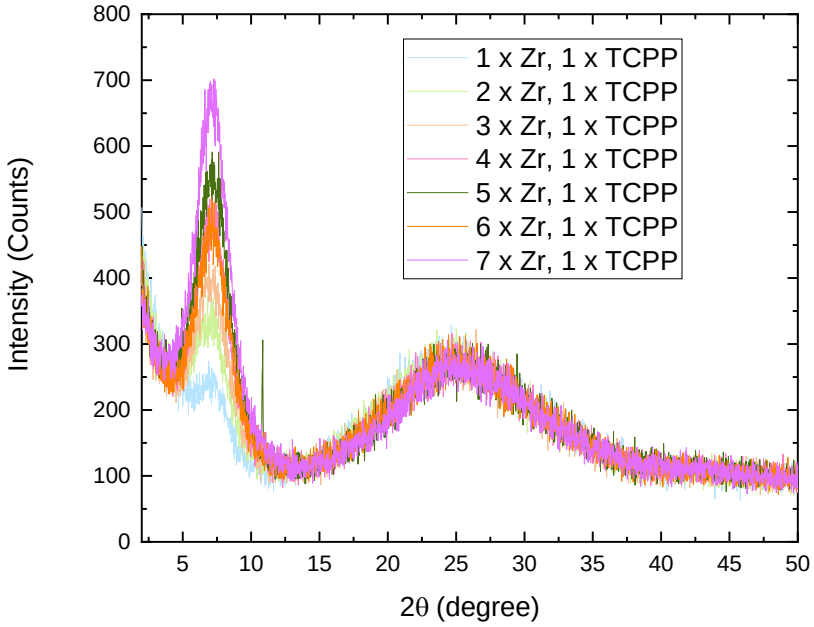


Figure 5.33: Diffractogram of ZrTCPP. i) A comparison of 5 layers of ZrTCPP, glass substrate, and zirconia deposited on glass substrate. ii) A comparison of the increasing Zr per deposition cycle.

### 5.1.16 AFM

The surface topography of the ZrTCPP films deposited on the glass substrates was measured by AFM (Figure 5.34). The overall root-mean-square (RMS) surface roughness of the ZrTCPP films estimated by AFM was 6.4 nm. However, the line profile across the single features on the surface from the AFM images shows a higher value of about 35 nm (Figure 5.34.ii). The films are rather topographically uniform (uniform surface roughness) at the nanoscale.

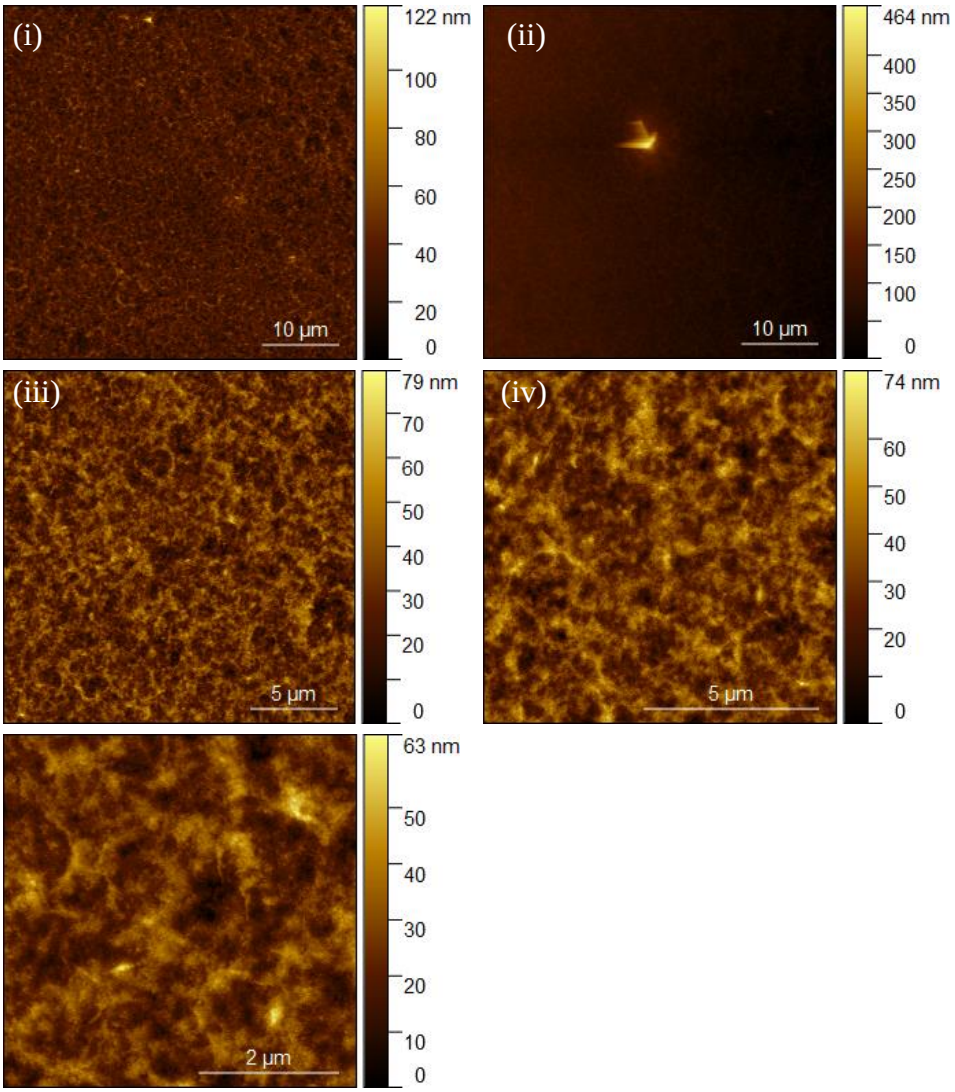


Figure 5.34: Surface topography as measured by AFM for 5 layers ZrTCPP films with a scan size of (i-ii) 45 x 45 µm$^2$, (iii) 20 x 20 µm$^2$, (iv) 10 x 10 µm$^2$ and (iv) 5 x 5 µm$^2$.

### 5.1.17 Ellipsometry

We were not able to achieve a good data fit for the ellipsometry data.

### 5.1.18 Summary of result

Figure 5.35 shows a summary of the main result in the first part of the experiments. The result section presented the different steps performed in order to achieve a homogenous thin film of ZrTCPP by spin coating. Furthermore, the characterization shows that the UV-Vis absorbance spectrum of ZrTCPP films is different than for TCPP porphyrin. In addition, our method of

synthesis was reproducible. Finally, the water stability experiments show that there was still film on the substrate after treated in water. Hence, the films were ready to be evaluated for antibacterial properties.

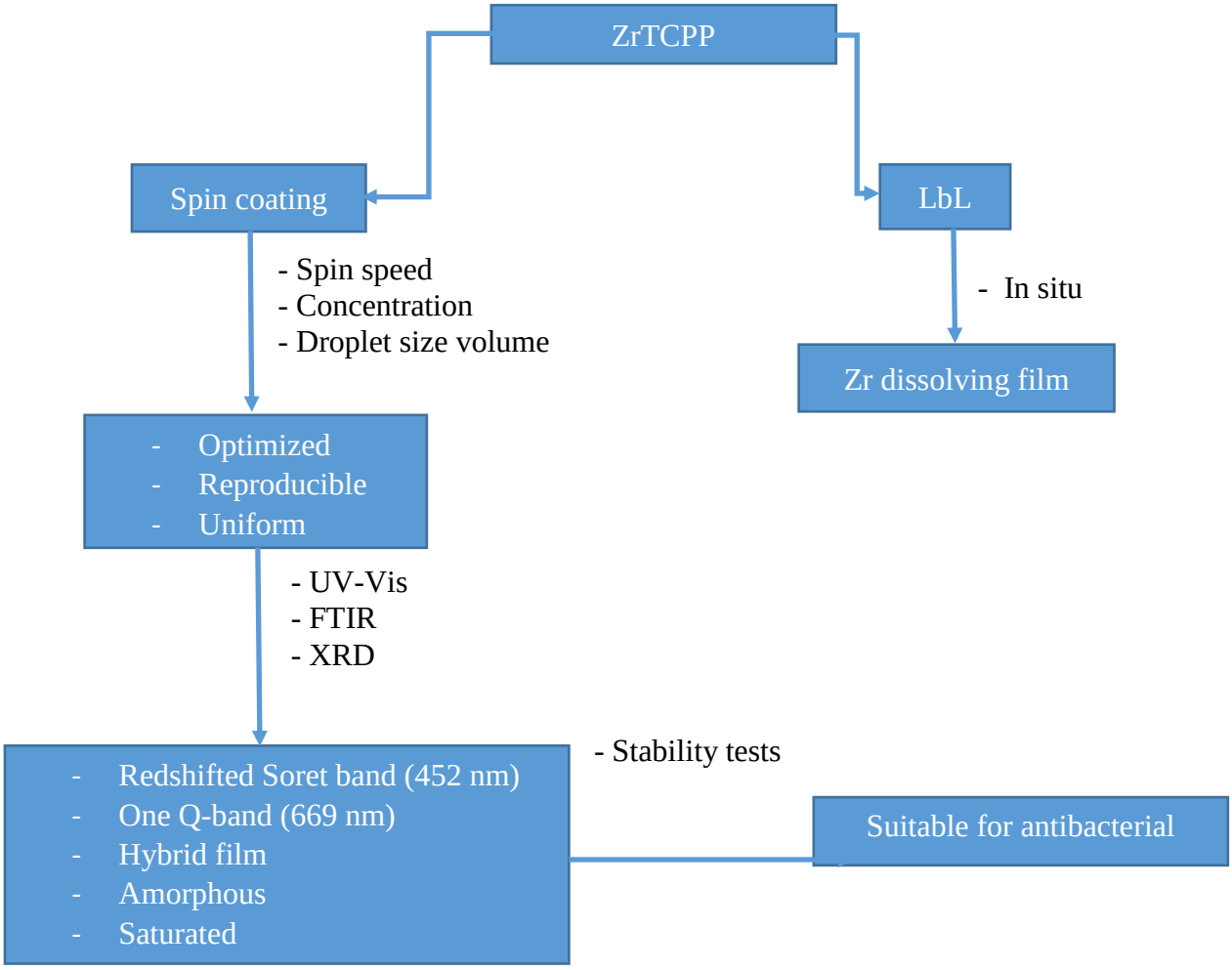


Figure 5.35: A summary of the main results from the experiment.

## 5.2 Antibacterial properties

In this section, the results from antibacterial assays will be presented. We have chosen an approach that is similar to the one used by Olsen [97] for better comparison. First, we will present the data from the experiment with planktonic cultures of *E. faecalis*, which includes both surface (attached bacteria) and supernatant (free-floating bacteria) experiments. Lastly, we will present the data for 24 hours biofilm assay.

### 5.2.1 Phototoxicity of ZrTCPP films against planktonic bacteria

The planktonic cultures of *E. faecalis* were incubated for 90 min on the surface of ZrTCPP films. Furthermore, the experiment was followed by irradiation for 5, 10, and 20 minutes with blue light that corresponds to a light dose of 22.8, 11.4, and 5.7 $Jcm^{-2}$, respectively. Figure 5.36 shows viable bacteria on the surface of ZrTCPP films after 5, 10, and 20 minutes of irradiation. We observed that the bacterial reduction increased with the increasing light dose and, surprisingly, achieved a 100% bacterial reduction after 10 minutes of irradiation. Even the samples that were not exposed to light irradiation also exhibited a significant bacterial reduction.

i)

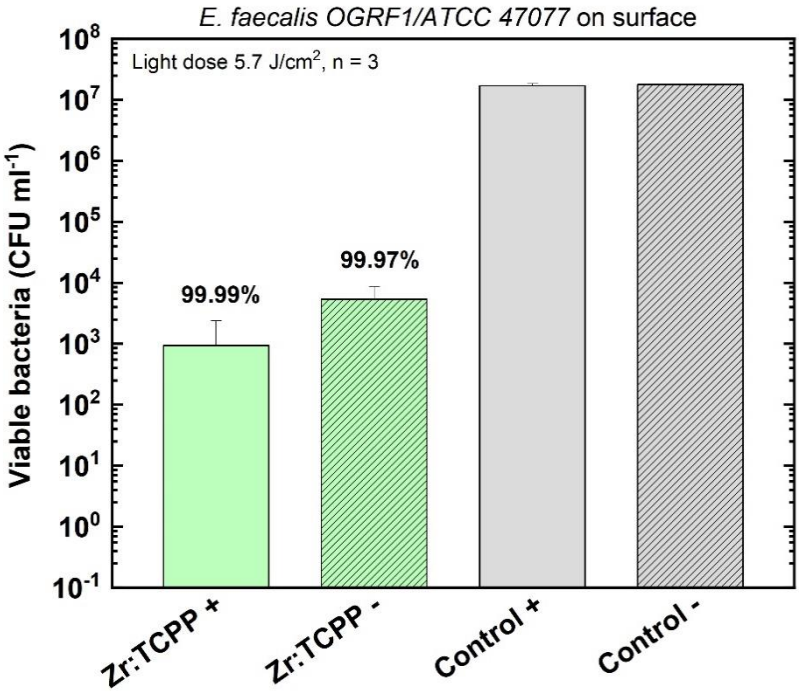

ii)

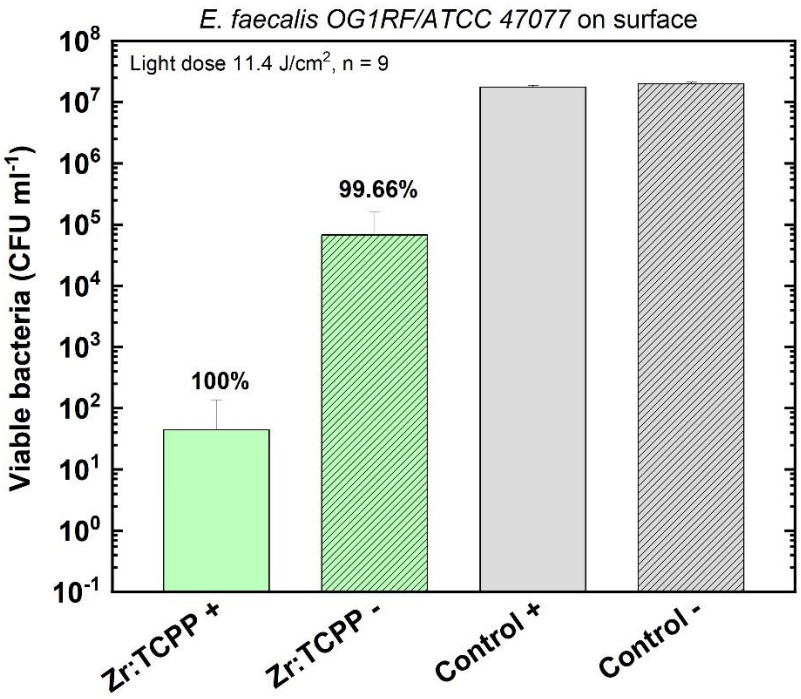


iii)

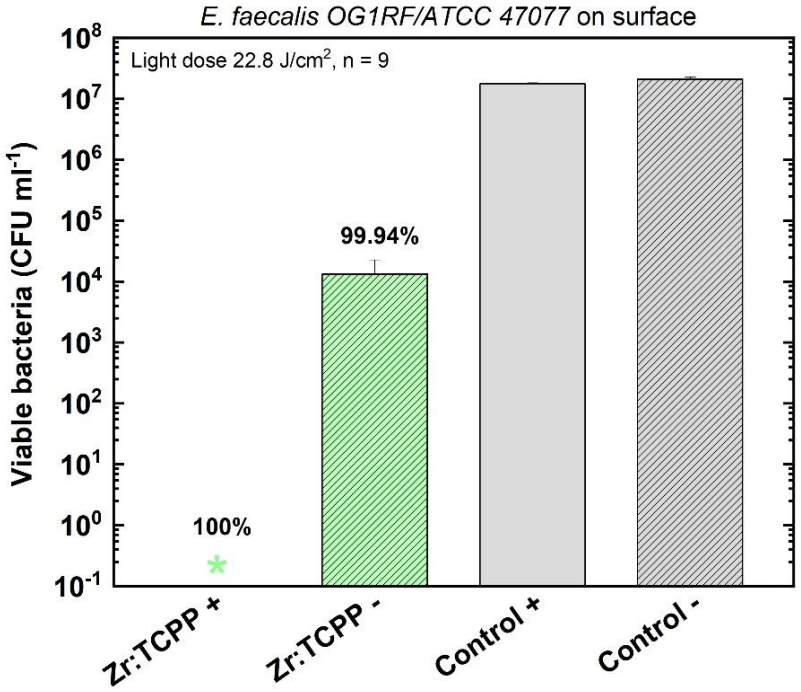


Figure 5.36: Phototoxic effect against *E. faecalis* after exposure to ZrTCPP films on the surface in combination with and in the absence of blue light irradiation. (+) indicates irradiated sample. (-) indicates non-irradiate sample. (n) is the number of samples used in this experiment. i) Light dose 5.7 $Jcm^{-2}$. ii) Light dose 11.4 $Jcm^{-2}$. iii) Light dose 22.8 $Jcm^{-2}$.

### 5.2.2 Phototoxicity in supernatant

The samples were evaluated in the supernatant of *E. faecalis* to investigate any leaching of the material into the solution. As seen in Figure 5.37, the films exhibit a significant bacterial reduction in the supernatant (free-floating bacteria). Furthermore, the bacterial reduction increases with the increasing light dose.

i)

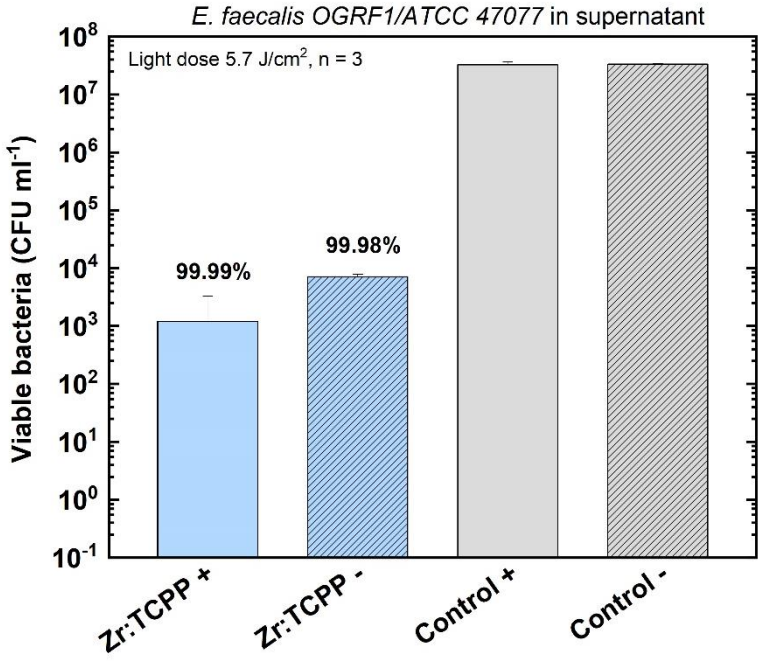

ii)

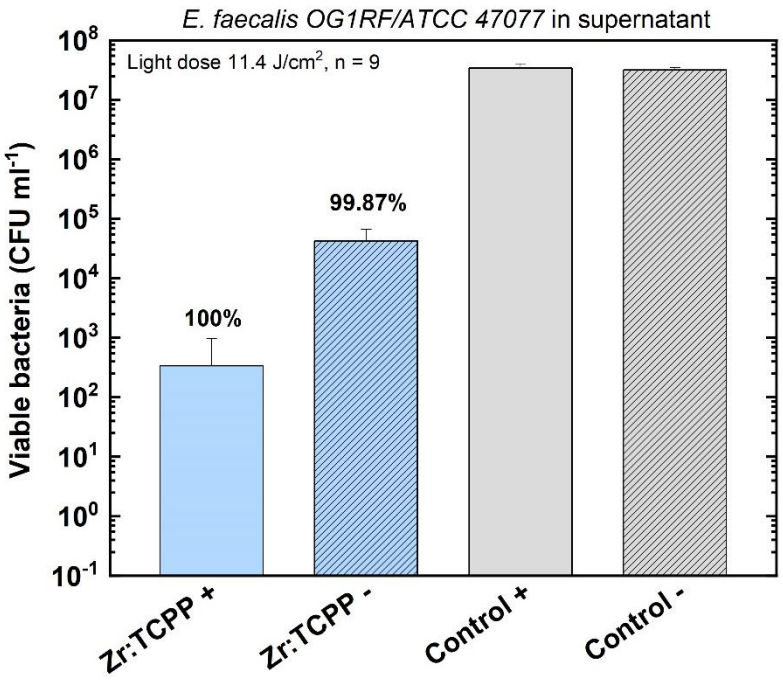


iii)

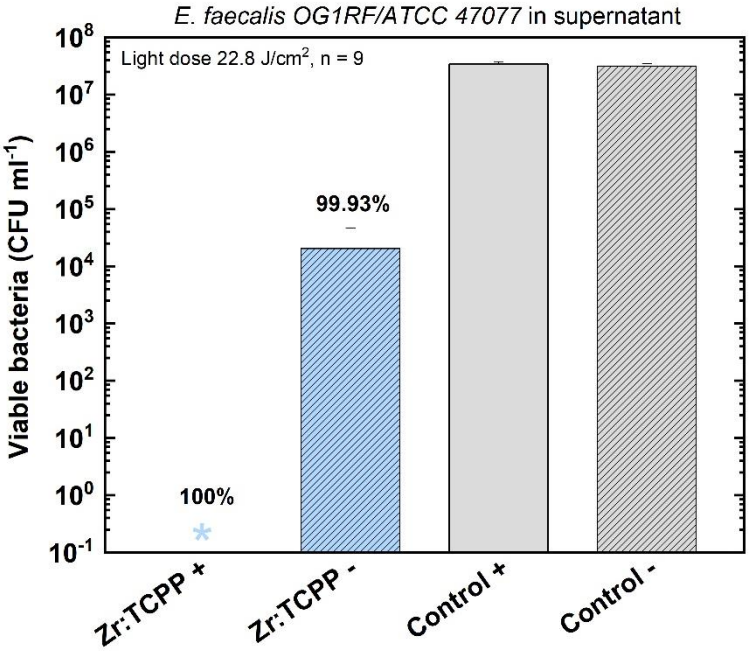


Figure 5.37: Phototoxic effect against *E. faecalis* in the supernatant after exposure to ZrTCPP films with and in the absence of blue light irradiation. (+) indicates irradiated sample. (-) indicates non-irradiate sample. (n) is the number of samples used in this experiment. i) Light dose 5.7 $Jcm^{-2}$. ii) Light dose 11.4 $Jcm^{-2}$. iii) Light dose 22.8 $Jcm^{-2}$.

### 5.2.3 Antibacterial effect against established biofilm

The antibacterial effect of ZrTCPP films against a biofilm of *E. faecalis* that had been developed for 24 hours was also evaluated. Figure 5.38 shows that the bacterial reduction in biofilm is 99.99% after 20 min of blue light irradiation. Moreover, samples without light irradiation also exhibited a significant bacterial reduction.

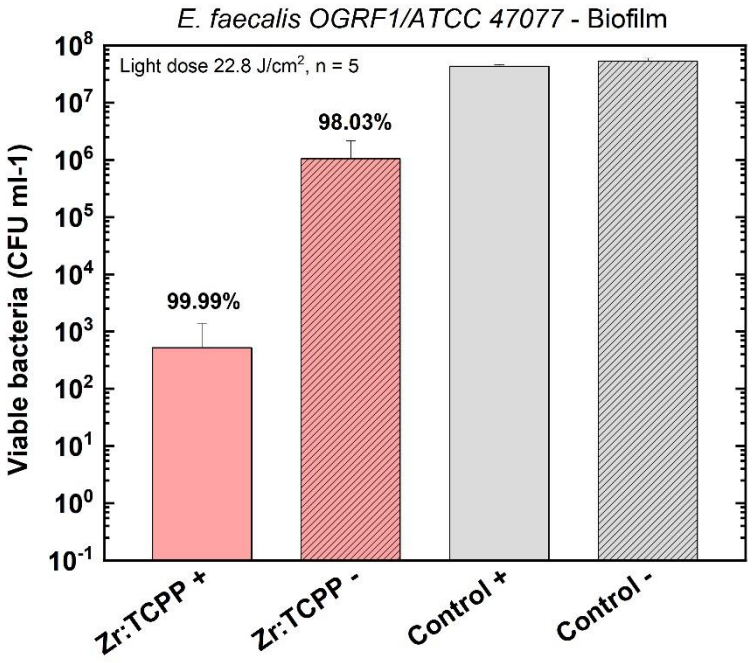


Figure 5.38: Phototoxic effect against 24-hours biofilm of *E. faecalis* after exposure to ZrTCPP films in combination with and in the absence of blue light irradiation. (+) indicates irradiated sample, (-) indicates non-irradiate sample. (n) is the number of samples used in this experiment.

The effect of the ZrTCPP surface with and without blue light irradiation on 24 h biofilm was also studied using confocal laser scanning microscopy (Figure 5.39). Bacteria cells with a damaged membrane that are considered to be dead are stained red, whereas cells with an intact membrane are stained green. Figure 5.39 shows that the bacteria in the biofilm are green before irradiation, which indicates viable bacteria. After irradiation, the micrograph shows red fluorescence, which indicates dead bacteria.

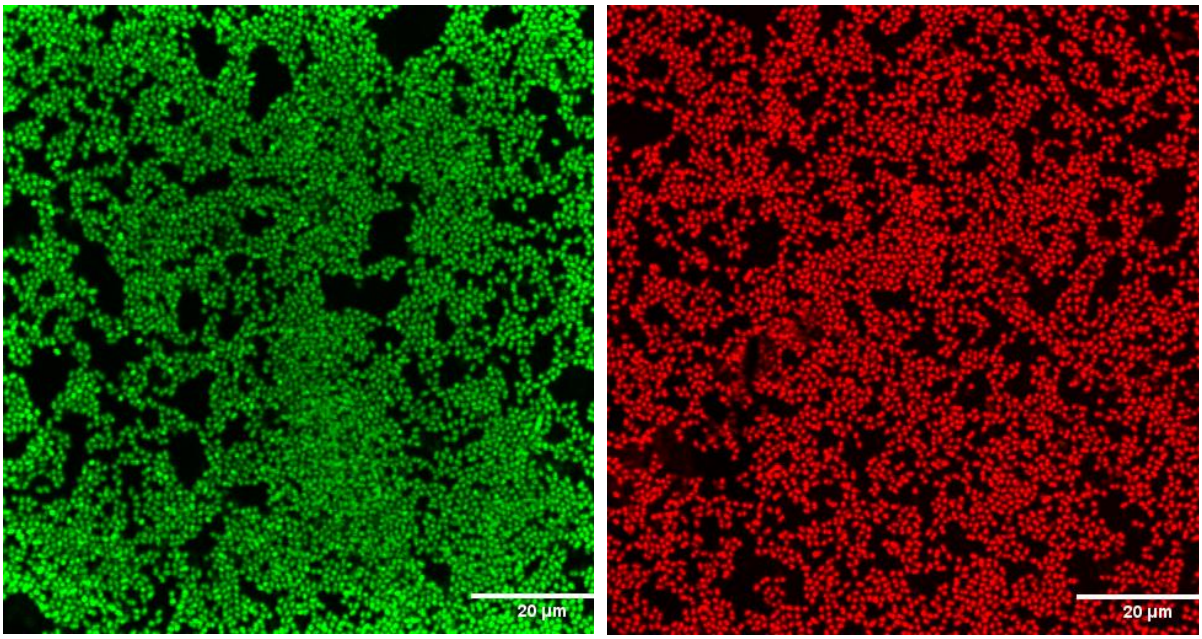


Figure 5.39: Confocal laser scanning microscopy images of *E. faecalis* biofilm stained with the LIVE/DEAD BacLight bacteria viability kit (SYTO 9 and PI) using 60x objective. Green color indicates live bacteria, and red dead bacteria. Micrographs show the biofilm before (left) and after (right) 20 min blue light irradiation.

### 5.2.4 Summary of results

5 layers of ZrTCPP thin film were evaluated for antibacterial properties. Three different environments were evaluated, on the surface, supernatant, and biofilm. The films show bactericidal effects in all experiments (Figure 5.40).

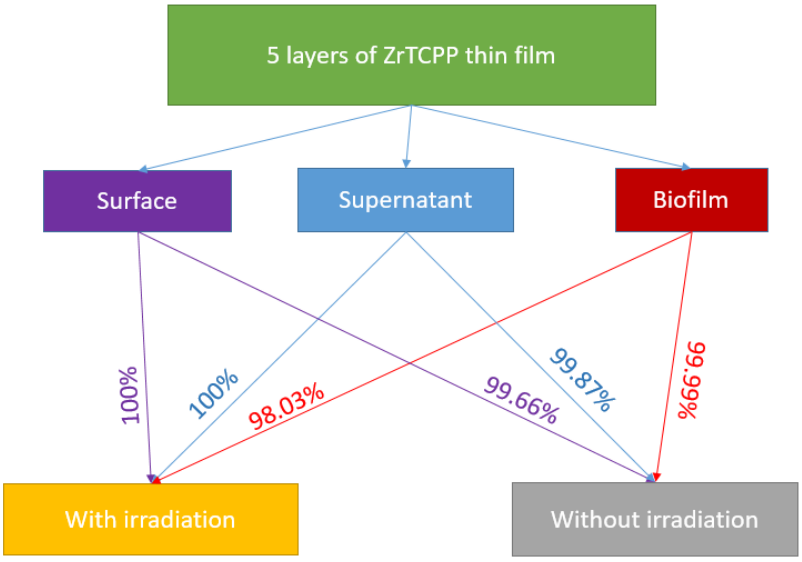


Figure 5.40: A summary of the bacterial assay.

# 6 Discussion

In this chapter, the experimental results obtained in this work will be discussed more in-depth. The discussion is divided into two parts: ZrTCPP thin film and bacterial assay.

## 6.1 ZrTCPP thin film

The synthesis of porphyrin-based materials is reported in the literature to be commonly performed under solvothermal conditions and usually takes several hours as described in the prior art. In this work, we have taken a different route for synthesizing porphyrin-based materials, by following Olsen's work on spin coating. This method differs from those reported in the literature in that it uses room temperature and short reaction times.

One of the most striking results in this work was that we achieved a homogenous thin film of ZrTCPP. From these experiments, we have seen that by alternating the deposition droplet volume, rotational speed, the concentration of precursors, rotation time, pH, and substrate treatment, all factors affected the growth of the film. This was as expected, and already proposed by Olsen. Of these parameters, the rotational speed and concentration of the precursors were the main two factors to provide homogenous thin films. Figure 5.4 shows that the ZrTCPP thin films fabricated by Olsen contained severe "coffee stain effects". By increasing the rotational speed to 4000 rpm, which is more than three times what Olsen used, the high rotational speed overcame the solution build-up at the edges and removed the "coffee stains" completely. The high rotational speed also decreased the thickness, which was compensated by increasing the concentration of precursors. By comparing the results from Olsen's UV-Vis absorption of 5 layers ZrTCPP to ours (Figure 6.1), we see that our film has a higher absorbance, which indicates that our film is thicker than hers. However, our contact angle for 5 layers of ZrTCPP are consistent with the evidence reported by Olsen. The hydrophobicity is suggested to be due to the nature of tetraphenyl porphyrins.

The results from the UV-Vis analysis (Figure 6.1) shows a redshift [67] and that four Q-bands has turned to only one Q-band. This proves that the Zr was incorporated into the core center of the porphyrin and increased the symmetry of the molecules, which reduced the number of Q-bands [58]. However, this is contrary to what was reported by So et al. [63], which suggested

that the mild conditions during the Lbl liquid deposition process promote the incorporation of free-base porphyrin in MOFs. The fact that our ZrTCPP exhibited only one Q-band limits some of the possibilities to interpret how strongly the metal ion was bonded to the core center by comparing two Q-bands ratios.

We observed a significant change in the ratio of the Soret band and the Q-band(s) upon reactions between HTCPP and Zr. For a free-base porphyrin, the intensity ratio of the Soret band:Q-band is 19:1 and 93:1 for the highest Q-band at 514 nm and the lowest Q-band at 647 nm, respectively. However, the Soret band:Q-band (at 669 nm) ratio of ZrTCPP is 3:1. This implies that the Q-band exhibited a stronger impact on the absorption of energy for metallated porphyrin in comparison to a free-base porphyrin. This result shows that the absorption energy of the TCPP is tunable by the incorporation of the metal ion and may increase the absorption of visible light. Our hypothesis is supported by Zhao et al. [100], which reported that changing the UV-Vis absorption of porphyrin-based material to exhibit a Q-band with higher intensity could promote a higher $^1O_2$ production. In addition, the redshift of the Q-band is highly favored in light therapy, especially, where the therapeutic window is considered for tissue penetration.

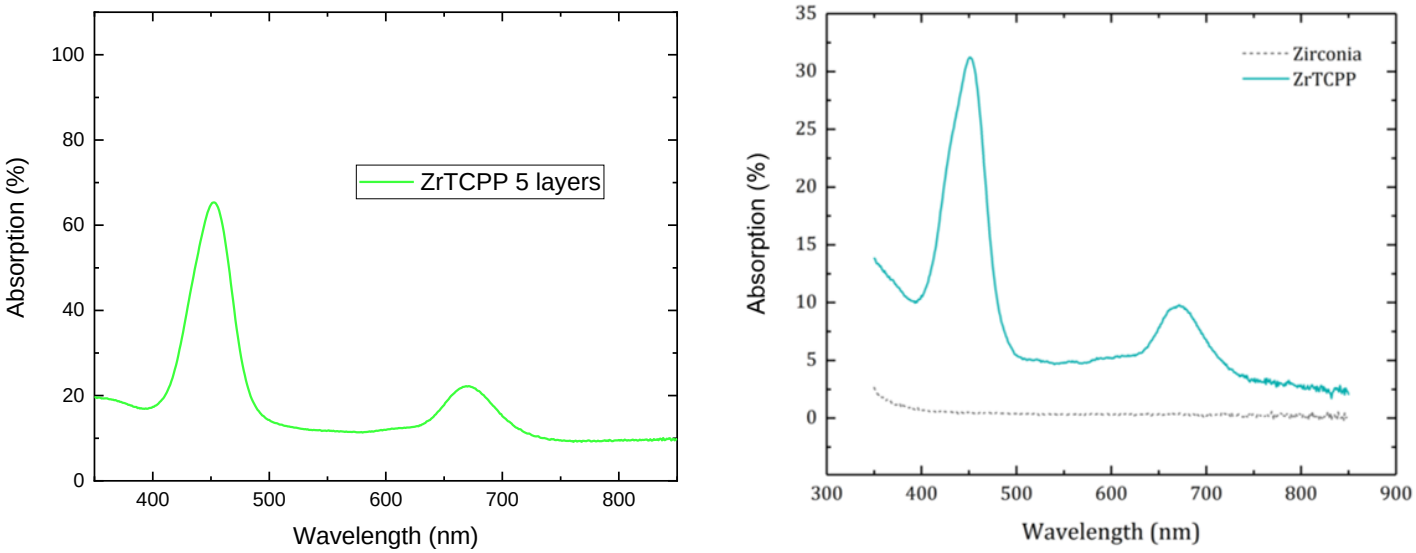


Figure 6.1. Absorption of ZrTCPP films obtained by combing transmittance and reflectance data measured by using the integrating sphere. Left: 5 layers of ZrTCPP deposited on plasma cleansed substrate. Right: 5 layers of ZrTCPP deposited on zirconia coated glass substrate from Olsen's thesis [97].

The XRD pattern shows that the ZrTCPP films are mainly amorphous, though with some features at low angles for a selection of the substrates. The information that can be obtained by XRD is therefore limited. We observe a peak at ca. 2θ = 7° (Figure 6.2.i) which corresponds to a plane distance of ca. 12.6 Å. Olsen's XRD pattern may indicate a peak around 2θ = 3° (Figure 6.2.ii), however, this may also be due to effects from a beam-stop in the diffractometer. The fact that we observe a reflection at 2θ = 7° indicates that our sample is more crystalline than Olsen's samples.

As presented in the prior art, numerous diffraction patterns have been reported for various Zr-TCPP phases in the literature (MOF-525, PCN-224, PCN-222, PCN-225, and PCN-224) although acquired for nanoparticles. The XRD pattern presented by Nie et al. [52] for PCN-224 (Figure 6.2.iv) shows peaks at 2θ = 4.62°, 6.54°, 7.90°, 9.12°, and 11.14° represented the crystal plane of [0 0 2], [0 2 2], [2 2 2], [0 0 4], and [2 2 4], respectively. A similar result is also reported by Jiang et al. [57] (Figure 6.1.iii).

i)

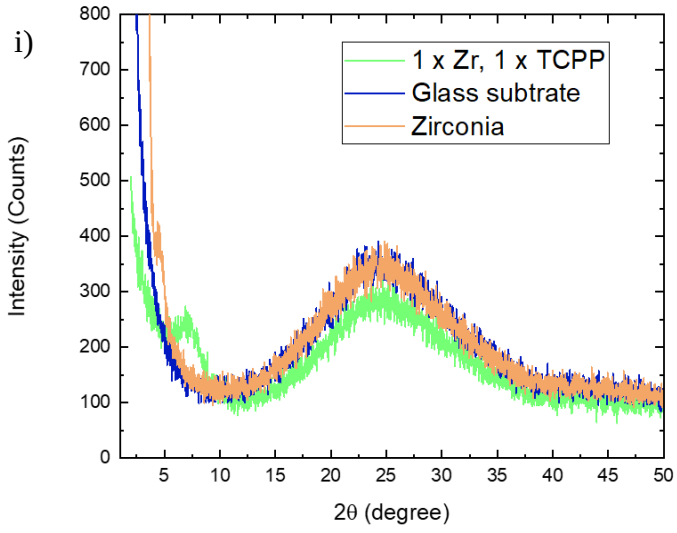


ii)

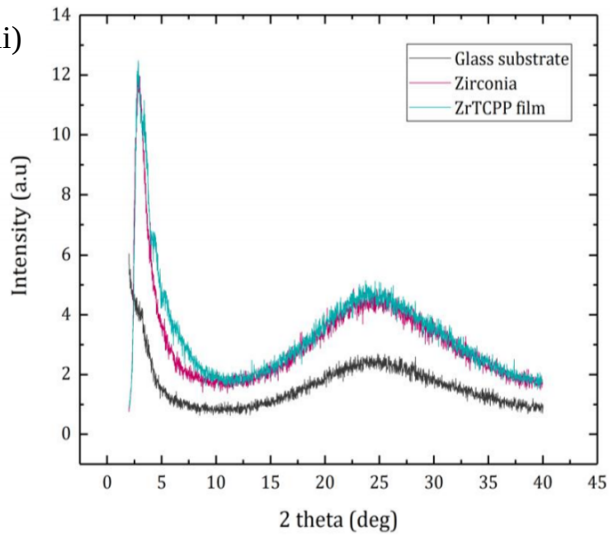

iii)

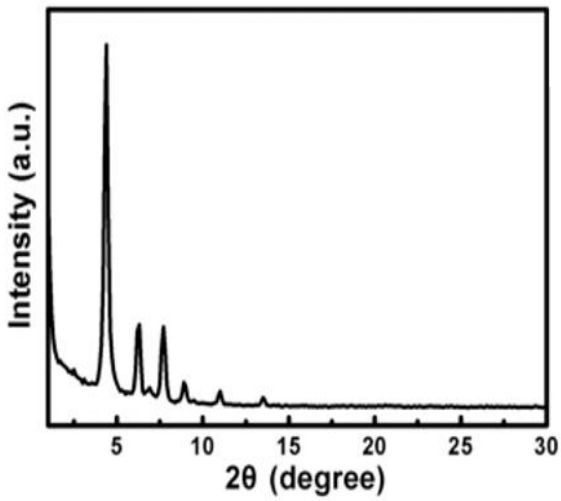


iv)

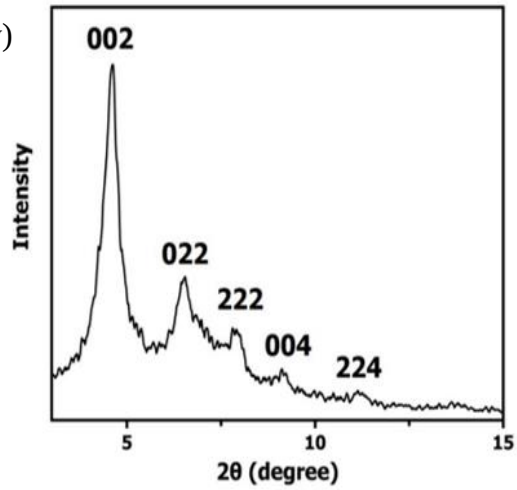


Figure 6.2: i) XRD pattern of 5 layer ZrTCPP thin film ii) XRD pattern of 5 layers ZrTCPP thin film from Olsen's thesis [97]. iii) XRD pattern of PCN-224 nanoparticles. Adapted from [57]. iv) XRD pattern of PCN-224 nanoparticles. Adapted from [52].

ZrTCPP fabricated by solvothermal is reported to exhibit a crystalline structure with distinct XRD peaks [52, 56]. Furthermore, this method also yields free-base porphyrin structures [50, 56, 60] , which means that the Zr is mainly attached to the carboxyl groups and not at the core of TCPP. This is contrary to our material that is amorphous with non-free-base porphyrin. By comparing the results, it shows that our method of synthesis favors the incorporation of Zr into the core center of TCPP, unlike solvothermal synthesis. Note that even though the strong change of UV-Vis spectra indicates that the Zr was incorporated into the center nitrogen atoms of the TCPP, it does not exclude that Zr can also be attached to the hydroxyl groups, as shown in Figure 6.3.

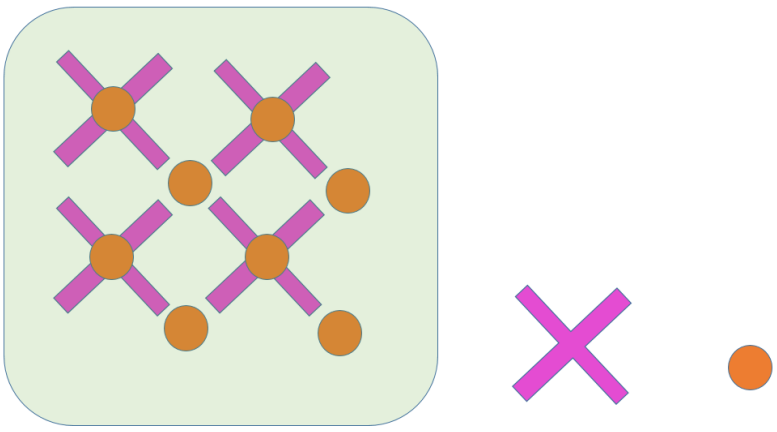

ZrTCPP TCPP Zr

Figure 6.3. A schematic illustration of the suggested ZrTCPP network. Zr is incoporated into the core center porphyrin and the hydroxyl groups.

The FTIR data shows that ZrTCPP has a feature at 681 $cm^{-1}$, which indicates Zr-O. This also strongly indicates that Zr binds to the carboxylic groups. However, it can also indicate formation of $ZrO_2$ that becomes alloyed with the film itself. In addition, the peaks related to C=O and C-O are shifted from TCPP to ZrTCPP, which indicates deprotonation of the carboxylic acid group and coordination of $Zr^{4+}$ to the carboxylate ion. In this case, the separation, Δ, between C=O and C-O provides information about the coordination mode [101]. The Δ value between peak 1543 and 1421 $cm^{-1}$ is 122, which indicates chelating (bidentate) complexes (Figure 6.4.ii). Moreover, the Δ value between peak 1634 and 1421 $cm^{-1}$ is 213, indicating unidentate complexes (Figure 6.4.i). This shows that the Zr is probably coordinated to the carboxyl groups in two different modes, which is coherent with a disordered structure.

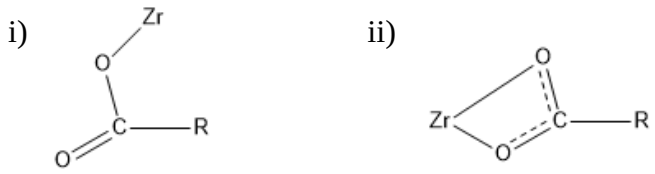


Figure 6.4: Modes of carboxylate ion complex cooridination. i) Unidentate complexes. ii) Chelating (bidendate) complexes.

### 6.1.1 Water stability

The thin film of ZrTCPP changed color from green to brown when immersed in DI water. The change was also observed in the UV-Vis spectra. Interestingly, the result indicates that the films were not as stable in water as previously expected. The ZrTCPP material has been reported to exhibit high stability in an aqueous solution [51, 58]. Jiang et al. [61] also reported that the ZrTCPP MOF exhibits high chemical stability when immersed in an aqueous solution with a pH ranging from 1 to 11. However, at low pH, the thin film exhibited similar traits as in neutral DI water, while in high pH the film was partly dissolved. One possible explanation for our discrepancy could be that our synthesis conditions produce a less crystalline material or a less stable polymorph due to the rapid synthesis conditions. Shaikh et al. [62] suggested that rapid synthesis conditions favor a less stable phase of ZrTCPP MOF. The thermodynamic stability corresponds to the formation of the polymorphs. The polymorph with the highest free energy is the most unstable, which also generally forms at the fastest rate. Usually, it takes 4-24 hours

to synthesize a porphyrin-based framework, as mentioned in the prior art. Meanwhile, our material was formed in only five minutes.

We believe that the Zr that were attached to the core center of the TCPP leached out of the film when treated with water. This can be supported by the significant change in the UV-Vis spectra. Given that it was still a film on the substrate, we speculate that it was kept together by the bonding between Zr and the carboxyl group (Figure 6.5). The EDS mapping confirmed that the film contained Zr even after leaching with water, which strengthens our hypothesis that Zr is attached to the carboxyl group. Our films when treated with DI water exhibited similar UV-Vis trends as that reported by Mu et al. [64] and Liu et al. [65]. These papers suggested that Zr was attached to the carboxyl group since the UV-Vis spectra show four Q-bands and a slight redshift of the Soret band after leaching. This result demonstrates that we can achieve a free-base porphyrin framework with metal ions with our method of fabrication without using high temperature and long reaction time as the common solvothermal/hydrothermal synthesis. The result is also consistent with the suggestion from Olsen, where she demonstrated that it was not possible to create a film with Zr (IV) and the porphyrin 5,10,15,20-tetrakis(4-hydroxy-phenyl)-21H,23H-porphine (THPP) (Figure 6.6) due to the lack of carboxyl groups. However, it was possible to create a film when she used TCPP that has carboxylate groups. In addition, when ZrTCPP films were immersed in 0.9% NaCl, a double split of the Soret band was observed. As discussed above, this indicates that some of the Zr leaked into the solution. Furthermore, the peak around 420 nm indicates Zr in carboxyl groups were stable in 24 hours, while the peak at 450 nm decreased. This is in accordance with our hypotheses that the Zr in carboxyl groups are more stable in an aqueous solution than Zr in the core center.

Moreover, section 5.1.10 demonstrated that it was possible to incorporate some of the Zr into the core center of the free-base porphyrin in the framework. This awakens the exploration of new possibilities to manipulate the structure. Others have shown that is possible to incorporate different metals into a ZrTCPP MOF [50, 57, 58]. Wang et al. [61] reported the successful incorporation of Zn into the core center of the porphyrin in the ZrTCPP framework. However, this type of exploration is out of the scope of this paper.

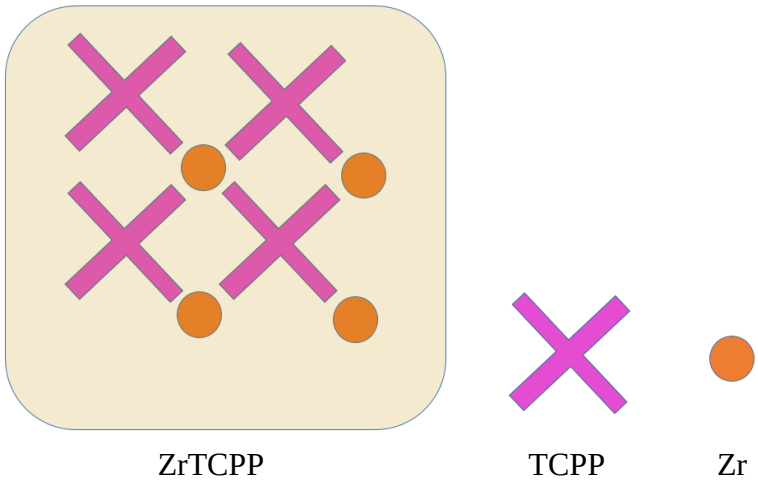


Figure 6.5. A schematic illustration of the suggested ZrTCPP network after treated in aqeous solution. Zr is atttached the hydroxyl group of the TCPP.

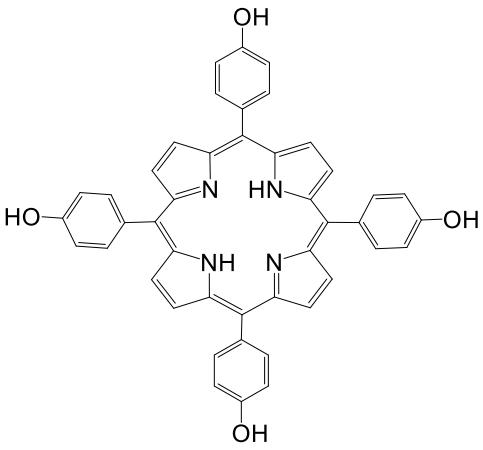


Figure 6.6: Chemical structure of THPP.

Clusters of TCPP can form J-aggregate or H-aggregate in solutions because of non-covalent interactions such as pi-pi stacking, hydrophilic-hydrophobic, and hydrogen bonding [100]. The aggregation can be influenced by metallation and the pH of the solution [102]. Therefore, we explored another possible explanation for the shift of the UV-Vis spectra based on J or H-aggregation (Figure 6.7). The J-aggregate follows a head-to-tail fashion, where the planes are stacked side-by-side. The H-aggregate follows a face-to-face fashion, where the planes are stacked perfectly on top of each other. These different patterns of stacking lead to the shifting of the UV-Vis spectra. The redshift, towards a lower wavelength, indicates J-aggregate, while a blueshift indicates an H-aggregation. In reality, is it usually a mixture of both, which can be detected by a very broad absorption [103]. The H- and J-aggregate are based on porphyrin in a solvent and cannot be directly compared to the UV-Vis of our dried thin film that was water

treated. However, in section 5.1.6, the UV-Vis absorbance measurement of Zr and TCPP dissolved in ethanol shows a redshift with the increasing Zr. The redshift could be a contribution to the J-aggregation. It has been reported that porphyrin-based material can form J- or H-aggregates in a solvent and can curl up to nanowires or rod-like structures in solid form depending on the pH of the solvent or the substituted metal-ion [100, 104, 105]. Based on this, we can not exclude that the film might in some degree exhibit self-assembly in water due to the H or J-aggregation.

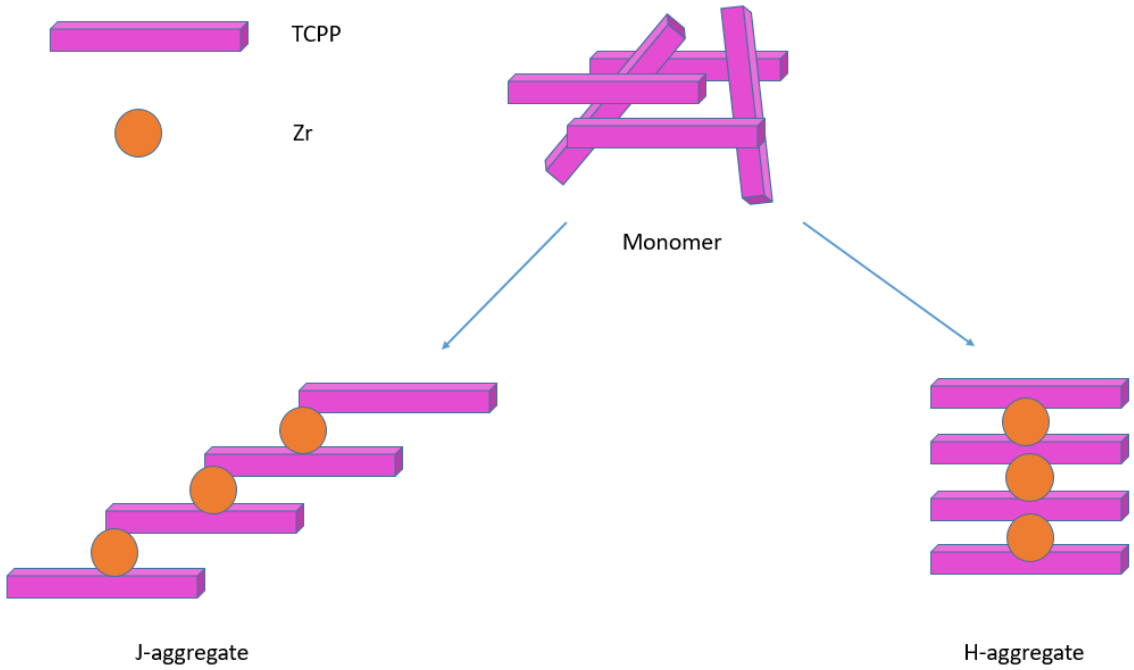


Figure 6.7: Schematic illustration of possible aggregation of porphyrin in aqueous solution.

### 6.1.2 Layer-by-layer liquid deposition

We explored the fabrication of ZrTCPP film by an LbL liquid approach in a specially designed chamber, which was based on the principle of ALD. This method was performed to explore the possibility of fabrication without bringing the precursors into the gas phase. Based on our result on the successfully fabricated thin film by spin coating and the washing step (section 5.1.7), we believed that it should be possible to recreate the principle of ALD by a liquid approach. However, this method was proven to be challenging. We did not expect that the Zr would remove the thin film, which contradicted the result in section 5.1.5, where the increased deposition of Zr per cycle yielded a thin film. Furthermore, with basis in the UV-Vis results

from section 5.1.5, we observed that the diffuse reflection of the film was increasing with the increase of Zr. We believe this to be due to the formation of $ZrO_2$. Given that the LbL liquid reaction was performed in a close chamber, this could hinder the formation of $ZrO_2$, which may be an important factor for film formation. However, this is clearly only a speculation, and further studies of the film growth have to be done. Another contradiction is observed where section 5.1.9 demonstrated that the addition of Zr in water would keep the film integrity intact, and showed that the addition of Zr would increase the green color in the water. These experiments suggested that additional Zr favors the formation of ZrTCPP material.

As seen in section 5.1.8, there are areas with missing data. Hence, an apparent limitation of this method is that the detector went into saturation and showed no signal when the chamber was fully saturated with TCPP. However, with this knowledge, the results can still be clearly interpreted. Even though we have not been able to successfully use this method to fabricate the thin film of ZrTCPP, it can still be explored further.

## 6.2 Antibacterial properties

For the discussion of the antibacterial assay we will compare the obtained results with that presented in the prior literature, with focus on antibacterials material against *E. faecalis* and porphyrin-based material against gram-positive bacteria. As explained in the prior art, different factors contribute to bacterial reduction. We have seen that there are many different protocols for antibacterial assay in the literature and must take this into account when comparing the results. To minimize the differences, we have chosen to exclude the comparison against gram-negative bacteria due to the difference in bacterial reduction in gram-positive and gram-negative as seen in the prior art. Comparing *E. faecalis* to other strains of gram-positive bacteria will give a more representative comparison.

### 6.2.1 Planktonic *E. faecalis*

We obtained a 100% bacterial reduction with a light dose of 11.4 $Jcm^{-2}$ in our experiment. Surprisingly, we observed that decreasing the light dose to 5.7 $Jcm^{-2}$ still exhibited a significant bacterial reduction (99.99%). From the prior art, we have seen that light doses vary from 10 $Jcm^{-2}$ to 360 $Jcm^{-2}$. It is clear that we have shown that our material is significantly

phototactically active. Furthermore, the result indicates that increasing the light dose would increase the bacterial reduction. This observation is in agreement with what was reported by Nie et al. [52] and Yildirim et al. [70]. However, it is important to note that a high light dose does not necessarily exhibit a high bacterial reduction, the choice of wavelengths is just as important. Pourhajibagher et al. [77] used a light dose of 360 $Jcm^{-2}$ (32 times larger than what we used in our work) and a light source with $\lambda$ = 450 nm to achieve a bacterial reduction of 1 log against *E. faecalis* with curcumin. For comparison, our light source has a $\lambda$ = 400-520 nm. Figure 6.8 shows the highest reported log reduction of antibacterial material towards the gram-positive *E. faecalis* using various antibacterial materials in each paper. In this work, we have used an inoculum size of $10^7$ $CFUml^{-1}$. In the literature in Table 1.2, it has been reported to use inoculum size ranging from $10^5$-$10^8$ $CFUml^{-1}$. A bacterial inoculum ranging from $10^5$-$10^8$ $CFUml^{-1}$ has been reported to exhibit no significant change in the bactericidal effect. However, increasing the bacterial inoculum over $10^8$ $CFUml^{-1}$ may reduce the bactericidal activity [106]. When taking this into consideration, we believe that the differences in bacterial reduction compared in this work are not significantly caused by inoculum sizes. As seen in the prior art, most of the antibacterial materials were irradiated with wavelength within visible light. Nevertheless, Huang et al. [72] and Pourhajibagher et al. [77] reported using wavelengths of 320 nm and 810 nm, respectively. Interestingly, Huang et al. [72] also reported a 100% reduction of *E. faecalis* using copper-cysteamine nanoparticles with 10 min of irradiation. As mentioned earlier, NaOCl was commonly used for treatment in the root canal. Based on these findings and comparison, a porphyrin-based material has the potential to replace NaOCl for the inactivation of *E. faecalis* in dental health.

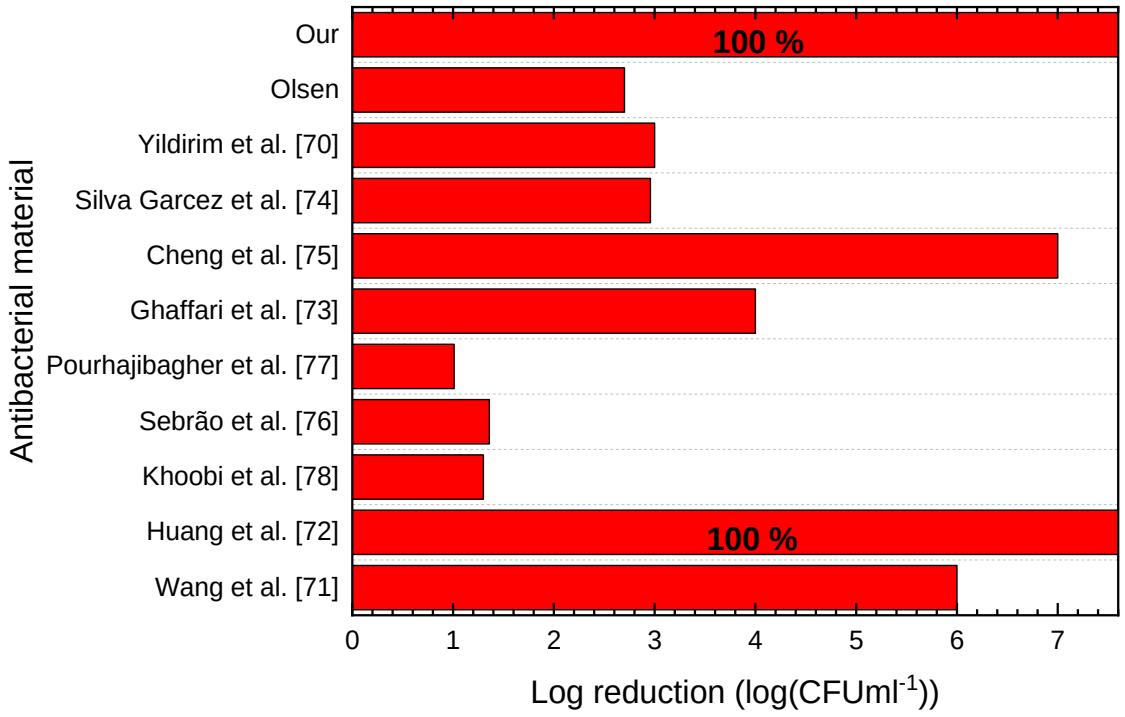


Figure 6.8: A comparison of antibacterial material bacterial log reduction of *E. faecalis*.

Our results show a higher antibacterial effect than what was reported by Olsen. We speculate that this might be due to the higher thickness of our material as mentioned earlier, which may absorb more light. In addition, our thin film was also more homogenous, which implies that it has less variations of stoichiometry. It has been reported that a higher concentration of the antibacterial material yields a higher bacterial reduction [71, 72]. Another suggestion as to why our material exhibits higher antibacterial properties is that we have a different phase of ZrTCPP than Olsen, as discussed earlier based on XRD data. We observed that we have a different phase of ZrTCPP in comparison to the ZrTCPP MOF described in the prior art. Furthermore, it has been reported that incorporating other components to solvothermal synthesized ZrTCPP MOF would increase the antibacterial property. However, PCN-WFC [52], PCN-224(Ti/Zr) [50], and ZPM@Ag(2) [56] exhibited a gram-positive bacterial reduction ranging from 1.42 to 6 log with the irradiation time of 30-60 min. These findings indicate that ZrTCPP MOF synthesized by solvothermal has a lower antibacterial property than our material.

As seen in the prior art, on average it takes 30 min of irradiation with pre-incubation ranging from 15-60 min for porphyrin-based material to exhibit a significant bacterial reduction against gram-positive or gram-negative bacteria. However, it has been reported that non-porphyrin-based materials can achieve a significant bacterial reduction down to 1-5 min of irradiation with

pre-incubation 1-5 min in the dark [70, 74, 76, 77]. Surprisingly, our result showed that porphyrin-based materials is able to compete with non-porphyrin-based material in irradiation time. However, one factor that could give us an advantage over prior reports based on porphyrin-based materials is that we used a longer incubation time (90 min). The longer incubation time could aid the bacterial to adhere more to the surface, which is favorable for bacterial reduction due to that the diffusion path of singlet oxygen in water is only 0.2 μm due to its short lifetime of 3-4 μs. Furthermore, we used a light source with wavelengths 400-520 nm, which is within visible light. Using visible light as a light source for porphyrin-based material has also been performed by reports discussed in the prior art. Figure 6.9 shows that our results are superior for bacterial reduction to what has been reported in the literature for porphyrin-based materials.

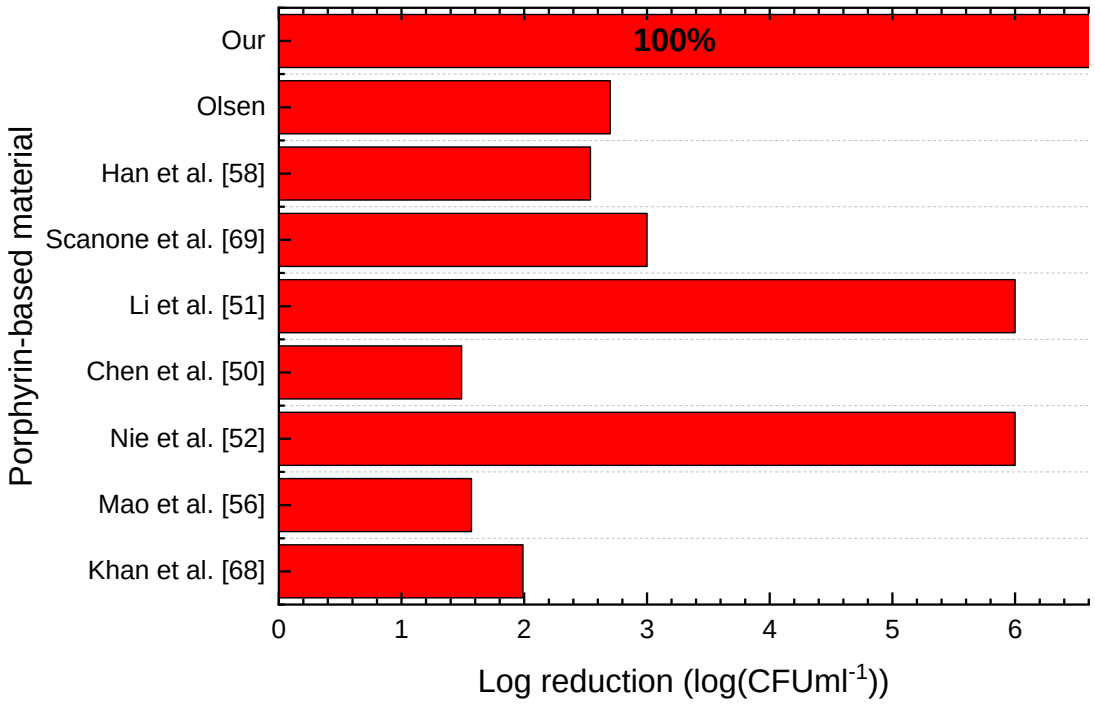


Figure 6.9: A comparison of porphyrin-based materials log reduction of gram-positive bacteria.

As discussed earlier, the films are not completely stable as expected. We expect some of the material to leach out of the films. This is confirmed by the antibacterial assay in supernatant that exhibit a 100% bacterial reduction within 10 min of light radiation. The diffusion path of singlet state oxygen in water is only 0.2 μm so some material must have leached out in order to exhibit that level of bacterial reduction.

### 6.2.2 Dark toxicity

Surprisingly, our sample exhibited a significant bacterial reduction of 3.2 log on the surface in dark mode. This result is much higher in comparison to Olsen who reported a 0.29 log reduction. Furthermore, Olsen reported a contradiction to our results, stating that the bacterial reduction in dark mode is higher in supernatant than on the surface. As seen in the prior art, porphyrin-based materials composed of TCPP shows no inactivation of bacteria in dark mode [51, 66, 69]. In addition, porphyrin-based materials composed of both Zr and TCPP, among other components, did not inherit a biologically toxic effect [50, 52, 57]. However, it has been reported that porphyrin-based materials have slight dark toxicity by Han et al. [58] and Khan et al. [68]. Our findings are contrary to results from the literature but our method of fabrication with Zr and TCPP is also different. Furthermore, our samples were fabricated under exposure to ambient lighting conditions and were in some parts further exposed to natural light during the antibacterial assay. The results also show that the bacterial reduction increased when irradiated with light. Based on this, we hypothesized that our material is extremely light-sensitive and might inherent a biologically toxic effect.

### 6.2.3 Biofilm

We observed a lower bacterial reduction in biofilm in comparison to the planktonic culture. This is in agreement with the results reported in the prior art. Unexpectedly, this result is not supported by Olsen, which achieved a higher bacterial reduction in biofilm in comparison to the planktonic. However, both Olsen's and our data indicate that ZrTCPP exhibits a great biofilm reduction in comparison to literature, as shown in Figure 6.10. Furthermore, as described in the prior art, they all used a higher light dose ranging from 31.2 to 360 $Jcm^{-2}$. In addition, they also used a lower inoculum concentration ranging from $10^5$-$10^6$ $CFUml^{-1}$, while we used an inoculum concentration of $10^7$ $CFUml^{-1}$.

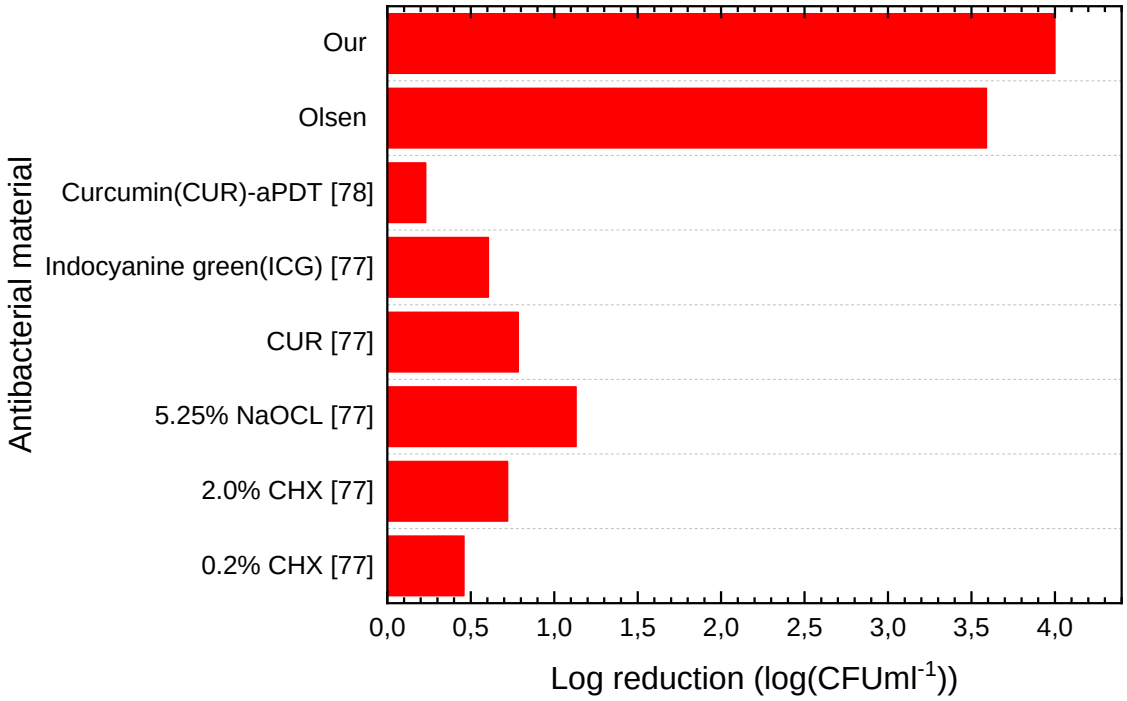


Figure 6.10: A comparison of antibacterial material bacterial log reduction of *E. faecalis* biofilm.

# 7 Conclusion

In summary, the visible-light-driven homogenous ZrTCPP thin film was synthesized successfully by a spin coating method with the optimized parameters. We have demonstrated that the key factors to remove the "coffee stain effect" and increase the uniformity were by increasing the rotational speed and the concentration of precursors. Furthermore, the mild conditions of deposition by spin coating, in comparison to other synthesis methods such as solvothermal, favored the incorporating of Zr into the core center of TCPP. The hybrid material exhibited a different UV-Vis absorption spectrum than for a free-base porphyrin, a redshift of the Soret band and only one Q-band was observed. In addition, it was proven that our method is highly reproducible. The water stability experiment revealed that the Zr that were attached to the carboxyl groups are more stable than Zr attached to the core center of the porphyrin. Considering that the thin film treated with water still exhibited a strong light absorption, the films could be evaluated in the antibacterial assay.

The antibacterial assay proved that the thin films showed optimized antimicrobial efficiency. With incubation of the films with bacteria culture for 90 min, followed by a 10 min of blue light irradiation (11.2 $Jcm^{-2}$), the films were able to exhibit a 100 % bacterial reduction of planktonic *E. faecalis* both on the surface and in the supernatant (free-floating bacteria). Moreover, the films were also able to reduce the 24 hours biofilm with 10 min of light irradiation (11.2 $Jcm^{-2}$) by 99.99%. Our results on the experiment without light irradiation show that the films exhibited significant dark toxicity, with a bacterial reduction of 99.93%. We believe that our material is extremely light-sensitive and might inherent a biologically toxic effect. Taking into the consideration above, the high effective photocatalytic bactericidal of ZrTCPP thin films could broaden the application prospect towards porphyrin-based materials.

Our data show that the fabrication via a layer-by-layer liquid deposition was proven to be challenging. The addition of Zr into the flow-cell reduced film formation instead of favoring film formation. Nevertheless, the observation of reaction in-situ by collecting UV-vis absorbance data demonstrated that the reaction mechanism between Zr and TCPP is highly repetitive.

# 8 Further perspectives

As with most scientific projects, this one has also resulted in some open ends and questions that are left for future works. Unfortunately the COVID-19 restriction invoked in the labs at UiO and NIOM restricted our ability to follow up on the suggestions below.

As presented in the prior art, the bacterial reduction also depend on the amount, or concentration, of antibacterial material. In our case, this would be as function of the available surface area and its roughness. In addition, a thicker film could provide a higher absorption cross section, which could increase the production of ROS. Hence, if time had allowed we wanted to explore the bacterial reduction on planktonic *E. faecalis* at different thicknesses of ZrTCPP films (5, 10, 15 layers). In addition, since we achieve a bacterial reduction of 99.99% for planktonic bacteria within 5 min of light irradiation, we wanted to decrease the light doses even further to 1 min (1.14 J/cm$^2$).

Our films exhibited significant dark toxicity, where we discussed earlier that one of the possibilities is that it is extremely light-sensitive. This could be confirmed by evaluating the singlet oxygen production. Furthermore, it would be interesting to test the phototoxicity of our materials against other strains of bacteria, such as gram-positive methicillin-resistant *S. aureus* or gram-negative *E. coli*. In addition, understand how much biofilm we can create on the ZrTCPP films (e.g. by increasing the incubation time) and to what extent we can reduce the established biofilm by phototoxicity.

We believe it is especially interesting to explore the phototoxicity at longer wavelengths, which are highly attractive in PDT where tissue penetration is considered. In addition, understanding the cytotoxicity of the ZrTCPP films by performing cell studies is crucial for further exploration. If the ZrTCPP thin films are not toxic to humans, the films could be considered to provide antibacterial coatings on e.g. dental implants.

As discussed, the Zr incorporated into the core center of the porphyrin ring was not as stable as expected. Hence, the stability of film could be explored by incorporating other metals into the ZrTCPP structure, such as Zn, Ag and Ti. The layer-by-layer approach proved challenging and showed a surprising behavior of dissolving the film for $Zr^{4+}$ exposures. The reasons behind this

is not clearly understood, and more thorough testing around this effect to understand the role of $Zr^{4+}$ would be interesting.

The stoichiometry of the ZrTCPP films have not been determined with sufficient accuracy. Unfortunately, the COVID-19 restrictions prevented us from exploring the films by x-ray photoelectron spectroscopy (XPS) which could provide valuable insight into the overall composition.

Our films are on the borderline between fully amorphous and some degree of crystallizing. We are uncertain as to how this affects the overall efficiency of the material and would have liked to explore this further by attempting post crystallization of the films by solvothermal approaches. This would also sched light on whether it is beneficial with an alloying with $ZrO_2$ in the film structure, or not.

# 9 References


1. Laxminarayan, R.P., A.M.D. Duse, C.M.D. Wattal, A.K.M.M.D. Zaidi, H.F.L.M.D. Wertheim, N.P. Sumpradit, E.M.D. Vlieghe, G.L.P. Hara, I.M.M. Gould, H.P. Goossens, C.P. Greko, A.D.P. So, M.M.P.H. Bigdeli, G.P. Tomson, W. Woodhouse, E.P. Ombaka, A.Q.P. Peralta, F.N.M. Qamar, F.P. Mir, S.P. Kariuki, Z.A.P. Bhutta, A.P. Coates, R.M. Bergstrom, G.D.P. Wright, E.D.P. Brown and O.P. Cars, *Antibiotic resistance—the need for global solutions.* Lancet Infect Dis, 2013. **13**(12): p. 1057-1098.
2. Mrabet, B., M.N. Nguyen, A. Majbri, S. Mahouche, M. Turmine, A. Bakhrouf and M.M. Chehimi, *Anti-fouling poly(2-hydoxyethyl methacrylate) surface coatings with specific bacteria recognition capabilities.* Surface science, 2009. **603**(16): p. 2422-2429.
3. Ivanova, E.P., V.K. Truong, H.K. Webb, V.A. Baulin, J.Y. Wang, N. Mohammodi, F. Wang, C. Fluke and R.J. Crawford, *Differential attraction and repulsion of Staphylococcus aureus and Pseudomonas aeruginosa on molecularly smooth titanium films.* Sci Rep, 2011. **1**(1): p. 165-165.
4. Milgrom, L.R., *The colours of life : an introduction to the chemistry of porphyrins and related compounds*. 1997, Oxford: Oxford University Press.
5. Piddock, L.J.V., *The crisis of no new antibiotics—what is the way forward?* The Lancet Infectious Diseases, 2012. **12**(3): p. 249-253.
6. Hutmacher, D.W. and W. Chrzanowski, *Biointerfaces : where material meets biology*. 2015, Royal Society of Chemistry: Cambridge, England.
7. O'Neill, J., *Review on antimicrobial resistance.* Antimicrobial resistance: tackling a crisis for the health and wealth of nations, 2014. **2014**(4).
8. Yong, C., *COVID-19.* Journal of the American College of Cardiology, 2020. **75**(20): p. 2639-2641.
9. Saleem, Z., B. Godman, M.A. Hassali, F.K. Hashmi, F. Azhar and I.U. Rehman, *Point prevalence surveys of health-care-associated infections: a systematic review.* Pathogens and global health, 2019. **113**(4): p. 191-205.
10. Getahun, H., I. Smith, K. Trivedi, S. Paulin and H.H. Balkhy, *Tackling antimicrobial resistance in the COVID-19 pandemic.* Bull World Health Organ, 2020. **98**(7): p. 442-442A.

11. Ruiz, J., *Enhanced antibiotic resistance as a collateral COVID-19 pandemic effect?* The Journal of hospital infection, 2021. **107**: p. 114-115.
12. Hsu, J., *How covid-19 is accelerating the threat of antimicrobial resistance.* BMJ, 2020. **369**: p. m1983.
13. Caselli, E., *Hygiene: microbial strategies to reduce pathogens and drug resistance in clinical settings.* Microb Biotechnol, 2017. **10**(5): p. 1079-1083.
14. Sobotta, L., P. Skupin-Mrugalska, J. Piskorz and J. Mielcarek, *Porphyrinoid photosensitizers mediated photodynamic inactivation against bacteria.* Eur J Med Chem, 2019. **175**: p. 72-106.
15. Dale, J., *Molecular genetics of bacteria*, S. Park, Editor. 2004, John Wiley & Sons: Chichester, West Sussex, England

Hoboken, N.J.

16. Beech, I.B. and J. Sunner, *Biocorrosion: towards understanding interactions between biofilms and metals.* Current Opinion in Biotechnology, 2004. **15**(3): p. 181-186.
17. Hasan, J., R.J. Crawford and E.P. Ivanova, *Antibacterial surfaces: the quest for a new generation of biomaterials.* Trends in Biotechnology, 2013. **31**(5): p. 295-304.
18. Zhou, F., *Antifouling Surfaces and Materials : From Land to Marine Environment*. 2015, Springer Berlin Heidelberg : Imprint: Springer: Berlin, Heidelberg.
19. Yu, Q., Y. Zhang, H. Wang, J. Brash and H. Chen, *Anti-fouling bioactive surfaces.* Acta Biomater, 2011. **7**(4): p. 1550-1557.
20. Magin, C.M., S.P. Cooper and A.B. Brennan, *Non-toxic antifouling strategies.* Materials Today, 2010. **13**(4): p. 36-44.
21. Rana, D. and T. Matsuura, *Surface Modifications for Antifouling Membranes.* Chemical Reviews, 2010. **110**(4): p. 2448-2471.
22. Chambers, L.D., K.R. Stokes, F.C. Walsh and R.J.K. Wood, *Modern approaches to marine antifouling coatings.* Surface and Coatings Technology, 2006. **201**(6): p. 3642-3652.
23. Damodaran, V.B. and N.S. Murthy, *Bio-inspired strategies for designing antifouling biomaterials.* Biomaterials Research, 2016. **20**(1): p. 18.
24. Truong, V.K., H.K. Webb, E. Fadeeva, B.N. Chichkov, A.H.F. Wu, R. Lamb, J.Y. Wang, R.J. Crawford and E.P. Ivanova, *Air-directed attachment of coccoid bacteria to the surface of superhydrophobic lotus-like titanium.* Biofouling, 2012. **28**(6): p. 539-550.

25. Michels, H., S. Wilks, J. Noyce and C. Keevil, *Copper Alloys for Human Infectious Disease Control.* Materials Science and Technology, 2005. **1**.
26. Lara, H.H., N.V. Ayala-Núñez, L.d.C. Ixtepan Turrent and C. Rodríguez Padilla, *Bactericidal effect of silver nanoparticles against multidrug-resistant bacteria.* World Journal of Microbiology and Biotechnology, 2010. **26**(4): p. 615-621.
27. Knetsch, M.L.W. and L.H. Koole, *New Strategies in the Development of Antimicrobial Coatings: The Example of Increasing Usage of Silver and Silver Nanoparticles.* Polymers, 2011. **3**(1): p. 340-366.
28. Meng, J., P. Zhang and S. Wang, *Recent Progress in Biointerfaces with Controlled Bacterial Adhesion by Using Chemical and Physical Methods.* Chemistry – An Asian Journal, 2014. **9**(8): p. 2004-2016.
29. Ivanova, E.P., J. Hasan, H.K. Webb, V.K. Truong, G.S. Watson, J.A. Watson, V.A. Baulin, S. Pogodin, J.Y. Wang, M.J. Tobin, C. Löbbe and R.J. Crawford, *Natural Bactericidal Surfaces: Mechanical Rupture of Pseudomonas aeruginosa Cells by Cicada Wings.* Small, 2012. **8**(16): p. 2489-2494.
30. Robertson, C.A., D.H. Evans and H. Abrahamse, *Photodynamic therapy (PDT): A short review on cellular mechanisms and cancer research applications for PDT.* Journal of Photochemistry and Photobiology B: Biology, 2009. **96**(1): p. 1-8.
31. Calin, M.A. and S.V. Parasca, *Light sources for photodynamic inactivation of bacteria.* Lasers in Medical Science, 2009. **24**(3): p. 453-460.
32. Maisch, T., J. Baier, B. Franz, M. Maier, M. Landthaler, R.-M. Szeimies and W. Bäumler, *The role of singlet oxygen and oxygen concentration in photodynamic inactivation of bacteria.* Proceedings of the National Academy of Sciences, 2007. **104**(17): p. 7223.
33. Maisch, T., *Resistance in antimicrobial photodynamic inactivation of bacteria.* Photochem Photobiol Sci, 2015. **14**(8): p. 1518-1526.
34. de Melo, W.C.M.A., P. Avci, M.N. de Oliveira, A. Gupta, D. Vecchio, M. Sadasivam, R. Chandran, Y.-Y. Huang, R. Yin, L.R. Perussi, G.P. Tegos, J.R. Perussi, T. Dai and M.R. Hamblin, *Photodynamic inactivation of biofilm: taking a lightly colored approach to stubborn infection.* Expert Rev Anti Infect Ther, 2013. **11**(7): p. 669-693.
35. Daniell, M.D. and J.S. Hill, *A HISTORY OF PHOTODYNAMIC THERAPY.* Aust N Z J Surg, 1991. **61**(5): p. 340-348.
36. Ito, Y., *Photochemistry for Biomedical Applications : From Device Fabrication to Diagnosis and Therapy*. 2018, Springer Singapore : Imprint: Springer: Singapore.

37. Atkins, P.W., *Atkins' physical chemistry*. 10th ed. ed, ed. J. De Paula. 2014, Oxford: Oxford University Press.
38. Hashimoto, T., Y.-K. Choe, H. Nakano and K. Hirao, *Theoretical Study of the Q and B Bands of Free-Base, Magnesium, and Zinc Porphyrins, and Their Derivatives.* J. Phys. Chem. A, 1999. **103**(12): p. 1894-1904.
39. Mack, J., *Expanded, Contracted, and Isomeric Porphyrins: Theoretical Aspects.* Chem. Rev, 2017. **117**(4): p. 3444-3478.
40. Atkins, P.W., *Atkins' physical chemistry*. Eleventh edition. ed. Physical chemistry, ed. J. De Paula and J. Keeler. 2018, Oxford: Oxford University Press.
41. Blusch, L.K., *The Siamese-Twin Porphyrin and Its Copper and Nickel Complexes: A Non-Innocent Twist*. Springer Theses. 2013: Springer.
42. Gouterman, M., *Study of the Effects of Substitution on the Absorption Spectra of Porphin.* The Journal of chemical physics, 1959. **30**(5): p. 1139-1161.
43. Gouterman, M., *Spectra of porphyrins.* Journal of Molecular Spectroscopy, 1961. **6**: p. 138-163.
44. *Porphyrins - Spectral Data of Porphyrin Isomers and Expanded Porphyrins*. 2015, Springer Berlin Heidelberg.
45. Stojiljkovic, I., B.D. Evavold and V. Kumar, *Antimicrobial properties of porphyrins.* Expert Opin Investig Drugs, 2001. **10**(2): p. 309-320.
46. Nagata, J.Y., N. Hioka, E. Kimura, V.R. Batistela, R.S.S. Terada, A.X. Graciano, M.L. Baesso and M.F. Hayacibara, *Antibacterial photodynamic therapy for dental caries: Evaluation of the photosensitizers used and light source properties.* Photodiagnosis and Photodynamic Therapy, 2012. **9**(2): p. 122-131.
47. Zhang, Q., J. He, W. Yu, Y. Li, Z. Liu, B. Zhou and Y. Liu, *A promising anticancer drug: a photosensitizer based on the porphyrin skeleton.* RSC Medicinal Chemistry, 2020. **11**(4): p. 427-437.
48. Lambrechts, S.A.G., M.C.G. Aalders and J. Van Marle, *Mechanistic Study of the Photodynamic Inactivation of <em>Candida albicans</em> by a Cationic Porphyrin.* Antimicrobial Agents and Chemotherapy, 2005. **49**(5): p. 2026.
49. Ash, C., M. Dubec, K. Donne and T. Bashford, *Effect of wavelength and beam width on penetration in light-tissue interaction using computational methods.* Lasers in medical science, 2017. **32**(8): p. 1909-1918.
50. Chen, M., Z. Long, R. Dong, L. Wang, J. Zhang, S. Li, X. Zhao, X. Hou, H. Shao and X. Jiang, *Titanium Incorporation into Zr-Porphyrinic Metal–Organic Frameworks*

*with Enhanced Antibacterial Activity against Multidrug-Resistant Pathogens.* Small, 2020. **16**(7): p. e1906240-n/a.

51. Li, J., W. Sun, Z. Yang, G. Gao, H.-H. Ran, K.-F. Xu, Q.-Y. Duan, X. Liu and F.-G. Wu, *Rational Design of Self-Assembled Cationic Porphyrin-Based Nanoparticles for Efficient Photodynamic Inactivation of Bacteria.* ACS Appl. Mater. Interfaces, 2020. **12**(49): p. 54378-54386.
52. Nie, X., S. Wu, A. Mensah, Q. Wang, F. Huang, D. Li and Q. Wei, *Insight into light-driven antibacterial cotton fabrics decorated by in situ growth strategy.* Journal of colloid and interface science, 2020. **579**: p. 233-242.
53. Lyutakov, O., O. Hejna, A. Solovyev, Y. Kalachyova and V. Svorcik, *Polymethylmethacrylate doped with porphyrin and silver nanoparticles as light-activated antimicrobial material.* RSC advances, 2014. **4**(92): p. 50624-50630.
54. Cui, H., Y. Wang, Y. Wang, Y.-Z. Fan, L. Zhang and C.-Y. Su, *A stable and porous iridium(iii)-porphyrin metal–organic framework: synthesis, structure and catalysis.* CrystEngComm, 2016. **18**(12): p. 2203-2209.
55. Liu, J., K. Zhang, Z. Chen, Z.-W. Wei and L. Zhang, *A Porous and Stable Porphyrin Metal-Organic Framework as an Efficient Catalyst towards Visible-Light-Mediated Aerobic Cross-Dehydrogenative-Coupling Reactions.* Chemistry – An Asian Journal, 2020. **15**(7): p. 1118-1124.
56. Mao, K., Y. Zhu, J. Rong, F. Qiu, H. Chen, J. Xu, D. Yang, T. Zhang and L. Zhong, *Rugby-ball like Ag modified zirconium porphyrin metal–organic frameworks nanohybrid for antimicrobial activity: Synergistic effect for significantly enhancing photoactivation capacity.* Colloids and Surfaces A: Physicochemical and Engineering Aspects, 2021. **611**: p. 125888.
57. Zhang, Y., P. Sun, L. Zhang, Z. Wang, F. Wang, K. Dong, Z. Liu, J. Ren and X. Qu, *Silver-Infused Porphyrinic Metal–Organic Framework: Surface-Adaptive, On-Demand Nanoplatform for Synergistic Bacteria Killing and Wound Disinfection.* Advanced functional materials, 2019. **29**(11): p. 1808594-n/a.
58. Han, D., Y. Han, J. Li, X. Liu, K.W.K. Yeung, Y. Zheng, Z. Cui, X. Yang, Y. Liang, Z. Li, S. Zhu, X. Yuan, X. Feng, C. Yang and S. Wu, *Enhanced photocatalytic activity and photothermal effects of cu-doped metal-organic frameworks for rapid treatment of bacteria-infected wounds.* Applied catalysis. B, Environmental, 2020. **261**: p. 118248.

59. Leng, X., H. Huang, W. Wang, N. Sai, L. You, X. Yin and J. Ni, *Zirconium-Porphyrin PCN-222: pH-responsive Controlled Anticancer Drug Oridonin.* Evid Based Complement Alternat Med, 2018. **2018**: p. 3249023-12.
60. Wang, S., W. Chen, C. Jiang and L. Lu, *Nanoscaled porphyrinic metal–organic framework for photodynamic/photothermal therapy of tumor.* Electrophoresis, 2019. **40**(16-17): p. 2204-2210.
61. Jiang, H.-L., D. Feng, K. Wang, Z.-Y. Gu, Z. Wei, Y.-P. Chen and H.-C. Zhou, *An Exceptionally Stable, Porphyrinic Zr Metal–Organic Framework Exhibiting pH-Dependent Fluorescence.* Journal of the American Chemical Society, 2013. **135**(37): p. 13934-13938.
62. Shaikh, S.M., P.M. Usov, J. Zhu, M. Cai, J. Alatis and A.J. Morris, *Synthesis and Defect Characterization of Phase-Pure Zr-MOFs Based on Meso-tetracarboxyphenylporphyrin.* Inorg. Chem, 2019. **58**(8): p. 5145-5153.
63. So, M.C., S. Jin, H.-J. Son, G.P. Wiederrecht, O.K. Farha and J.T. Hupp, *Layer-by-Layer Fabrication of Oriented Porous Thin Films Based on Porphyrin-Containing Metal–Organic Frameworks.* J. Am. Chem. Soc, 2013. **135**(42): p. 15698-15701.
64. Mu, J., L. He, W. Fan, W. Tang, Z. Wang, C. Jiang, D. Zhang, Y. Liu, H. Deng, J. Zou, O. Jacobson, J. Qu, P. Huang and X. Chen, *Cascade Reactions Catalyzed by Planar Metal–Organic Framework Hybrid Architecture for Combined Cancer Therapy.* Small, 2020. **16**(42): p. e2004016-n/a.
65. Liu, S., J. Bai, Y. Huo, B. Ning, Y. Peng, S. Li, D. Han, W. Kang and Z. Gao, *A zirconium-porphyrin MOF-based ratiometric fluorescent biosensor for rapid and ultrasensitive detection of chloramphenicol.* Biosensors & bioelectronics, 2020. **149**: p. 111801-111801.
66. Ribeiro, C.P.S., S.R.D. Gamelas, M.A.F. Faustino, A.T.P.C. Gomes, J.P.C. Tomé, A. Almeida and L.M.O. Lourenço, *Unsymmetrical cationic porphyrin-cyclodextrin bioconjugates for photoinactivation of Escherichia coli.* Photodiagnosis and photodynamic therapy, 2020. **31**: p. 101788-101788.
67. Sun, Z., S. Wu, Y. Peng, M. Wang, M. Jalalah, M.S. Al-Assiri, F.A. Harraz, J. Yang and G. Li, *Sensor array for rapid pathogens identification fabricated with peptide-conjugated 2D metal-organic framework nanosheets.* Chemical engineering journal (Lausanne, Switzerland : 1996), 2021. **405**: p. 126707.

68. Khan, R., M. Özkan, A. Khaligh and D. Tuncel, *Water-dispersible glycosylated poly(2,5'-thienylene)porphyrin-based nanoparticles for antibacterial photodynamic therapy.* Photochem Photobiol Sci, 2019. **18**(5): p. 1147-1155.
69. Scanone, A.C., N.S. Gsponer, M.G. Alvarez and E.N. Durantini, *Photodynamic properties and photoinactivation of microorganisms mediated by 5,10,15,20-tetrakis(4-carboxyphenyl)porphyrin covalently linked to silica-coated magnetite nanoparticles.* Journal of photochemistry and photobiology. A, Chemistry., 2017. **346**: p. 452-461.
70. Yildirim, C., E.S. Karaarslan, S. Ozsevik, Y. Zer, T. Sari and A. Usumez, *Antimicrobial efficiency of photodynamic therapy with different irradiation durations.* Eur J Dent, 2013. **7**(4): p. 469-473.
71. Wang, F., H. Wu, P. Jin, Z. Sun, F. Liu, L. Du, D. Wang and W. Xu, *Antimicrobial Activity of Phenyllactic Acid Against Enterococcus faecalis and Its Effect on Cell Membrane.* Foodborne Pathog Dis, 2018. **15**(10): p. 645-652.
72. Huang, L., L. Ma, W. Xuan, X. Zhen, H. Zheng, W. Chen and M.R. Hamblin, *Exploration of Copper-Cysteamine Nanoparticles as a New Type of Agents for Antimicrobial Photodynamic Inactivation.* Journal of biomedical nanotechnology, 2019. **15**(10): p. 2142-2148.
73. Ghaffari, S., A.S.K. Sarp, D. Lange and M. Gülsoy, *Potassium iodide potentiated photodynamic inactivation of Enterococcus faecalis using Toluidine Blue: Comparative analysis and post-treatment biofilm formation study.* Photodiagnosis and Photodynamic Therapy, 2018. **24**: p. 245-249.
74. Silva Garcez, A., S.C. Núñez, J.L. Lage-Marques, A.O.C. Jorge and M.S. Ribeiro, *Efficiency of NaOCl and laser-assisted photosensitization on the reduction of Enterococcus faecalis in vitro.* Oral Surg Oral Med Oral Pathol Oral Radiol Endod, 2006. **102**(4): p. e93-e98.
75. Cheng, M., Y. Zhang, X. Li, J. Liang, L. Hu, P. Gong, L. Zhang, R. Cai, H. Zhang, J. Ge, Y. Ji, Z. Guo, X. Feng, C. Sun, Y. Yang, L. Lei, W. Han and J. Gu, *Endolysin LysEF-P10 shows potential as an alternative treatment strategy for multidrug-resistant Enterococcus faecalis infections.* Sci Rep, 2017. **7**(1): p. 10164-10164.
76. Sebrão, C.C.N., A.G. Bezerra, P.H.C. de França, L.E. Ferreira and V.P.D. Westphalen, *Comparison of the Efficiency of Rose Bengal and Methylene Blue as Photosensitizers in Photodynamic Therapy Techniques for Enterococcus faecalis Inactivation.* Photomed Laser Surg, 2017. **35**(1): p. 18-23.

77. Pourhajibagher, M., N. Chiniforush, S. Shahabi, M. Palizvani and A. Bahador, *Antibacterial and Antibiofilm Efficacy of Antimicrobial Photodynamic Therapy Against Intracanal Enterococcus faecalis : An In Vitro Comparative Study with Traditional Endodontic Irrigation Solutions.* J Dent (Tehran), 2018. **15**(4): p. 197-204.
78. Khoobi, M., S. Farkhonde Masoule, M. Pourhajibagher and J. Safari, *Photodynamic Inactivation of Endopathogenic Microbiota Using Curcumin- mediated Antimicrobial Photodynamic Therapy.* Journal of Sciences, Islamic Republic of Iran, 2018. **29**(3): p. 205-209.
79. Ribeiro, M.S., F.P. Sellera and C.L. Nascimento, *Photodynamic Therapy in Veterinary Medicine: From Basics to Clinical Practice*. 2017, Cham: Cham: Springer International Publishing.
80. Lovell, J.F., T.W.B. Liu, J. Chen and G. Zheng, *Activatable Photosensitizers for Imaging and Therapy.* Chem. Rev, 2010. **110**(5): p. 2839-2857.
81. Nyokong, T. and V. Ahsen, *Photosensitizers in Medicine, Environment, and Security*. 2012, Springer Netherlands : Imprint: Springer: Dordrecht.
82. Abrahamse, H. and M.R. Hamblin, *New photosensitizers for photodynamic therapy.* Biochem J, 2016. **473**(4): p. 347-364.
83. Tronsmo, A., *Innføring i mikrobiologi*. 2016, Oslo: Universitetsforl.
84. Bardy, S.L., S.Y.M. Ng and K.F. Jarrell, *Prokaryotic motility structures.* Microbiology, 2003. **149**(2): p. 295-304.
85. French, S., D. Puddephatt, M. Habash and S. Glasauer, *The dynamic nature of bacterial surfaces: Implications for metal-membrane interaction.* Crit Rev Microbiol, 2013. **39**(2): p. 196-217.
86. König, H., H. Claus and A. Varma, *Prokaryotic Cell Wall Compounds : Structure and Biochemistry*. 2010, Springer Berlin Heidelberg : Imprint: Springer: Berlin, Heidelberg.
87. Sagar, S., S. Kaistha, A.J. Das and R. Kumar, *Antibiotic Resistant Bacteria*. 2020, Singapore: Singapore: Springer Singapore Pte. Limited.
88. Ivanova, E. and R. Crawford, *Antibacterial Surfaces*. 2015, Springer International Publishing : Imprint: Springer: Cham.
89. Rashid, R., A. Cazenave-Gassiot, I.H. Gao, Z.J. Nair, J.K. Kumar, L. Gao, K.A. Kline and M.R. Wenk, *Comprehensive analysis of phospholipids and glycolipids in the opportunistic pathogen Enterococcus faecalis.* PLoS One, 2017. **12**(4): p. e0175886-e0175886.

90. Kitz, R., U. Martens, E. Ziesenіß, P. Enck and M.A. Rose, *Probiotic E.faecalis — adjuvant therapy in children with recurrent rhinosinusitis.* Central European journal of medicine, 2012. **7**(3): p. 362-365.
91. Kanumuru, N.R. and R. Subbaiah, *Bacterial Efficacy of Ca(oH)2 Against E.faecalis Compared with three Dental Lasers on Root Canal Dentin- An Invitro Study.* J Clin Diagn Res, 2014. **8**(11): p. ZC135-ZC137.
92. Ghaffari, S., A.S.K. Sarp, D. Lange and M. Gülsoy, *Potassium iodide potentiated photodynamic inactivation of Enterococcus faecalis using Toluidine Blue: Comparative analysis and post-treatment biofilm formation study.* Photodiagnosis Photodyn Ther, 2018. **24**: p. 245-249.
93. Kääriäinen, T., D. Cameron, M.-L. Kääriäinen, A. Sherman, T. Kriinen and M.-L. Kriinen, *Atomic Layer Deposition: Principles, Characteristics, and Nanotechnology Applications*. 2013, Somerset: Somerset: John Wiley & Sons, Incorporated.
94. Graniel, O., J. Puigmartí-Luis and D. Muñoz-Rojas, *Liquid atomic layer deposition as an emergent technology for the fabrication of thin films.* Dalton Transactions, 2021.
95. Levison, M.E.M.D. and J.H.M.D.M. Levison, *Pharmacokinetics and Pharmacodynamics of Antibacterial Agents.* Infect Dis Clin North Am, 2009. **23**(4): p. 791-815.
96. Wiegand, C., C. Wiegand, M. Abel, M. Abel, P. Ruth, P. Ruth, P. Elsner, P. Elsner, U.-C. Hipler and U.-C. Hipler, *In vitro assessment of the antimicrobial activity of wound dressings: influence of the test method selected and impact of the pH.* J Mater Sci Mater Med, 2015. **26**(1): p. 1-13.
97. Olsen, M.S., *Porphyrin-based films for photodynamic inactivation of bacteria*. 2019.
98. Lu, J., Z. Li, W. An, L. Liu and W. Cui, *Tuning the Supramolecular Structures of Metal-Free Porphyrin via Surfactant Assisted Self-Assembly to Enhance Photocatalytic Performance.* Nanomaterials (Basel, Switzerland), 2019. **9**(9): p. 1321.
99. Morris, W., B. Volosskiy, S. Demir, F. Gándara, P.L. McGrier, H. Furukawa, D. Cascio, J.F. Stoddart and O.M. Yaghi, *Synthesis, Structure, and Metalation of Two New Highly Porous Zirconium Metal–Organic Frameworks.* Inorganic Chemistry, 2012. **51**(12): p. 6443-6445.
100. Zhao, Y., X. Cai, Y. Zhang, C. Chen, J. Wang and R. Pei, *Porphyrin-based metal-organic frameworks: protonation induced Q band absorption.* Nanoscale, 2019. **11**(25): p. 12250-12258.

101. Verpoort, F., T. Haemers, P. Roose and J.P. Maes, *Characterization of a Surface Coating Formed from Carboxylic Acid-Based Coolants.* Applied spectroscopy, 1999. **53**(12): p. 1528-1534.
102. Lu, J., Z. Li, W. An, L. Liu and W. Cui, *Tuning the Supramolecular Structures of Metal-Free Porphyrin via Surfactant Assisted Self-Assembly to Enhance Photocatalytic Performance.* Nanomaterials, 2019. **9**(9).
103. Choi, M.Y., J.A. Pollard, M.A. Webb and J.L. McHale, *Counterion-Dependent Excitonic Spectra of Tetra(p-carboxyphenyl)porphyrin Aggregates in Acidic Aqueous Solution.* Journal of the American Chemical Society, 2003. **125**(3): p. 810-820.
104. Koti, A.S.R. and N. Periasamy, *Self-Assembly of Template-Directed J-Aggregates of Porphyrin.* Chemistry of Materials, 2003. **15**(2): p. 369-371.
105. Yao, M., Y. Meng, X. Mao, X. Ning, Z. Zhang, D. Shan, J. Chen and X. Lu, *New insight into enhanced photocatalytic activity of morphology-dependent TCPP-AGG/RGO/Pt composites.* Electrochimica Acta, 2018. **282**: p. 575-581.
106. Mizunaga, S., T. Kamiyama, Y. Fukuda, M. Takahata and J. Mitsuyama, *Influence of inoculum size of Staphylococcus aureus and Pseudomonas aeruginosa on in vitro activities and in vivo efficacy of fluoroquinolones and carbapenems.* Journal of Antimicrobial Chemotherapy, 2005. **56**(1): p. 91-96.
107. Hofkens, J., J.r. Enderlein and M. Sauer, *Handbook of fluorescence spectroscopy and imaging: from single molecules to ensembles*. 2011: Wiley-VCH.
108. Leng, Y., *Materials Characterization: Introduction to Microscopic and Spectroscopic Methods*. 1. Aufl.
2nd ed. ed. 2009, Weinheim: Weinheim: Wiley.
109. Voigtländer, B., *Atomic Force Microscopy*. 2019, Springer International Publishing : Imprint: Springer: Cham.
110. Fujiwara, H. and R.W. Collins, *Spectroscopic Ellipsometry for Photovoltaics : Volume 1: Fundamental Principles and Solar Cell Characterization*. 2018, Springer International Publishing : Imprint: Springer: Cham.
111. Law, K.-Y. and H. Zhao, *Surface Wetting: Characterization, Contact Angle, and Fundamentals*. 2015, Cham: Cham: Springer International Publishing AG.

# Appendix A

**Characterization techniques**

## A.1 UV-VIS spectroscopy

UV-Vis spectroscopy is a method used for analyzing the absorbance or transmittance of a sample. The instrument measures intensity of light as a function of wavelength when passing through the sample. Materials have their characteristic spectra and can in some cases be used as aid for the identification of unknown samples. Furthermore, the amount of light absorbed is related to the amount of the sample and can be used to obtain a quantitative analysis.

The instrument use light to induce an electronic transition in a molecule or atom, like typical electronic transitions from the HOMO to LUMO. The higher the energy gap between the HOMO and LUMO, the shorter wavelength is required for adsorption. The instrument is composed of a broadband light source (typically tungsten and deuterium), a monochromator, a slit (wavelength selector), sample holders, a detector, and a display showing data output (e.g., software on a computer). The basic principle of a UV-Vis spectrometer is illustrated in Figure A.1. The light from a light source is dispersed by a monochromator, usually with a grating or a prism. The dispersed light is selected by a slit before it irradiates the sample, in that way, the effect of different wavelengths upon the sample can be measured. Furthermore, the detector measures the transmitted or reflected light and converts it into either current or oscillations to obtain an absorption or transmittance spectrum. The transmittance is described by the ratio between $I_o$ and $I$.

$$T = \frac{I_0}{I}$$

where $I_o$ is the incident light intensity, and the intensity of light after passing through a sample is denoted as $I$. The absorbance is the negative logarithm of transmittance and is described by the following equation:

$$A = -\log(T) = -\log\left(\frac{I}{I_0}\right)$$

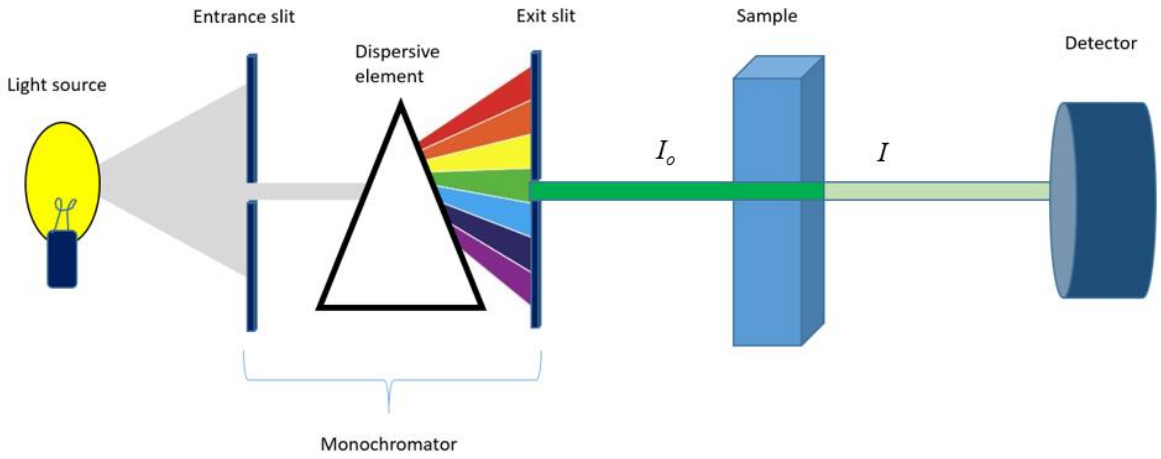


Figure A.1: A simplified illustration of the UV-Vis spectroscopy. The light is emitted from the light source and is selected by the entrance slit. Furthermore, the light is dispersed by the dispersive element and the desired wavelength is selected by the exit slit before it goes through the sample. Incident light ($I_o$) goes through a sample and some light gets absorbed. The light that is not absorbed passes through the sample denotes as $I$. Finally, the detector measures the reflected/absorbed light by the sample.

The absorbance can also be described by Lambert-Beer law. The incoming light is attenuated proportionally to the sample concentration, and the length of the light travels inside the sample.

$$A = \epsilon c l$$

where $\epsilon$ is the molar absorptivity ($M^{-1}cm^{-1}$), c is the molar concentration of the solute (mol/l or g/ml) and l is the path length (length of sample cell in cm). Because absorbance is proportional to Beer's law, the concentration can be determined. The absorbance peaks should be around 0.3 < A > 2.5 [107] (p. 7-9). Furthermore, the instrument can either have a single beam or double beam configuration. In the double beam instrument, the monochromatic light is split into two beams, one beam is used for reference and the other passes through the sample. The reference beam intensity is taken as 100% transmission (or 0% absorption). Unlike the one beam instrument, which only uses one beam for reference/sample measurement.

## A.2 X-ray diffraction (XRD)

X-rays are electromagnetic waves with wavelengths in the range of 10 picometer to 10 nanometers. X-rays are usually produced by triggering the relaxation process of an atom. This process is achieved by bombarding an anode with high-energy electrons. The energy that is released from the relaxation has different wavelengths and X-rays can be isolated from this energy [108] (p. 45-46).

The XRD is usually used for the identification of the crystal structure and composition of the sample. The crystal structure is defined by the atomic arrangement. The repeating arrangement of atoms forms distinct plans separated by well-defined distances. The interactions between X-rays and the crystal planes induce diffraction. This relationship is explained by Bragg's law:

$$n\lambda = 2\,d\sin\theta$$

where $n$ is a positive integer, $\lambda$ is the wavelength of the X-ray, $d$ is the spacing of the crystal planes, and $\theta$ is the incident angle (Figure A.2). The incoming X-rays are scattered elastic from the crystal and result in constructive or destructive interference. Constructive interference shows up as a peak in the diffraction pattern, which only happens when the waves are in phase. The difference between path lengths between waves must equal to an integer multiple of the wavelength for constructive interference [108] (p. 49-50).

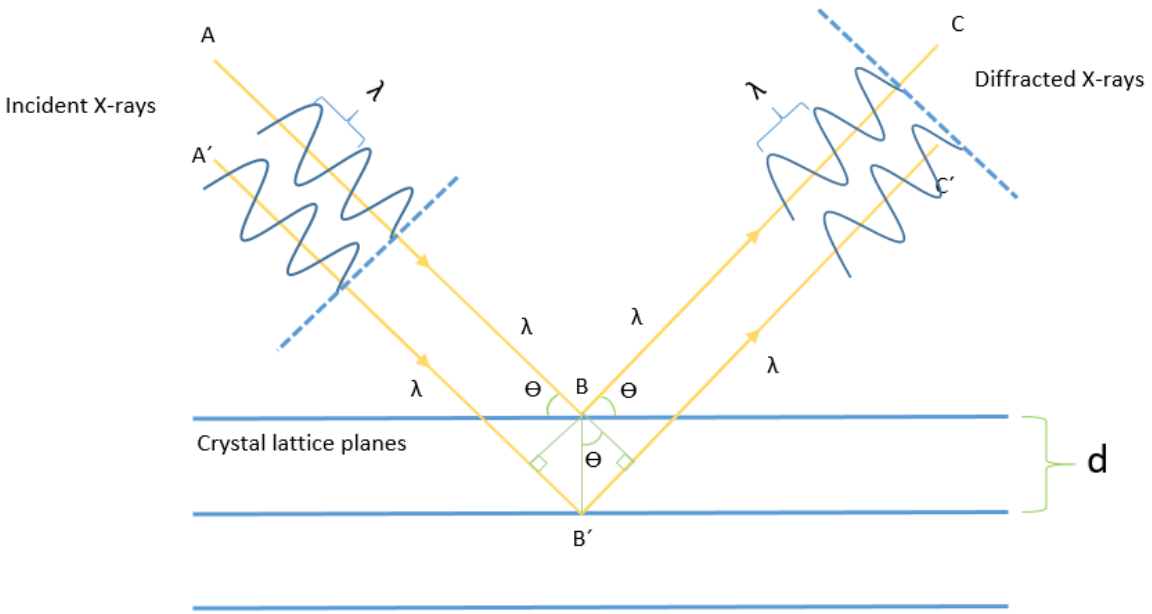

Figure A.2: Schematic illustration of Bragg diffraction in a crystal lattice. The difference between ABC and A´B´C´ is equal to 2dsin$\theta$. This distance needs to be equal to an integer number of wavelengths ($\lambda$) to produce constructive interference.

Usually, XRD uses a Bragg-Brentano geometry for measurement. The principle can be explained by the main components: an X-ray source, a sample mount, and a detector. During scanning, either the X-ray tube and the detector rotates, or the sample mounted on the sample holder rotates, but the angle between the sample and X-ray source/detector is kept constant. The sample is irradiated with X-rays, and the detector registers reflections that fulfills Brag's law from the sample [108] (p. 59-60).

## A.3 Fourier-transform infrared spectroscopy (FTIR)

Infrared spectroscopy is an instrument used to study the interaction between infrared radiation and matter. Most used for identification of an unknown components, but can also be used for quantitative information, such as additives or contaminants, kinetic information through the growth or decay of infrared absorptions. However, a centrosymmetric molecule is said to be IR inactive, and other methods such as Raman spectroscopy must be used to find the vibrational transitions.

FTIR measurements use the Fourier transformation, which is a mathematical algorithm to transform raw data into a spectrum with absorbance versus wavelength. This method allows a quick measurement by using a broad-spectrum light source instead of monochromatic beam scanning as performed for traditional IR. The advantage of this method over other IR methods is that it is faster, has a better signal-to-noise ratio, and superior wavenumber accuracy.

The FTIR instrument is built based on the Michelson interferometer system (Figure A.3). There is a source that produces infrared radiation that interacts with the Michelson interferometer. This system is set up of one beam splitter and two mirrors. The incoming broad spectrum beam is split into two beams by the beam splitter with individual travel paths. The mirrors guide these beams back into recombination that induces interference. One mirror is fixed, and the other mirror moves to create different beam path distances, consequently, obtain different intensities of interference. In this way, it is possible to acquire simultaneously spectral information of all wavelengths instead of scanning one wavelength at a time. Furthermore, the energy that is

absorbed by the sample triggers the vibration of specific molecular bonds. A combination of bond length and the atoms that are involved in this bond determines the vibration energy. There are different kinds of vibrations, but the most prominent are symmetric/asymmetric stretching, and deformation vibrations. Vibrations can be IR-active or IR-inactive, which depends on the dipole moment. If the stretching is completely symmetrical where there is no change in dipole moment, the vibrations are IR-inactive. The energy that is transmitted through the sample is measured by a detector and the obtained signal is transformed into a spectrum by a computer. The frequencies in the spectrum are given as wavenumbers on the form $cm^{-1}$. Information that is obtained from absorbed vibration gives the constituents and the bonds formed in the sample. The amount of absorption peaks indicates the number of vibrational freedom of the molecule [108] (p. 255, 257, 260-262, 267-273).

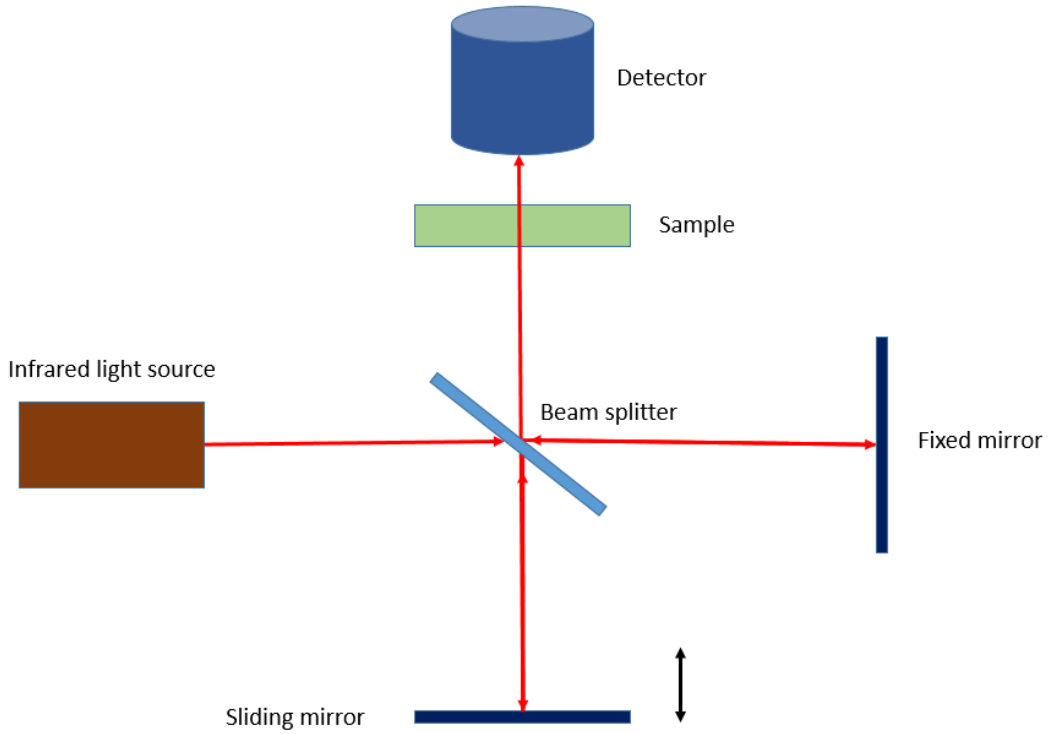


Figure A.3: Schematic illustration of the Michelson interferometer in FTIR.

## A.4 Scanning electron microscopy (SEM)

Scanning electron microscope (SEM) is an electron microscope that studies the topography of a sample by scanning its surface. As the name implies, electrons are used to study the sample as opposed to a normal light microscope that uses photons. Consequently, a much better

resolution and magnification can be obtained, due to the shorter wavelength of the accelerated electrons. Furthermore, this characterization method can provide information about morphology, chemical composition, and particle size.

A SEM consists of an electron gun, a lens system with electromagnetic lenses and aperture, different types of detectors, and an image-processing unit. The electron gun, which is the source of electrons, is located at the top of the system. There are three main types of electron guns such as thermionic emission gun, field emission gun (FEG), or a combination called a Schottky FE gun. The electron beam is created by applying a high acceleration voltage on the electron source that gives the electrons enough energy to overcome the work function. Furthermore, the electrons that escape the surface go through the lens system, which consists of condenser lenses, apertures, and the final lens. The condenser lenses and apertures are used to narrow down the electron beam, while the final lens (also known as the objective lens) is used to focus the beam to a small area on the sample. Finally, the surface of the sample can be scanned by the scan coils system that is situated above the objective lens [108] (p. 121-124).

When a high-energy electron beam hits a sample, various interactions occur and different signals are produced such as Auger electrons, secondary electrons (SE), backscattered electrons (BSE), characteristic X-rays (Figure A.4). The electron-matter interaction, which generates signals, is confined in a zone, described by a pear-shaped volume below the surface of the sample. The SEs interaction zone is usually in the depth of 5-50 nm, while the BSs usually exhibit from the depth of 50-300 nm. Signals from SE and BSE are used in SEM for imaging. As seen in Figure A.4, the production of SE is close to the surface, and therefore provides a basis for imaging with good topography contrast. While the BSE are great for imaging the contrast from the sample that arise from different atomic numbers (Z-contrast) since heavier elements disperse more electrons [108] (p. 129-130).

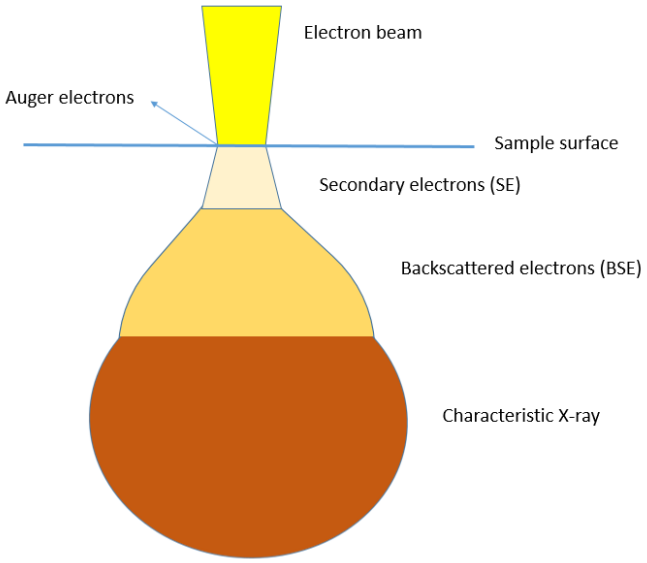


Figure A.4: Schematic illustration of electron-matter interaction. The sample is bombarded with a high-energy electron beam. As a result, different energy is released from the sample. Inspired by [108] (p. 136).

## A.5 Energy dispersive X-ray spectroscopy (EDS)

Energy dispersive X-ray spectroscopy (EDS) is a characterization technique used to analyze characteristic X-ray emitted from the electron-matter interaction by SEM. The characteristic X-rays are detected by an EDS detector, and are converted into voltage signals. The signals are processed in a computer to create a visual EDS-map by the distribution of the number of counts (pulse) of specific energy. The X-rays generated from an atom in the sample after being bombarded with high energy-electron has characteristic energy for that element, due to the unique electronic structures with unique sets of energy levels. Therefore, we can obtain information about the chemical composition of the sample. This method is a powerful tool for elemental mapping [108] (p. 183-185).

## A.6 Atomic force microscopy (AFM)

The atomic force microscope (AFM) is a method mainly used to study the surface topography of solid material at the atomic level, but also for surface manipulation. It is a versatile tool for imaging surfaces, including glass, polymers, composites, ceramics, and biological samples. The AFM instrument mainly consists of a scanning component with a cantilever with a sharp tip, a

laser beam deflection system, a feedback component, and a computer (Figure A.5). The laser beam is focused on the back of the cantilever and reflected into the detector. The tip of the cantilever is deflected by the attractive or repulsive interaction between the atoms of the sample and those of the tips while scanning through the sample. The force (F) of the tip-sample interaction that deflects the cantilever is described by Hooke's law:

$$F = -kz$$

where k is the constant factor characteristic of the spring and z is the extension. The bending of the cantilever is detected by the detector, which uses this information to generate electronic signals. These signals go to the feedback component that does a feedback loop using the laser deflection in comparison to preset references to regulate the tip-sample separation. Finally, since the feedback voltage indicates the changing of tip-sample distance, a computer is used to process these signals into a topographic image.

There are different modes for surface analyzing such as contact mode, tapping mode, and non-contact mode. The choice of measurement mode depends on the sample type. It has also a wide range of measurable force interactions, for example, van der Waals, electrical, magnetic, etc. The AFM resolution is not limited by the wavelength and aberrations because there is no illumination needed. Instead, it is determined by the finest tip diameter and the tip-sample separation [109].

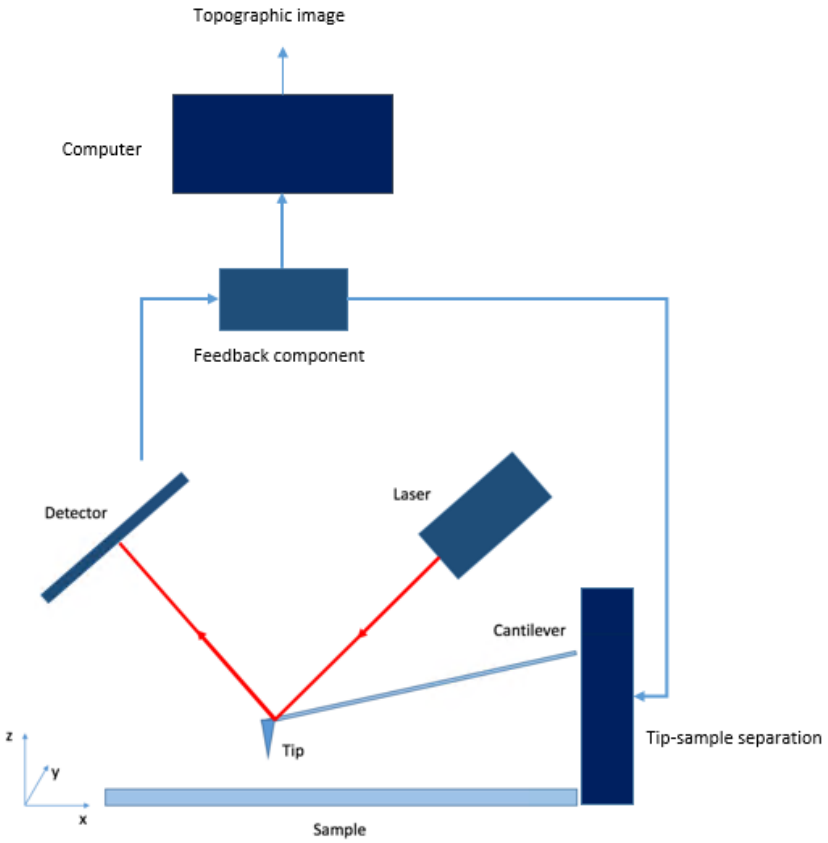


Figure A.5: A schematic illustration of components in the atomic force microscope.

## A.7 Spectroscopic ellipsometry

Spectroscopic ellipsometry is an optical measurement technique for the characterization of thin films. It obtains information such as thickness and refractive index of a material by measuring the change in polarized light upon light reflection of the sample (or light emission by a sample). Light, which is electromagnetic wave, is composed of the electric field and the magnetic field. In ellipsometry, only the electric field is considered when defining the beam polarization state. Two light waves that are arbitrarily out of phase induce elliptical polarization, hence the name "ellipsometry" (Figure A.6).

The instrument composes a light source, polarizer, analyzer, and a detector. The electromagnetic waves from the light source are polarized by a polarizer before it hits a sample at an incoming angle, and the reflected light from the sample goes through an analyzer before reaching the detector. Usually, the angle of the beam is chosen to be between 70-80º. The

ellipsometry measures two values (ψ, Δ), which is used to determine the amplitude ratio ψ and phase difference Δ between light waves known as s- and p-polarized light waves. If the electric fields of the incident and reflected light waves oscillate within the same plane, then we have a p-polarization. Whereas, the s-polarized light travels perpendicular to the incident plane. p and s-polarized light reflect differently, the ellipsometry measures the complex reflectivity ratio of p and s polarized light. The change in polarization of the incident and reflective beam is defined by the complex reflectance ratio, ρ:

$$\rho = \tan\psi \exp(i\Delta) = \frac{r_p}{r_s}$$

where $r_p$ is the change in amplitude for the p-component and $r_s$ is the change in amplitude for the s-component. The detector in ellipsometry measures Δ and ψ as a function of wavelength. These measurements have to be fitted by an optical model to obtain the optical information [110] (p. 1-5).

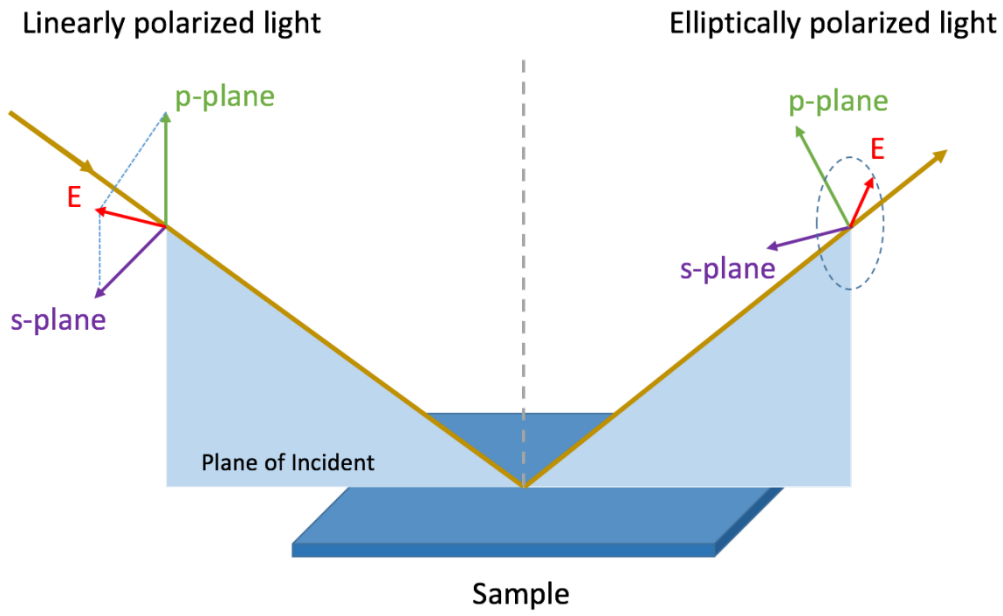


Figure A.6. Principle of ellipsometry. The incoming light that is directed on the sample is linearly polarized. The light that is reflected from the sample is elliptically polarized light.

## A.8 Contact angle

Contact angle gives an indication of how a liquid interacts with a solid surface at the three-phase boundary where a liquid, gas, and solid intersect (Figure A.7). This is a measure of the wettability of the surface, which is the ability of a liquid to maintain contact with a solid surface. The higher the surface wettability, the lower the contact angle. If the contact angle is lower than 90º, the surface is considered as hydrophilic, whereas the contact angle higher than 90º points to hydrophobic surface. It can become superhydrophobic when the contact angle is higher than 150º. The wettability can be described by the Young's equation:

$$\gamma_{LG} - \gamma_{SL} - \gamma_{SG} \cos\theta = 0$$

where $\gamma_{LG}$ is the surface tension at the liquid-vapor interface, $\gamma_{SG}$ is the surface tension at the solid-gaseous interface, $\gamma_{SL}$ the surface tension at the solid-liquid interface and $\theta$ is the contact angle [111] (p. 36-37). The contact angle between a water droplet and a surface is referred to as the water contact angle (WCA).

There are several techniques to perform contact angle measurement. One of the methods is to use a set-up that comprises a camera, a drop stage, a light source, and a computer. Water droplet of a known volume is released onto the surface at the drop stage. The camera is used to capture an image of the droplet on the surface, and the data is recorded and analyzed by the program that returns the contact angle.

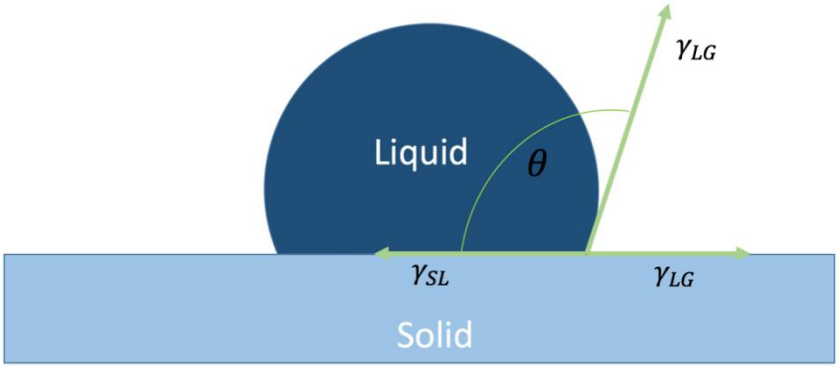


Figure A.7: Schematic illustration of a contact angle between liquid and a solid surface showing the quantities in the Young's equatio

# Appendix B

## B.1 Calculations

**Calculation of molar absorption coefficient**

Assume stoichiometry of ZrTCPP.

Concentration of ZrTCPP: $C = 2.66*10^{-5}$ M

Absorbance of 3:1 ZrTCPP at 450 nm: $A_{3:1} = 1.04895$

Molar absorbance coefficient = $C/ A_{3:1}$ = **$3.94*10^{-4}$ $M^{-1}cm^{-1}$**

**Calculation of film thickness**

Mol of ZrTCPP: $n = 2.66*10^{-8}$ mol

Molar mass of ZrTCPP: M = 790.77 g/mol

Mass of ZrTCPP: $m = n * M = 2.10^{-5}$ g

Density of ZrTCPP: $\rho = 0.676$ $gcm^{-3}$

Thickness of film if the solution is evaporated evenly over a 1 x 1 $cm^{-2}$:

$T = m / \rho = 3.11 *10^{-5}$ cm = 311.10 nm

Exclusion coefficient: $\text{Ɛ} = A_{3:1} / T = 0.003372$ $nm^{-1}$

Based on a 5 layers ZrTCPP film with typical absorption of 35 % at 450 nm, which is converted to $A_{35\%} = 0.19$.

Thickness of film = $A_{35\%} / \text{Ɛ}$ = **55.5 nm**

## B.2 EDS

i)

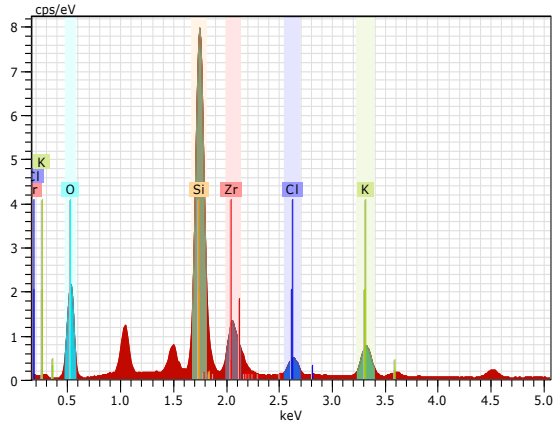


ii)

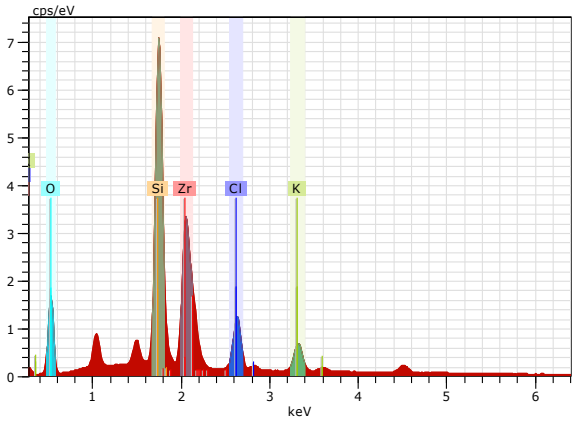


iii)

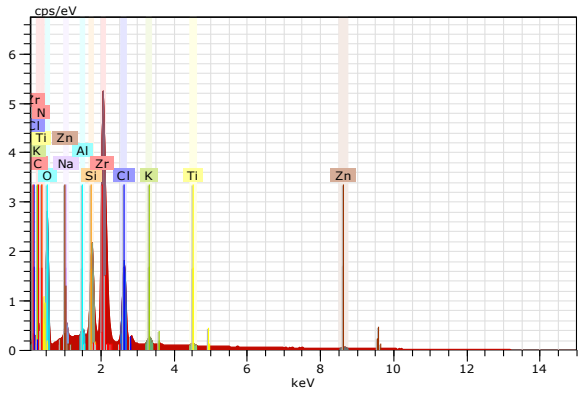


Figure B.1: EDS spectra of ZrTCPP thin films. i) 5 layers. ii) 10 layers. iii) 15 layers.

i)

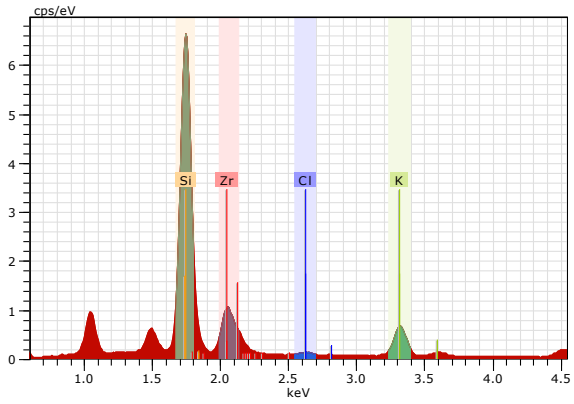


ii)

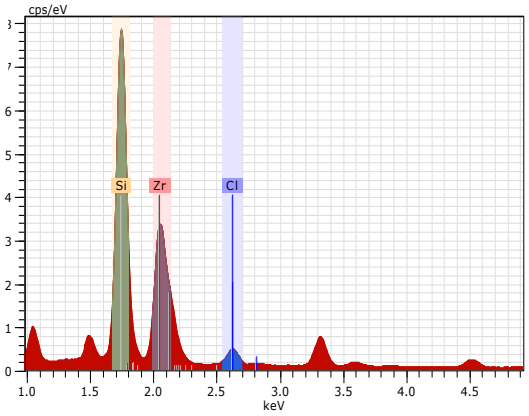

iii)

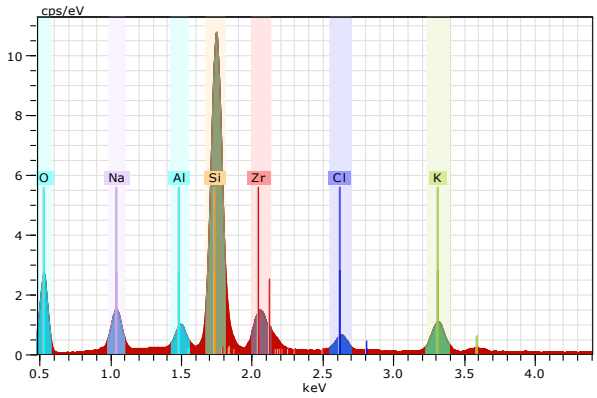


iv)

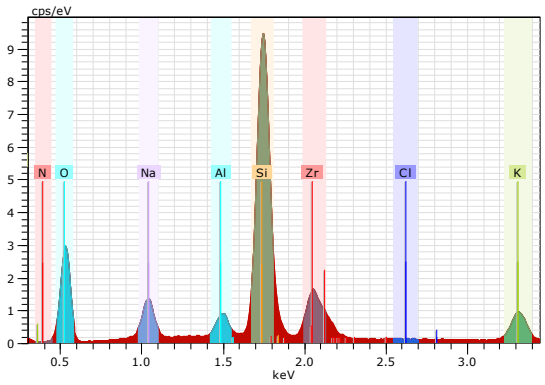


Figure B.2: EDS spectra for ZrTCPP thin film treated with aqueous solution for 3 hours. i) 5 layers of ZrTCPP in DI water. ii) 10 layers of ZrTCPP in DI water iii) 5 layers of ZrTCPP in acidic water. iv) 5 layers of ZrTCPP in basic water.